Anomalous X-ray Diffraction from Semiconductor Nanostructures
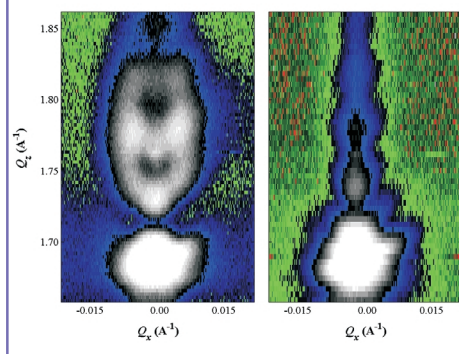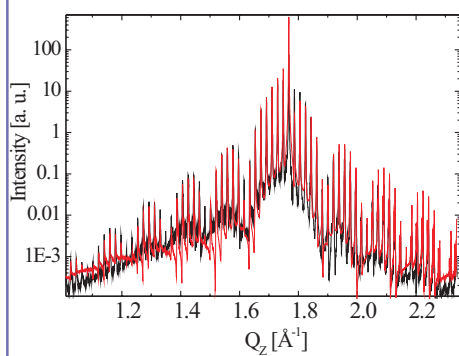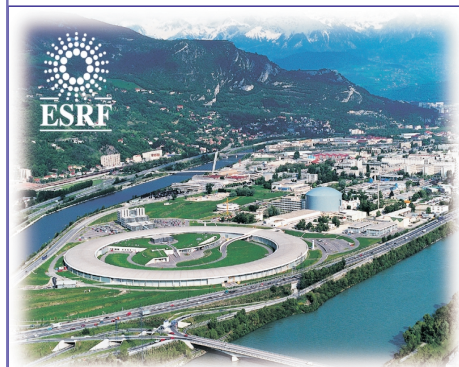
Dissertation

eingereicht von

Dipl.-Phys. Tobias Urs Schülli

Angefertigt an
der European Synchrotron Radiation Facility (ESRF) in Grenoble
in Zusammenarbeit mit dem
Institut für Halbleiterphysik der Johannes Kepler Universität Linz

Betreuung:
o.Univ.-Prof. Dr. Günther Bauer
Dr. Till Hartmut Metzger

Gutachter: o.Univ.-Prof. Dr. Günther Bauer
Prof. Dr. Václav Holý

Linz, April 2003

„La terre nous en apprend plus long sur nous que tous les livres. Parce qu'elle nous résiste. L'homme se découvre quand il se mesure avec l'obstacle. Mais, pour l'atteindre, il lui faut un outil. Il lui faut un rabot, ou une charrue. Le paysan, dans son labour, arrache peu à peu quelques secrets à la nature, et la vérité qu'il dégage est universelle.“

Antoine de Saint-Éxupéry, „Terre des hommes“, (1939).

To my parents

ii

Kurzfassung

Die vorliegende Arbeit befasst sich mit der theoretischen Behandlung anomaler Röntgendiffraktion und ihrer Anwendung zur Untersuchung von Halbleiter Heterostrukturen. Es wird gezeigt, dass anomale Techniken sowohl in der hochauflösenden Diffraktion, als auch unter streifendem Einfall eine vielversprechende Methode zur strukturellen Untersuchung kristalliner Nanostrukturen sind. Die Ergebnisse, welche für die Ausarbeitung der Messmethode und die untersuchten Proben erzielt wurden, lassen sich wie folgt zusammenfassen:

- Es wurde gezeigt, dass zur Bestimmung der atomaren Streufaktoren in der Nähe der K-Kanten die in den Kramers Kronig Relationen vereinten Annahmen der klassischen Elektrodynamik zu Werten führen, die in quantitativer Übereinstimmung mit Diffraktionsmessungen an Ge Kristallen stehen. Die theoretischen Werte für die Impulsabhängigkeit von $f_0(Q)$ von Literatur [27] wurden durch Kalibrationsmessungen an reinem Ge experimentell getestet.

- Zur Ausnutzung der starken M-Kantenresonanz von Pb, wurden Diffraktionsexperimente bei niedrigen Röntgenenergien (etwa 2500 eV) durchgeführt. Die experimentell ermittelte energieabhängige Unterdrückung von Überstrukturreflexen von Verbindungskristallen befand sich in guter Übereinstimmung mit dem theoretisch erwarteten Verhalten. Spezielle Detektoren für niedrige Röntgenenergien wurden eigens zu diesem Zweck entwickelt. Die Erweiterung des für Diffraktionsexperimente üblichen Energiebereichs hin zu niedrigeren Energien erlaubt eine Nutzung der K-Kanten vieler leichter Elemente sowie Zugewinne in der experimentellen Auflösung aufgrund der gößeren Wellenlänge.

- Die Kombination von Überstruktur Bragg-Reflexen und anomaler Effekte erlaubt eine Materialempfindlichkeit, welche zur Bestimmung von Verzerrungen in dünnen epitaktischen EuSe Schichten, hervorgerufen durch eine Gitterfehlanpassung von etwa 1 %, herangezogen wurde. Zusätzlich war hier die erhöhte Auflösung durch die langen Wellen notwendig, um die hochwertige Wachstumsqualität von EuSe/PbSeTe-Übergittern zu charakterisieren. Vollständig kohärentes pseudomorphes Wachstum wurde im Falle eines 30 Doppelschichten zählenden Übergitters mit einer Gesamtdicke von 0.3 μm nachgewiesen. Eine genaue Bestimmung des EuSe Gitterparameters in EuSe/PbSe$_{1-x}$Te$_x$ Übergittern war nur bei Röntgenenergien in der Nähe der Pb M-Kante möglich. Diese Ergebnisse

werden von grundlegender Bedeutung für die Interpretation der empfindlichen Änderung der magnetischen Eigenschaften dieser Proben sein. Letztere wurden durch magnetische Neutronenstreuung untersucht [54, 92].

- Zur Untersuchung des epitaktischen Wachstums von Ge nano-Inseln auf Si(001), wurden anomale Diffraktionsmethoden mit der Beugung unter streifendem Einfall kombiniert. Die beträchtliche Verstärkung des anomalen Effekts bei hohen Impulsüberträgen ermöglichte die modellunabhängige Bestimmung von Verzerrungs- und Konzentrationsprofil in Abhängigkeit der Höhe. Die Ausbildung der SiGe Legierung in den Inseln nach der Ge Abscheidung, führte zu keinerlei Auswaschung der wohldefinierten Grenzfläche zwischen Si-Substrat und SiGe Inseln. Bei einer Wachstumstemperatur 600°C, die niedrigste hier untersuchte, lag eine Ge Konzentration von 70-80 %, bei weitgehend gradientfreier Höhenabhängigkeit im Inneren der Inseln vor. Höhere Wachstumstemperaturen führten zu höheren Si-gehalten, ohne jedoch die scharfe Grenzfläche zu beeinträchtigen. Dies deutet darauf hin, daß die Durchmischung nicht durch Grenzflächeninterdiffusion zustande kommt, sondern durch Entfernen eines sehr stark verzerrten Gebietes im Si-Substrat welches sich entlang des Umfanges der Inseln befindet. Dies wird durch Berichte über die Ausbildung von Gräben rund um die domförmigen Inseln untermauert [14, 77, 78]. Unsere Ergebnisse stützen ebenso die neulich veröffentlichten Messungen zum mittleren Ge-Gehalt solcher Nanostrukturen [93, 94].

- In vergrabenen Quantenpunkten und 3D geordneten $PbSe/Pb_{0.92}Eu_{0.08}Te$ Übergittern konnte mittels der Aufnahme von reziproken Karten in anomaler Streuung die Orientierung und Veränderung von Facetten nach dem Überwachsen bestimmt werden. Die Ursprünglichen {010} Facetten welche von PbSe Nanopyramiden auf einer PbTe Oberfläche ausgebildet werden, bleiben wärend des Überwachsens nicht erhalten sondern werden zu {411} Facetten abgeflacht. Im Falle der Bedeckung von PbSe mit $Pb_{0.92}Eu_{0.08}Te$, liegen jedoch weiterhin wohldefinierte Facetten mit geänderter Ausrichtung vor. Der Neigungswinkel dieser Facetten entspricht der kristallographischen Richtung bevorzugter Verzerrungsausbreitung in diesen Systemen [91, 41]. Es wurde gezeigt, daß ein Überwachsen mit PbTe anstelle von $Pb_{0.92}Eu_{0.08}Te$ zu einer Auswaschung der PbSe Pyramiden führt. Die hohe Qualität der langreichweitigen 3 dimensionalen Ordnung, welche sich in $PbSe/Pb_{0.92}Eu_{0.08}Te$ Quantenpunktübergittern ausbildet, ist daher eher auf die Interdiffusionsunterdrückung durch die 8 % Eu Beimischung zu erklären, als durch die damit erreichte Gitterparametersymmetrisierung.

Abstract

In this work, we have presented a detailed theoretical treatment of anomalous x-ray diffraction methods and applied it to a study of semiconductor heterostructures. We have shown that anomalous techniques both in high resolution diffraction as well as in the grazing incidence setup offer a promising tool for the structural study of crystalline nanostructures. The results we can conclude for the technique and the studied samples can be summarized as follows:

- For the determination of the atomic scattering factors in the vicinity of K-edges, the Kramers Kronig relations derived from classical electrodynamics lead to results that were quantitatively confirmed by diffraction measurements from a Ge crystal. The theoretical values for the momentum dependence of $f_0(Q)$ taken from reference [27] have been tested experimentally by calibration measurements for pure Ge.

- Diffraction at low x-ray energies (around 2500 eV) was used to exploit the strong M-edge resonance of Pb. The attenuation of superstructure reflections from IV-VI compounds was confirmed to be in good agreement with theoretical predictions. To this end detectors were especially developed for these low energies. The extension to the lower energy regime can be used for diffraction experiments which permit the exploitation of a variety of K-edges from light elements and yields resolution gains from the use of longer wavelengths.

- The material selectivity achieved by the combination of superstructure Bragg reflections and anomalous effects was applied to measure strain in thin epitaxial EuSe layers, caused by a lattice mismatch of 1 %. Here, enhanced resolution at the long wavelength was mandatory to characterize the highly perfect growth of the EuSe/PbSeTe superlattices. Fully coherent pseudomorphic growth was found for 30 bilayers with a total thickness of 0.3 μm. The precise measurement of the EuSe lattice parameter in EuSe/PbSe$_{1-x}$Te$_x$ multilayers was only possible at x-ray energies close to the Pb M-edge. These results will be the basis for the interpretation of the sensitive change of the magnetic properties in these samples, which where investigated by magnetic neutron scattering recently [54, 92].

- To investigate the epitaxial growth of Ge nano-sized islands on Si(001), the anomalous x-ray diffraction technique was applied in grazing incidence diffraction

geometry. The anomalous effect was considerably enhanced at high momentum transfer and enabled us to determine the height profile of strain and composition in Ge rich islands independently without any model assumptions. The SiGe alloy formation during deposition of pure Ge does not dilute the well-defined interface between the Si-substrate and the SiGe island. At the lowest growth temperature of 600°C investigated here, a Ge concentration between 70 and 80 % was found throughout the island with a gradient free compositional height profile. Higher growth temperatures tend to increase the Si content and the gradient inside the SiGe islands, however, without influencing the abrupt interface. We suggest that intermixing is induced by the removal of a highly strained part of the Si-substrate surrounding the island, rather than through the island-substrate interface. This is strongly supported by the formation of trenches along the island perimeters reported in [14, 77, 78]. Our results confirm the estimations about the average Ge content published recently [93, 94].

- For buried quantum dots and 3D ordered $PbSe/Pb_{0.92}Eu_{0.08}Te$ superlattices, the orientation and transformation of facets after overgrowth could be determined via anomalous x-ray reciprocal space mapping. The original {010} facet orientation of PbSe nano-pyramids on a PbTe surface is not conserved in overgrown and multilayered samples but is changed to a {411} facet. A well-defined facet orientation is however still present after overgrowth of the PbSe with $Pb_{0.92}Eu_{0.08}Te$. The inclination angle of these facets coincides with the crystallographic direction of preferred strain propagation in these systems [91, 41]. We have shown that overgrowth with PbTe instead of $Pb_{0.92}Eu_{0.08}Te$ tends to wash out the PbSe pyramids. The highly perfect growth of 3D ordered $PbSe/Pb_{0.92}Eu_{0.08}Te$ super-lattices therefore is attributed to the prevention of interdiffusion by the 8 % Eu content rather than to the strain symmetrization achieved by this alloying.

Contents

1   Introduction

Semiconductor research and technology has been a rapidly progressing field during the last four decades. The miniaturisation in device technology permitted the enormous increase in the speed of microprocessors, and the density and read-out speed of memory devices. In 1958 the first planar integrated circuit was invented by Jack S. Kilby [1]. Seven years later, Gordon Moore, a co-founder of the Intel company, made the observation that the number of transistors per square inch in these integrated circuits had doubled every year since 1961. As he predicted that this trend would continue, the exponential growth of the transistor density became known as "Moore's Law". The doubling time turned out to be 18 months, instead of 12, but this trend has been stable for 30 years until now. Figure 1.1 shows the roadmap for the Si-based technology demonstrating the exponential behaviour in the transisitor density and the minimum feature size fabricated by the CMOS (**C**omplementary **M**etal-**O**xide **S**emiconductor) technique in recent years.
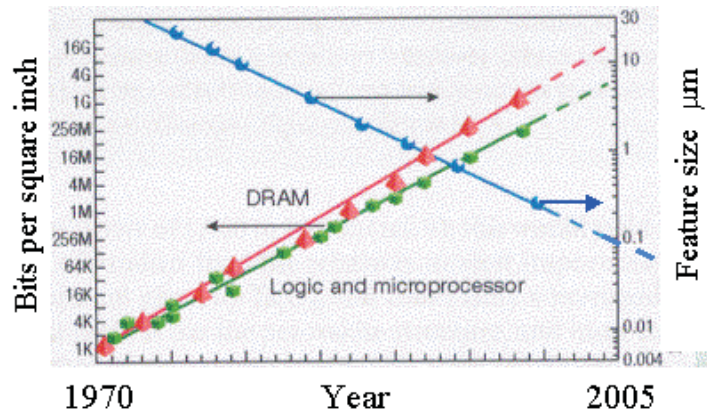
Figure 1.1: Exponential increase of the transistor density in integrated circuits, achieved by the exponential decrease of the minimum lithographic feature size. This behaviour has been stable over the last 30 years and is known as "Moore's Law".

The continuing trend might soon reach the lithographic feature size that is comparable with the de Broglie wavelength of an electron ($\approx$50 nm in Si). It is in this mesoscopic regime where quantization effects appear. No phase averaging between electrons takes place anymore, and the confinement condition starts to favour certain quantized energy levels. Besides the difficulties in accessing this region of feature size with current lithographic fabrication technologies, it can be expected that the small sizes of such nanotransistors lead to significant leakage currents due to tunnelling effects. Whilst on one hand a problem, the idea of exploiting new effects in such *quantum devices* has

fascinated researchers for decades. Propositions of logical devices based on "quantum cells" have already been made 10 years ago [2, 3]. The confinement effects of 2D electron gases in very thin films have been studied and exploited in optical devices. Here band structure engineering makes use of combinations of semiconductors, in order to achieve complex systems of heterostructures, in the dimensions of quantum confinement [4].

Semiconductor heterostructures

Molecular beam epitaxy (MBE) or metalorganic chemical vapour deposition (MOCVD) are the basic techniques in contemporary high-tech industrial fabrication of heterostructure devices. All samples investigated in this work are produced by a MBE process. The material systems are IV-VI semicondutors, mainly the lead salts, and the IV-IV system SiGe. The first one can be seen as a pioneer of all compound semiconductors, the second one promises to offer the easiest way to combine quantum dots with the existing Si based CMOS technology. A brief introduction of the systems will be given below.

IV-VI semiconductor multilayers   The IV-VI semiconductors are indeed a milestone system for developments over the last 100 years. As early as 1874 the rectifying effect of lead sulfide known as "Bleiglanz" or galena was discovered by K. F. Braun. Yet it still took 30 years before it was applied in wireless telegraphy. Braun got the Nobel price in physics together with G. Marconi in 1909. Being semiconductors with narrow bandgaps, the lead chalcogenides (PbS, PbSe, PbTe) where the first passive solid state infrared detectors in the 1950's. The main funding for development of these detectors was provided to fulfil military requirements in the seekers of short range air to air and ground to air missiles [5]. This knowledge is nowadays exploited in active devices for night vision cameras and thermal imaging in medical applications [6]. The opportunity to alloy the lead with the europium chalcogenides due to their identical crystal structure and similar lattice parameters, permits widely tunable bandgaps from the far infrared to the visible spectrum. In Fig. 1.2 several emission spectra according to Planck's law are plotted for different temperatures. The IV-VI bandgaps cover a temperature range that extends from the emission maximum at room temperatures up to the radiation emitted by light bulb filaments. The presence of atmospheric transparency over a vast part of this range opens up a wide field of possible applications.
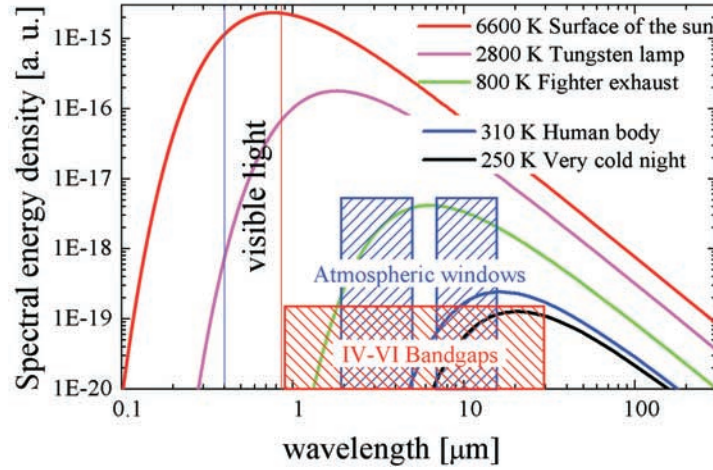
Figure 1.2: The IV-VI bandgaps in the infrared spectrum emitted as black body radiation according to Planck's law. Several emission spectra are plotted for different temperatures as indicated in the graph.

In the case of 2D layered growth, such heterostructures offer a changed density of states for the electronic energy levels due to the 2D confinement in the *quantum well*. Together with a high epitaxial growth quality, these IV-VI compounds lead to one of the first quantum well lasers [7]. These tunable lasers promise to achieve extremely low threshold currents and high optical efficiency up to the near infrared, therefore being of considerable interest for optoelectronic communication technology. The efforts made in the growth of these multilayered systems also led to the discovery and the production of thermoelectric devices with higher efficiency than the bulk materials in the temperature regime between 400 and 550 K. It is indeed expected that further developments in this field will supply the most efficient thermoelectric thin film materials known [8]. The structural congruence of the lead and europium chalcogenides also permits the growth of highly perfect multilayers of alternating diamagnetic and magnetic material. As *e.g.* EuSe is *metamagnetic*, *i.e.* showing various magnetic phases such as ferro-, antiferro-, and ferrimagnetism, the heteroepitaxial strain can be a tool to tune the properties of this magnetic semiconducting material.

IV-VI semiconductor quantum dots In epitaxial systems with a sufficient mismatch between the crystal lattices, a fundamental growth instability leads to the formation of islands on top of a perfect crystal surface. If these self-organized islands are small enough to correspond to the de-Broglie wavelength of a conduction electron, it defines new discrete energy levels for electrons or holes in these structures. In this case the islands behave like *artificial atoms* and are called *quantum dots*. Their application

can range from quantum dot lasers [9, 10] to possible devices in future computer architecture or in quantum computing systems [11].

SiGe nano-islands   In the SiGe system, the deposition of Ge on Si(001) also leads to a formation of islands. In some cases they are too large to act as quantum dots but still offer the opportunity to serve as 2D confined quantum wells. In this case the growth permits a dislocation free formation of SiGe islands with a Ge content that cannot be achieved in a high quality SiGe continuous film on a Si substrate. As Si and Ge both crystallize in the diamond structure, they are completely miscible in all compositions and form a disordered alloy. For confinement effects, interdiffusion is however undesirable. As the growth of islands is a process far from thermodynamic equilibrium, a detailed theoretical prediction of the interdiffusion behaviour driven by entropy and minimization of the elastic energy is difficult.

In any further development in these areas of material science a detailed knowledge about the structural properties as *strain* and *interdiffusion* at interfaces is required. For both of these, high resolution x-ray diffraction is the tool of choice. In particular, the anomalous x-ray scattering technique can supply a unique opportunity to separate the influences of strain and interdiffusion on the diffraction pattern. The present work introduces two techniques, one is suited for the material discrimination in compounds as the IV-VI semiconductors and the other deals with composition resolution in disordered alloys as SiGe.

The tool

Anomalous x-ray scattering   This work deals about a particular application of x-ray diffraction to the study of nanometer sized crystals. We use the "anomalous scattering behaviour" of atoms when the energy of the scattered x-ray photons is close to a resonant energy of an absorption edge. Physically, it is hard to justify the use of the expression *anomalous* for this resonant behaviour. From current view of electromagnetism and matter, this resonant behaviour is seen as normal and for purely historical reasons we refer to it as the *anomalous* scattering in the case of x-rays and their interaction with atoms [16]. It is even notable that in the case treated here, a quantitative description of the resonant response of atoms to the electromagnetic oscillations of the x-rays is possible by classical descriptions; the use of the driven harmonic oscillator description only has to be justified via the existence of discrete energy levels in the

atomic shell structure. The resonance is part of sensation and supplies the colours of our world. As the colours visible by the human eye are caused by electromagnetic resonances, such colour effects also exist in a regime of electromagnetic waves high above the visible frequencies. The "colours" of the atoms as seen by electromagnetic waves at x-ray energies are exploited in this work as a tool for element specific diffraction. The application of x-ray scattering methods to the structural analysis of semiconductor multilayers and nanocrystals grown on perfect crystal surfaces is one important step in the understanding of fundamental epitaxial growth processes. Due to the elemental sensitivity the anomalous diffraction technique can answer questions concerning interdiffusion processes in epitaxial growth.

Object and structure of this work

The objective of this work is the development and advancement of x-ray diffraction techniques that can resolve strain and composition independently. To increase the number of accessible atomic absorption edges, the x-ray energy that was used for diffraction experiments was extended to the low-energy regime in the vicinity of 2500 eV. Low energies permit the excitation of resonances of outer electron shells, usually yielding stronger anomalous effects than the K-shells. Generally in diffraction lattice parameters are probed. Therefore interfaces are defined by either compositional changes or changes in the strain state. Being material selective, the anomalous diffraction methods presented here are highly sensitive to *chemical* interfaces, rather than changes in the lattice parameter. The role of interdiffusion in epitaxial processes and the formation of quantum dots is still under discussion [12] as the driving force for interdiffusion and alloying can differ fundamentally between different material systems [13, 14].

Therefore anomalous x-ray diffraction shall be employed in order to resolve quantitatively the composition and strain profile in quantum dots and 2D heterostructures. The tasks related to this topic and the material systems presented before are:

- Seperate determination of the out-of-plane lattice parameters in multilayers of lead-/europium chalcogenides.

- The influence of strain tuning in EuSe by different alloys of $PbSe_{1-x}Te_x$ in $PbSe_{1-x}Te_x$/EuSe multilayers.

- Clarification of the influence of Eu in $Pb_{0.92}Eu_{0.08}Te$ capping layers on top of PbSe nano pyramids.

- Determination of the strain and composition profiles in SiGe islands on Si(001). Complementary methods of reciprocal space mapping, anomalous diffraction and selective etching will be employed here, to study also the influence of the growth temperature on the Ge-concentration in the islands.

The work is **structured** as follows:

- To quantify the results obtained from the diffraction experiments, a mathematical review of the kinematic diffraction conditions will be given. Furthermore, the quantitative treatment of the atomic scattering factor in the vicinity of absorption edges is introduced. We will focus our interest on the peculiarities of truncated epitaxial systems and the importance of the *phase* of the complex atomic scattering factor.

- The derived expressions and equations in 2D systems are used to describe a selection of anomalous scattering effects that are of importance in the data evaluation.

- The experimental part will start with the explanation of the equipment that was developed for experiments at low x-ray energies. Special attention will be given to the calibration of an anomalous diffraction experiment, which includes the absolute measurement of the atomic scattering factors in elemental crystals and the relative determination of these factors in compound crystals.

- The experiments concerning the aims outlined above follow in the last part. The methods of anomalous diffraction will be applied to 2D multilayers of IV-VI compound crystals as PbSe/EuSe. Anomalous grazing incidence diffraction will be applied to the SiGe system. In a further experiment anomalous reciprocal space mapping is exploited to determine the facet orientation and transformation

in PbSe quantum dots grown in 3D superlattices. The influence of the overgrowth with either PbTe or $Pb_{0.92}Eu_{0.08}Te$ on the interdiffusion of the islands is studied.

"By convention sweet is sweet, by convention bitter is bitter, by convention hot is hot, by convention cold is cold, by convention color is color. But in reality there are only atoms and void. That is, the objects of sensation are supposed to be real and it is customary to regard them as such, but in truth they are not. Only the atoms and the void are real."
Demokrit, 460-371 B. C.
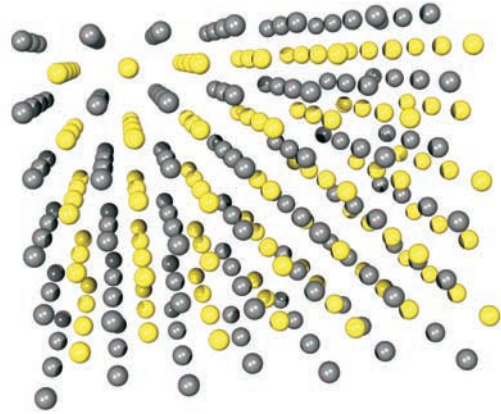
2   Theoretical treatment of kinematic and anomalous diffraction

The fundamental question of obtaining information about a physical system via an indirect method has been applied in diffraction physics for more than a century. Indirect methods were often seen as last resort techniques, where no other tool could supply the required information. In the case of diffraction, the reverse development took place in the 20th century. For simple mathematical reasons it allows for the determination of frequencies in a periodic space of interaction. As most of the condensed matter around us is found to be in a crystallized state this periodic space is supplied by nature and its spatial frequencies are the reciprocal distances between the atoms. The resolution of these distances down to a precision of 5 digits is far beyond the performance of any direct microscopy technique. It is indeed the precise determination of lattice parameters which makes diffraction an interesting tool for epitaxial systems. Here one often deals with several crystals with a slight lattice mismatch. To resolve small strain gradients, diffraction becomes the tool of choice. In this work, diffraction will be applied to artificial systems as *e.g.* highly perfect layers only a few atomic monolayers in thickness. It will be shown that in these particular systems, diffraction offers a mathematically manageable tool, as the description can be performed in a straightforward way if certain experimental boundary conditions are fulfilled. In the following sections we will clarify these conditions and apply solutions of the diffraction mathematics to our material systems investigated in this work.

2.1 Mathematical considerations of diffraction

2.1.1 The conditions for diffraction

One of the standard textbooks of optics [15] introduces diffraction as "the most diffi-cult problem in optics". Optics in general describes the propagation of electromagnetic waves, using the notation of "geometrical optics" in the form of ray-tracing, or wave optics in the case where diffraction has to be described. To justify any mathematical treatment or simplification used in this work, we have to consider the conditions un-der which we perform diffraction experiments. As a starting point we treat X-rays as "classical" waves with a wavelength λ and an amplitude A. In order to describe the directional property of the wave propagation, λ will often be included in the wavevector $\vec{k}$ which points in the propagation direction and has the magnitude $\frac{2\pi}{\lambda}$. λ and A are parameters that define the space- and time dependent wavefunction $\Psi\left(t, \vec{k}\vec{r}\right)$. The ju-stification of the use of a wave function shall not be treated here; it results as an ansatz for a solution of the wave equation in classical electrodynamics. For simplification, we will always treat $\Psi\left(t, \vec{k}\vec{r}\right)$ as a monochromatic plane wave. Deviations will later be introduced and will only lead to quantitative rather than qualitative corrections. With these fundamental properties of light, we can now further simplify our description of diffraction if certain conditions are fulfilled. In the particular case of x-ray diffraction, we often deal with the so called *far field case* or *Fraunhofer approximation*, where

$$\lambda * L >> d^2 \tag{2.1}$$

is satisfied. d describes the width of the *coherently* diffracting object, whereas L des-cribes the distance between the object and the point of observation. The size of the coherent scattering region is either determined by the beam-size itself, the coherence length of the beam (i.e. the region over which the phase of the wavefield is well-defined) or the size of the parts of the sample which scatter coherently. In the experiments dis-cussed later we will always deal with the latter two conditions. The condition 2.1 can also be called the "monochromatic plane wave condition", as due to the size of the diffracting object and the far distance of the observation point, the phase-shift of the wavefield inside the object caused by the curvature of the wavefront, can be neglec-ted. In addition, the finite bandwidth $\Delta\lambda$ causes a phase-shift $\Delta\Phi$ in the propagation direction through the coherently diffracting object which is smaller than π. For a ty-pical wavelength $\lambda = 1$ Å and a sample-detector-distance of $L = 1$ m, Eq. (2.1) is fulfilled for diffracting objects significantly smaller than 10 μm. This is much larger than the size of the monocrystalline regions of all objects investigated in this work. The bandwidth $\Delta\lambda$ affects the coherence condition in the propagation direction. Two

waves with wavelengths λ and $\lambda + \Delta\lambda$ suffer after a propagation length of l a phase-shift $\Delta\Phi = \left(\frac{l}{\lambda} - \frac{l}{\lambda + \Delta\lambda}\right) 2\pi$. If we define a phase-shift $\Delta\Phi$ between these waves as the "loss-of-coherence" condition, we can approximate the *longitudinal coherence length l_c* as

$$l_c \approx \frac{\lambda^2}{2\Delta\lambda} \tag{2.2}$$

An analogue can be defined to derive an expression for the coherence length in directions perpendicular to the propagation direction. In that case we use the term *transverse coherence length*. We describe it with a similar geometrical justification, the phase difference of $\Delta\Phi = \pi$ between two points on the wavefront. The finiteness of the transverse coherence length is caused by a deviation of our wavefront from the perfect plane wave. A divergent beam causes our wavefront to be curved, and we have to ask the question "up to which divergence can we describe the wavefront as flat?". To answer it, we select a certain point on a maximum of our wavefront that we consider as flat. If we now move along the wavefront, perpendicular to the propagation direction, we expect to stay on the maximum of a plane wave. As our wavefront is curved however, we move down in a valley instead and lose the maximum. It appears reasonable to define the part of our wavefront to be considered as "flat", where we still find at least half of the maximum value of positive undulation. In other words, we can move upwards or downwards in transverse direction until we have reached a phase-shift of $\frac{\pi}{4}$. Considering Fig. 2.1 we can state for the transverse coherence length t_c:

$$\left(\frac{t_c}{2}\right)^2 = \left(L_1^2 - L_0^2\right)^2 = (L_1 + L_0)(L_1 - L_0) \tag{2.3}$$

and as we defined above $(L_1 - L_0) = \frac{\lambda}{8}$ we can approximate

$$\left(\frac{t_c}{2}\right) = \frac{2L_0}{\frac{t_c}{2}}\frac{\lambda}{8} \tag{2.4}$$

therefore we can define the transverse coherence length t_c for small divergences ϵ:

$$t_c = 2 * \frac{2}{\tan\frac{\epsilon}{2}}\frac{\lambda}{8} \approx \frac{\lambda}{\epsilon} \tag{2.5}$$

These considerations will be important if we want to investigate long range ordered nanostructures. In this case, the size of the coherently scattering object might extend to the same lengthscale as the coherence of our experimental setup. In most of the cases discussed later, however, the size of the scattering crystals will be significantly smaller than the coherence lengths defined in eqs. (2.2) and (2.5).
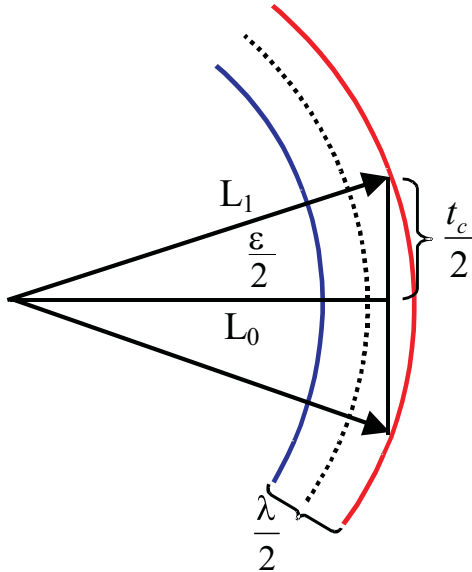
Figure 2.1: Sketch of a curved wavefront and its limitations to the plane wave description

If in addition Eq. (2.1) is fulfilled, we can work with a plane monochromatic wave and our scattered intensity is simply described by a Fourier integral over the spatial electron distribution in our diffracting crystal.

2.1.2 From diffraction to Fourier transforms

In a general diffraction experiment, we observe the scattered intensity distribution caused by the spatial distribution of the light scatterers. If we consider our incident and scattered waves to be parallel and monochromatic, we can describe the incident wave as

$$\Psi\left(t, \vec{k_i}\vec{r}\right) = \hat{A}e^{i\left(-\vec{k_i}\vec{r}+\omega t\right)}, \tag{2.6}$$

where $\hat{A}$ describes the amplitude and ω the frequency of the electromagnetic oscillations. If we consider only a finite number of point scatterers at N locations $\vec{r}_j$, we have to sum up the waves scattered in these points. For the summation, the point of observation P plays a crucial role, as it determines the phase relation of the scattered waves (*e.g.* which wave arrives first at P). For that reason we should mention that it is always possible to add a phase ϕ to a travelling wave as in Eq. (2.6). We could change (2.6) to be $\Psi\left(t, \vec{k_i}\vec{r}\right) = e^{i\left(-\vec{k_i}\vec{r}+\omega t+\phi\right)}$. As ϕ only leads to an offset of the origin of the oscillations, it can be chosen arbitrarily if we only look at *one* wave. We therefore chose it to be zero for the incident wave Ψ. If we now consider our ensemble of scatterers at r_j, we note that for any chosen observation point P we get a certain phase ϕ_j for the scattered wave Ψ_j from the point scatterer j according to its spatial position at r_j.

These phases can no longer be chosen but lead to interference phenomena observed at P between all N Ψ_j. If P is "far away" according to Eq. (2.1) the phase-shifts between the Ψ_j is caused by their relative distance in space projected on the propagation direction of the incident wave and onto the direction pointing towards P. This is sketched in Fig. 2.2.
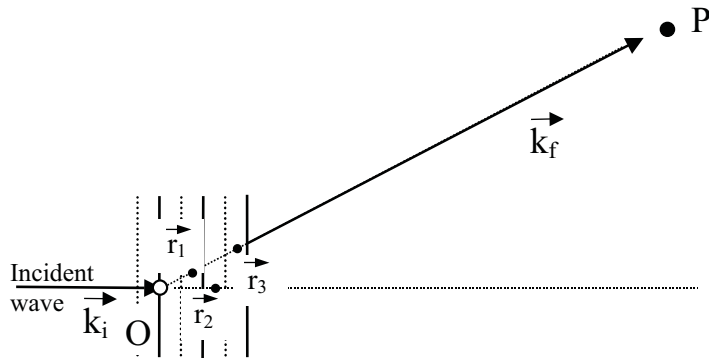

Figure 2.2: The spatial arrangement of the point scatterers r_j causes a well defined phase relation for the interference of the scattered waves from all r_j.

The wave propagating in direction $\vec{k}_i$ arrives with a different phase shift with respect to the origin O at every point scatterer r_j. This phase shift is proportional to the distance from r_j to O projected onto the propagation direction $\vec{k}_i$. If we only look at scattered waves in a certain direction $\vec{k}_f$ defined by our observation point P, we observe another phase shift between O and r_j, depending on their distance projected onto $\vec{k}_f$. For the interference between waves scattered at e.g. O and any r_j, the phase difference would be the sum of both. The simplest example would be $\vec{k}_i = \vec{k}_f$ for forward scattering. Both phase shifts would be of the same magnitude with opposite signs. The phase shift would be zero and therefore the interference for forward scattering is always constructive. For all other directions, we measure certain phase relations that refer to the spatial arrangement of our scatterers. As no experiment can resolve the rapid oscillations described by ωt in Eq. (2.6), one only measures the intensity I as the absolute square of the coherent sum of all amplitudes Ψ_j:

$$I = <| \sum_{j=1}^{N} \hat{A}_j e^{i\left(-\vec{k}_i \vec{r}_j + \omega t + \vec{k}_f \vec{r}_j\right)} |^2>_t = <| \sum_{j=1}^{N} \hat{A}_j e^{i\left(\vec{k}_f - \vec{k}_i\right)\vec{r}_j} e^{i\omega t} |^2>_t = | \sum_{j=1}^{N} \hat{A}_j e^{i\left(\vec{k}_f - \vec{k}_i\right)\vec{r}_j} |^2$$

(2.7)

$< \ldots >_t$ denotes the time average that eliminates the oscillating time dependent part $e^{i\omega t}$. Equation (2.7) is already the discrete Fourier transform of the spatial arrangement of our point-scatterers' scattering potential from the space referred to by the $\vec{r}_j$ into the $\left(\vec{k}_f - \vec{k}_i\right)$ space. We therefore call $\vec{Q} = \left(\vec{k}_f - \vec{k}_i\right)$ the momentum transfer and refer

to it as the $\vec{Q}$-space. We could express the same problem analytically via expressing the scattering potential as a scattering density function $\rho(\vec{r})$ in which we produce the point like nature of our scatterers with delta functions:

$$\rho(\vec{r}) = \sum_{j=1}^{N} \hat{A}_j \delta(\vec{r}_j)$$
$$I = \mid \int \rho(\vec{r}) e^{i\vec{Q}\vec{r}} \vec{dr} \mid^2 \tag{2.8}$$

The scattering amplitude $A\left(\vec{Q}\right) = \int \rho(\vec{r}) e^{i\vec{Q}\vec{r}} \vec{dr}$ is therefore simply described by the Fourier transform into the $\vec{Q}$-space of the scattering density $\rho(\vec{r})$ in real space. It is worth looking at some helpful formulas concerning the Fourier transforms, as we will deal with them in the following chapters.

2.1.3   Fourier transforms: Useful relations and Babinet's principle

As we know that we probe the Fourier space of an object in a diffraction experiment, it will be helpful to think about basic relations between real- and reciprocal (Fourier) space. We will focus our interest to those relations which are of special use for the diffraction calculations and experiments performed later. Suppose we consider the Fourier transform (FT) $A\left(\vec{Q}\right)$ of an electron density distribution $\rho(\vec{r})$. Then we may take advantage of the following relations:

1. Linearity: The FT of $\rho(\vec{r}) = f(\vec{r}) + g(\vec{r})$ is

$$FT[f(\vec{r}) + g(\vec{r})] = FT[f(\vec{r})] + FT[g(\vec{r})] \tag{2.9}$$

The proof is evident when evaluating the integral 2.8. The usefulness of the linearity is evident in the description of *e.g.* a heteroepitaxial real space, build up of a summation over different materials.

2. Inversion symmetry: The FT of the inverted real space is the FT of the non-inverted original real space with inverted reciprocal coordinates:

$$FT[\rho(-\vec{r})] = A\left(-\vec{Q}\right) \tag{2.10}$$

In the same manner as before, this is proven by simply writing out the integral. This inversion symmetry is of great interest in anomalous diffraction for structure resolution[17]: The sign inversion is done by *e.g.* looking at the reflections (111) and $(\bar{1}\bar{1}\bar{1})$ for $\vec{Q}$ and $-\vec{Q}$. If our unit cell is centro-symmetric in real space, those two reflections look the same. If it is not, we can apply anomalous scattering and change the appearance and intensity of a pair of reflections. Such pairs are named "Friedel-pairs". Performing anomalous scattering at one element and probing various Friedel pairs, we can derive the positions of the probed element in the unit cell [18].

3. Translation in real space: Suppose we translate an object in real space by a certain distance $\vec{u}$ and we want to calculate the FT of $\rho(\vec{r} - \vec{u})$. We might then substitute $(\vec{r} - \vec{u})$ by $\vec{U}$ and $d\vec{r}$ by $d\vec{U}$ as $\frac{d\vec{U}}{d\vec{r}} = 1$. The FT 2.8 then reads

$$
\begin{aligned}
A\left(\vec{Q}\right) &= \int \rho\left(\vec{U}\right) e^{i\vec{Q}(\vec{U}+\vec{u})} d\vec{U} \\
&= \int \rho\left(\vec{U}\right) e^{i\vec{Q}\vec{U}} e^{i\vec{Q}\vec{u}} d\vec{U} \\
&= e^{i\vec{Q}\vec{u}} FT\left[\rho\left(\vec{U}\right)\right]
\end{aligned}
\tag{2.11}
$$

A translation by $\vec{u}$ in real space therefore corresponds to a multiplication by $e^{i\vec{Q}\vec{u}}$ in reciprocal space.

4. The convolution theorem: Consider the scattering density to consist of a convolution of two functions f and g:

$$
\rho(\vec{r}) = \int f\left(\vec{\xi}\right) g\left(\vec{r} - \vec{\xi}\right) d\vec{\xi}
\tag{2.12}
$$

Again we make a substitution $\vec{r} - \vec{\xi} = \vec{U}$ and derive for the FT of $\rho(\vec{r})$:

$$
\begin{aligned}
A\left(\vec{Q}\right) &= \int \int f\left(\vec{\xi}\right) g\left(\vec{\xi} - \vec{r}\right) d\vec{\xi} e^{i\vec{Q}\vec{r}} d\vec{r} \\
&= \int \int f\left(\vec{\xi}\right) g\left(\vec{U}\right) d\vec{U} e^{i\vec{Q}(\vec{U}+\vec{\xi})} d\vec{\xi} \\
&= \int g\left(\vec{U}\right) e^{i\vec{Q}\vec{U}} d\vec{U} \int f\left(\vec{\xi}\right) e^{i\vec{Q}\vec{\xi}} d\vec{\xi}
\end{aligned}
\tag{2.13}
$$

Therefore the Fourier transform of a convolution between f and g is the product of their Fourier transforms:

$$
FT\left[f(\vec{r}) * g(\vec{r})\right] = FT\left[f(\vec{r})\right] \bullet FT\left[g(\vec{r})\right]
\tag{2.14}
$$

As the Fourier transform is a bijective operation, the inverse holds true, as well: The Fourier transform of a product is a convolution of the Fourier transforms of the factors.

5. Babinet's principle: Babinet's principle originally deals with the diffraction pattern observed from two complementary apertures. In classical optics this is the typical question that arises if we invert *e.g.* a diffraction grating: Suppose we have N slits with a spacing d in between and a slit width a. Then the inverted aperture would consist of N slits with a spacing d in between and slit width $(d-a)$. What is now often applied as the "Babinet's principle" is the statement that the diffracted intensity distribution of such inverted apertures is equal. [19, 20] It is of crucial importance for the investigations performed in this work, that this statement is wrong. Already a qualitative argument says, that the integrated intensity must be different, as our transmission density (as an analogue for the scattering density ρ treated so far) for the transparent parts is unity, we have a larger transmitting aperture in the second case, if $d > 2a$. Let's consider a

grating in 1 dimension where $a << \frac{d}{2}$. We can describe this real space structure with a sum of N delta functions of the form $\sum_{j=1}^{N} \delta (x - j * d)$. This sum is convoluted with the slit function, that is unity between $-\frac{a}{a}$ and $\frac{a}{a}$ and zero elsewhere. Then we know from Eq. (2.14) that its Fourier transform is the product of the Fourier transforms of the grating sum and the slit function. The latter is a textbook example (*e.g*) [15] for diffraction, its Fourier transform has the form

$$\frac{\sin \frac{Qx}{2}}{\frac{Qx}{2}}. \tag{2.15}$$

This is now multiplied with the oscillations defined by the grating spacing d. Consequently, Eq. (2.15) is enveloping this oscillating grating diffraction function. The grating is the same for both complementary apertures, but the width of the transparent slits changes. It is known that Eq. (2.15) shows a central maximum with a half-width that corresponds to the reciprocal value of the slit size. In both complementary cases the slit size is different, a or $d - a$ but both are smaller than d. The reciprocal distance of the grating diffraction peaks is therefore smaller than the width of the central maximum of the envelope function. In this case, we have different envelopes in the vicinity of the origin and the diffracted intensities are qualitatively different for the complementary apertures. Figure 2.3 shows diffraction patterns for two complementary apertures for $N = 10$, $a = 30$, $d = 100$ in (a) and $N = 10$, $a = 70$, $d = 100$ in (b). The dotted envelopes represent the slit diffraction function according to Eq. (2.15).
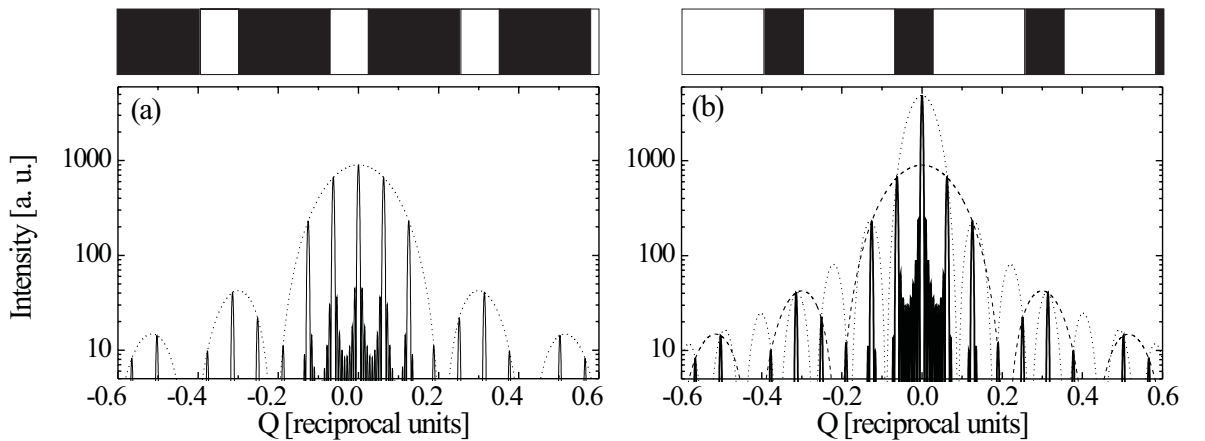
Figure 2.3: (a) Diffraction pattern from grating of N slits of width $a = 30$ and a grating constant $d = 100$. (b) Diffraction pattern from the aperture complementary to the one in (a). The Fraunhofer diffraction functions from a single slit are plotted for both apertures as dotted lines. In (b), the envelope function from (a) is added as a dashed line for comparison.

A close look at Fig. 2.3 shows that indeed all grating peaks are of the same intensity with the central one as the only exception. All others are enveloped by both slit diffraction functions.

2.2 X-ray scattering from materials

This section will give a brief review of the fundamental interactions between charged particles (electrons) and electromagnetic waves. This leads to a qualitative understanding of the "anomalous" scattering behaviour in the vicinity of absorption edges.

2.2.1 Elastic and inelastic scattering of light by charged particles

In this first section about light-matter interaction, the most important aspect for diffraction is reviewed: the scattering of light (photons) without energy losses *i.e.* without changing the wavelength of the wave, or without annihilation or creation of photons inside the interaction volume. It is known from fundamental electromagnetic theory, that accelerated charges emit radiation (see *e.g.* [21]). Classically, the acceleration $\vec{a}$ is given by the Lorentz force of the oscillating electromagnetic field from the incident wave $\vec{E}e^{i\omega t}$ acting on a charge e with mass m:

$$\vec{a} = \frac{e}{m}\vec{E}e^{i\omega t} \tag{2.16}$$

The field vector irradiated by an accelerated charge is proportional to this acceleration and its charge:

$$\vec{E}_i = \frac{e}{m}\vec{E}e^{i\omega t} * e\frac{\cos\phi}{c^2 R} \tag{2.17}$$

R denotes the distance from the observation point to the radiating charge, $\cos\phi$ is the polarization correction for the angle ϕ between the propagation direction to the observation point, and the oscillating direction of the charge e. It is important to note that in Eq. 2.17, the irradiated field is proportional to $\frac{e^2}{m}$. As the experimental observable is the intensity $I \propto |E|^2$, it depends on $\frac{e^4}{m^2}$. We can already state that the elastic nuclear scattering is about a factor of 1836^2 smaller than the scattering contribution from the electrons of an atom. In the scattering of x-rays from materials, we therefore can focus on the description of the scattering by the electrons and neglect the contributions of the nuclei. All these considerations are valid for free electrons and are of purely classical nature. They do not take into account the inelastic scattering from a free electron, which is known as *Compton scattering*. In this case, the x-ray photon recoils from an electron and an x-ray photon of lower energy is scattered from the electron. This energy is transferred to the electron with conservation of momentum. The energy loss of the photon ΔE and the cross section $\frac{\delta\sigma}{\delta\Omega}$ of this process are given by [22]:

$$\Delta E = \frac{\frac{E_0}{m_e c^2}(1-\cos\theta)}{1+\frac{E_0}{m_e c^2}(1-\cos\theta)} \tag{2.18}$$

$$\frac{\delta\sigma}{\delta\Omega} = \frac{r_e^2 \left(1 - \cos^2\theta\right)}{2\left[1 + \frac{E_0}{m_e c^2}\left(1 - \cos\theta\right)\right]^2} \tag{2.19}$$

r_e is used here as an abbreviation for $\frac{e^2}{mc^2}$ and is also called the classical electron radius. Equation (2.19) is an approximation derived employing relativistic quantum mechanics. Its use can be justified for x-ray energies below 100 keV [23]. The important point here is that the cross section (2.18) depends on the scattering angle. Compton scattering might be negligible for small angles, but becomes more important for higher angles. In a diffraction experiment this means that we expect increasing background contribution in angular space. The treatment in this chapter has been performed for the ideal case of free electrons. Dependent on the x-ray energy and the element, most of the electrons in a material can be considered as quasi-free. Therefore we can use these qualitative approaches if the x-ray energy is far from the resonant energies of bound states.

2.2.2 Resonant behaviour

In the case where we consider an electron as being in a bound state, the response to the exciting wavefield is not as simple as in Eq. (2.17). It is however still possible to apply a classical treatment. The extremely high frequency of x-rays, typically in the range of $10^{18} s^{-1}$, by far exceeds all plasma frequencies from metals. Therefore, all materials can be treated as dielectric. The Drude model applies the classical treatment of the harmonic oscillator to the dynamic polarization of materials. If we apply this assumption to the electrons of a material (as discussed before, the acceleration effect of the nuclei will be negligible), the exciting field $E = E(t)$ acts on the electron cloud with a mass density ρ_m and a charge density ρ_e and deviates them from their equilibrium distribution around the nucleus. This is described by the dipolar amplitude or elongation s. The acting force to reinstall the equilibrium is defined by B. As the electrons will follow the oscillations of the field E, regardless of their eigenfrequency, the 1-dimensional undamped driven oscillator equation reads:

$$\rho_m \ddot{s} + Bs = \rho_e E \tag{2.20}$$

As mentioned before, inelastic processes always exist, even in the free electron treatment. Even if we may not be able to quantify them in a simple way, we have to respect them as a damping factor that has to be added on the left-hand side of Eq. (2.20) as known from mechanics. Without further knowledge of its origin we call this damping factor γ. In addition, it appears more descriptive to replace the product of our dipolar

amplitude and the charge density by the polarizability $P = \rho_e s$. The eigenfrequency of the unperturbed system is also known to be $\omega_0 = \sqrt{\frac{B}{\rho_m}}$. This changes Eq. (2.20) to

$$\ddot{P} + \omega_0^2 + \gamma \dot{P} = \frac{\rho_e^2}{\rho_m} E. \tag{2.21}$$

To solve this differential equation for P, it is useful to apply the Fourier transform from time into frequency space for the time dependent variables E and P:

$$E(t) = \int e^{-i\omega t} E(\omega) \, d\omega \tag{2.22}$$

$$P(t) = \int e^{-i\omega t} P(\omega) \, d\omega \tag{2.23}$$

With eqs. (2.22) and (2.23) applied to (2.21) and some simple mathematics we have:

$$\left(-\omega^2 - i\gamma\omega + \omega_0^2\right) P(\omega) = \frac{\rho_e^2}{\rho_m} E(\omega) \tag{2.24}$$

We have transformed a differential equation into an algebraic but *complex* equation. The polarization P is the response to the field E of a material with the polarizability χ. If we state $P(\omega) = \chi E(\omega)$ we can deduce from Eq. (2.24) for χ:

$$\chi(\omega) = \frac{\frac{\rho_e^2}{\rho_m}}{\omega_0^2 - \omega^2 - i\gamma\omega} \tag{2.25}$$

Therefore, it follows from the basic mathematical treatment applied in eqs. (2.21)-(2.25) that $\chi(\omega)$ as an response function from a material has a complex solution. χ is also called the dielectric susceptibility. The main problem in the theoretical description of χ is the precise knowledge of ω_0 and γ. It might be easy to measure resonance frequencies, as the driven oscillator shows a maximum of energy absorption per cycle if excited with the resonant frequency. However there is no straightforward way to measure γ. In classical electro dynamics, the causality principle can be used to derive a relation between the real and the imaginary part of χ [21]. These relations are called the Kramers-Kronig dispersion relations. With χ' as the real part and χ'' as the imaginary part of χ these relations are:

$$\chi'(\omega) = \int_0^\infty \frac{\omega' \chi''(\omega')}{\omega'^2 - \omega^2} d\omega' \tag{2.26}$$

$$\chi''(\omega) = -\int_0^\infty \frac{\chi'(\omega')}{\omega'^2 - \omega^2} d\omega' \tag{2.27}$$

In this work, we will particularly use Eq. (2.26). As the imaginary part of the dielectric susceptibility describes the absorption, it is possible to measure it under relatively simple experimental conditions. The trade-off, however, is the fact that we have to

know the absorption behaviour for all frequencies in order to derive the real part. In the case of atomic resonances, χ' and χ'' are represented by the anomalous corrections f' and f'' to the atomic form factor. The theoretical description of f' and f'' is based on self-consistent equations describing the atom as a multi-electron system [24]. The structure of Eq. (2.26) shows that the derivation of f' from f'' is particularly sensitive to the behaviour of $f''(\omega)$ in the vicinity of the values for ω where we want to find out our precise behaviour of $f'(\omega)$. In anomalous scattering, this region of interest is an absorption edge, and it is important to know the detailed structure of $f'(\omega)$ and $f''(\omega)$ across this region. As measurements of $f''(\omega)$ from $\omega = 0$ up to $\omega = \infty$ are not feasible, it is possible to perform a high resolution measurement of $f''(\omega)$ in the region of interest, and use tabulated theoretical descriptions for the remaining parts of the integrand in Eq. (2.26). This procedure will be presented and exemplified later in section 3.4.1. From these derivations we keep in mind that x-rays are scattered by the electrons of an atom. To respect the existence of bound states, we applied the harmonic oscillator picture to describe the resonant behaviour if the x-ray energy is close to the binding energy of an electron. Due to the shell structure of the electron system, resonances affect in general only a small fraction of the electrons of an atom. The resonance correction terms taking into account the dispersion as represented via χ' and χ'' in eqs. (2.26) and (2.27) are added as f' and f'' to the expected *normal* scattering power f_0 of an atom:

$$f = f_0(Q) + f'(E) + if''(E) \tag{2.28}$$

$f_0(Q)$ is generally proportional to the number of electrons of an atom. As units for f we use *electron units*. In these units, f_0 fulfills the equivalent of $f_0 = Z$ for forward scattering, *but decreases for higher scattering angles or momentum transfers Q.*

2.2.3 Behaviour of the atomic scattering factor at the accessible edges

The resonant energies accessible for x-ray scattering are generally the K- or L-edges. This of course depends on the location in the periodic table of the considered element and on our definition of the x-ray regime. From the crystallographic point of view, this regime will have a limit at the low energy side: the x-ray wavelength λ still has to allow us to excite a Bragg reflection from a crystal. We therefore look at the Bragg condition for positive interference between netplanes with Miller indices h, k, l:

$$\frac{\lambda}{2} = d_{hkl} \sin\theta \tag{2.29}$$

For lower x-ray energies, λ and therefore the left side of Eq. (2.29) gets larger. The right side increases with the Bragg angle θ and the netplane spacing d_{hkl}. As $\sin\theta$ cannot

become larger than 1, no wavelength larger than $2d_{hkl}$ can be used to excite the (hkl) reflection. We may take Si as a typical example where the lowest indexed reflection is the (111) reflection with a d-spacing of $d_{111} = 3.135$Å. This sets the upper wavelength limit to 6.27 Å and therefore the lowest x-ray energy to diffract from the Si-(111) is 1977 eV. Of course there are crystals with higher d-spacing. Without trying to find the most exotic example we state that somewhere around 2000 eV we can set the lower limit for energies in crystallography. In most of the available experimental setups used for diffraction, however, the usual lower enery limit is around 5000 eV. The fact that air and almost any other material becomes a strong absorber in the energy regime below 5000 eV often prevents the use of the whole range suited for crystallography. Figure 2.4 gives an overview over the accessibility of edges in the periodic table.

Figure 2.4: Periodic table and absorption edges of the elements: For x-ray energies above 2000 eV, anomalous scattering is possible on K-edges from P (Z=15) up to all heavier elements. The elements where only the K-edge is accessible are highlighted in red. Elements where K-edge and L-edges can be reached are highlighted in blue. The elements in magenta have K-, L- and M-edges (from Ir (Z=77) even the M_V-edge) above 2000 eV.

For all elements that have absorption edges in the accessible energy range, anomalous scattering can be applied. Elements with atomic number up to 14 (Si) have K-edges below 2000 eV and are therefore not suited for anomalous diffraction. From P (Z=15)

to Kr (Z=36), the only absorption edge above 2000 eV remains the K-edge. From Rb (Z=37) upwards, one can reach L-edges, and from Dy (Z=66) M-edges are accessible. For the outer electron shells, more electrons can contribute to the resonances, and the anomalous corrections f' and f'' are more important at L- or M-edges than at the K-edge.

As an example for the various absorption edges, one might look at two extreme examples: a light element and a heavy element. In the case of sulfur (S), one can only access the K-edge at 2472 eV. Due to the low number of electrons (Z=16) however, the relative anomalous effect on $|f|$ can be a decrease of 70 % in forward scattering. In lead (Pb), we have access to the M_V-edge at 2500 eV. Here we have a particularly strong resonance and the scattering of Pb decreases to 35 electron units for forward scattering. This is a relative anomalous decrease of almost 60 %. At the Pb-L_{III}-edge (13040 eV) the relative effect amounts to 22 %, at the Pb K-edge (88000 eV) this effect is still of the order of 13 %. In both cases, the absolute resonant decrease of $|f|$ at the K-edge was about 11 electron units. Simply the lower number of electrons of the Sulfur atom leads to a much higher relative anomalous effect. For heavy elements this can in general be compensated if we go to higher energies. The values of $|f|$ for Pb and S are plotted in Fig. 2.5(a), together with the relative anomalous effect in (b).
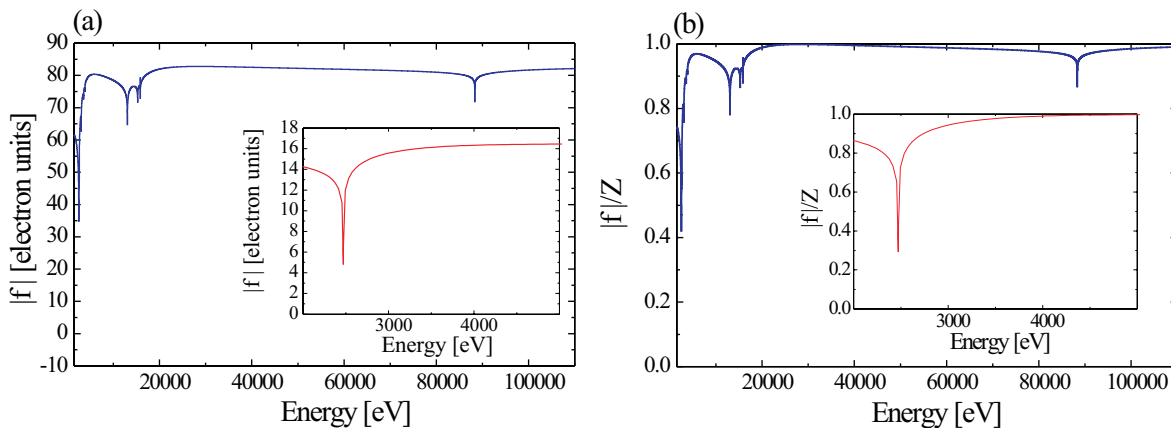
Figure 2.5: (a) $|f|$ for Pb (blue line) and S (red line, inset). (b) relative anomalous effect for Pb and S.

2.2.4 Momentum dependence of the atomic scattering factor

The anomalous effects, the behaviour discussed previously and plotted in Fig. 2.5, are valid in the forward scattering direction. For a further treatment of the scattering in reciprocal or angular space, we have to take a closer look at the origin of the atomic scattering factor. The forward scattering power $|f|$ of an atom is in general (*i.e.* far

away from resonances) proportional to its number of electrons Z. As these electrons are arranged in orbitals that result in a certain spatial charge-density distribution, the atom itself is not a point-like scatterer. If we have a look at Fig. 2.2 in section 2.1.2 and imagine building these electron clouds by a finite number of point-scatterers, we can replace our charge density distribution with a coarse grained charge distribution. All these point-scatterers scatter now with a certain phase shift according to their distance from each other. This spatial phase shift contributes to the incident wave as well as to the scattered wave and they cancel each other only for forward scattering. Analogous to the case discussed in section 2.1.2, we interpret the scattering factor as the Fourier transform of the electron density of an atom. The linearity Eq. (2.9) enables us to consider the Fourier transform of every orbital separately and define their sum to be the complex atomic scattering factor $f = f_0 + f' + if''$. We then sum up all Fourier transforms of all occupied orbitals without any consideration of resonances effects on the scattering factor f_0. Again this factor equals the number of electrons for forward scattering. If we consider resonant effects, we might only look at a fraction of the electrons that contribute. Therefore, we take these into account via the corrections f' and if''. The complex nature of the correction has been discussed in section 2.2.2. It can here also be interpreted as a retarded response of the resonator. We define here the phase shift in time as the *anomalous phase* $\phi = \arctan \frac{f''}{f_0 + f'}$. With the momentum $|f| = \sqrt{(f_0 + f')^2 + f''^2}$, the atomic form factor as a complex number can then be written in the form

$$f = f_0 + f' + if'' = |f|e^{i\phi}. \tag{2.30}$$

Both notations have advantages: the complex notation appears to be a didactically helpful picture of the collective response of the atom as a charge oscillation with a phase shift to the exciting wave. In addition it is a notation which will be better suited for the treatment in analytical solutions as presented in section 2.5.2. The separation into f_0, f' and f'' offers advantages when we consider the Fourier transform of the atomic scattering factor, as diffraction takes place not in forward scattering, but at certain momentum transfers according to the probed reflections. The kinematic intensity of Bragg reflections is known to decrease for higher index reflections. This takes place even if we ignore the effect of temperature vibration in the kinematic theory. This can be explained by the decrease of the Fourier transform of the atomic scattering factor for increasing momentum transfer Q: We simply consider a 1D small crystal, consisting of a periodic linear arrangement of identical atoms F. All these atoms have a certain electron density distribution $\rho(R)$ around their nucleus. Then we can describe the total electron density distribution of this crystal in real space as a sum of delta functions

at the periodic positions convoluted with the aforementioned atomic electron density function $\rho(R)$.

Applying the convolution theorem 2.14, we can now state that the Fourier transform of such a crystal is equivalent to the product of the Fourier transform of the summation over delta functions, and the Fourier transform of the electron distribution of an atom. As infinite integrations over delta functions are easy to evaluate, a simple check of the Fourier transform of such a delta lattice shows that the intensity is equivalent to the square of the number of its lattice sites for all Bragg points. Therefore, the decrease of the Bragg intensities for increasing indices is enveloped by the decrease of the Fourier transform of the electron distribution $\rho(R)$ around the atom. This decrease in reciprocal space gets more dramatic for the outer electron shells which have a more extended spatial distribution than the inner orbitals. As in many cases we consider anomalous effects at the K-edge, this decrease of the Fourier transform might even be negligible up to a certain Q-range. Then we have only to take into account the momentum dependence of f_0, which is *independent* of the x-ray energy. This leads to a useful separation of the scattering factor f into an explicitly Q-dependent and energy independent part f_0, and in the Q-independent, but energy dependent resonance corrections f' and f''. In Fig. 2.6, the momentum dependence of f_0 of Pb (Z=82) is plotted. The maximum values for the momentum transfer at the Pb M_V-, L_{III}- and K-edges are indicated as perpendicular lines.
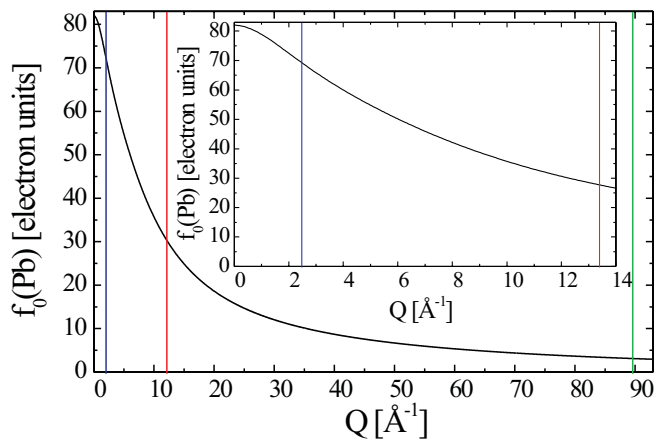
Figure 2.6: Momentum dependence of the atomic scattering factor of Pb. Perpendicular lines mark the achievable momentum transfer at the M_V-edge- (blue line), the L_{III}-edge- (red line) and the K-edge energy (green line). The inset shows a magnification of the momentum range up to the L_{III}-edge.

Indeed one should remark a physical coincidence here: as our maximum momentum transfer is achieved by backscattering of a photon, and hence determined by the photon

energy itself, the momentum transfer at *e.g.* K-edges is limited to a value that still justifies the negligence of the Q-dependence of f' and f'' [28, 29].

If we move to L- or M-edges, we might affect outer electron shells, however, as our x-ray energy decreases, we even further decrease our maximum Q-range. A precise calculation of $f_0(Q)$ remains difficult, as the orbital dimensions have to be calculated for every electron shell and for every element. Tabulated values of $f_0(Q)$, as well as for $f'(E)$ and $f''(E)$ can be found in [25, 26]. For a more precise evaluation of $f_0(Q)$ Baro *et.al.* derived a simple parameterization with a set of 5 parameters (in addition to Z) for every element [27]. All values of $f_0(Q)$ used in this work are based on these parameterization.

2.2.5 Absorption and other inelastic processes in materials

Inelastic scattering has been mentioned in section 2.2.1 as Compton scattering from a free electron. As we look at bound states in our atoms and crystals, there are certainly more inelastic processes to consider. In Compton scattering, the photon is never absorbed, but just transfers a certain energy and momentum to the electron. This causes an arbitrary change in the phase of the photon and therefore it no longer contributes to the coherent scattering. Another form of interaction between photons and electrons is the annihilation of a photon via the photoelectric effect that leads to a complete transfer of the photon energy to the electron system. This system is usually an atom with electrons in bound states. If the x-ray or photon energy is sufficient to overcome the electron binding energy of an atomic shell, electrons can be excited into vacuum levels and the entire photon energy is absorbed. This leaves empty states in the inner shells that are usually occupied by electrons of higher shells, leading to the emission of characteristic x-rays (fluorescence) and Auger electrons. These characteristic x-rays are also parasitic features in our elastic signal in scattering experiments. Beside illumination corrections of the probed sample volume, these contributions are flat in reciprocal space. The energy of the excited fluorescence lines is necessarily below the energy of the incident x-ray photons. It becomes clear that the described process can only take place when the x-ray energy used in the experiment is above an absorption edge of the atom. There exists an analogous process for x-ray energies just below an absorption edge, but above the energy of the fluorescence transitions. This process is called resonant Auger scattering in the case of electron emission, or resonant Raman scattering in the case of photon emission. This scattering can be interpreted on a quantum mechanical basis: the excited electrons can occupy virtual energy levels close to the Fermi level. If the life-time τ of these states is sufficiently short, its energy level can spread out to

the region above the Fermi energy due to the relation $\tau \Delta E \approx \hbar$. It is clear that the probability of this scattering increases very rapidly when approaching the ionization energy. From the ionization energy on, this is then called fluorescence. The main difference between these processes is not only the intensity, but also the much sharper line width of the fluorescence lines due to the life-time broadening in the resonant Raman case. In addition, the resonant Raman emission energy is not independent of the exciting energy. A graph of the electron configuration of Cu is drawn in Fig. 2.7. The K-absorption edge energy is at 8979 eV, indicated as the exciting photon (red arrow). The recombination energy from the L- into the K-shell causes the characteristic K_α radiation at about 8050 eV. The latter is split (due to the Russell-Saunders coupling) into $K_{\alpha 1}$ and $K_{\alpha 2}$. The recombination from the M- into the K-shell is responsible for the K_β emission line which lies at about 8950 eV. The intensity ratio between the K_α and the K_β lines is quantum mechanically determined, and is usually of the order of 5:1. It is important to know that K_α energies are roughly 10 % lower in energy than the ionization level, but K_β energies are within 1 %. In the separation of inelastic from elastic contribution, this can lead to difficulties if the incident photon energy is at the K-absorption edge.
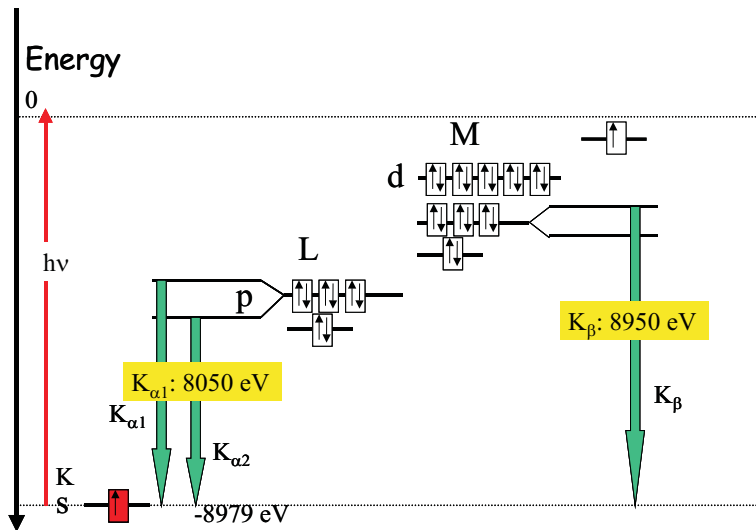

Figure 2.7: Electron configuration and recombination energies of Cu. If the incident photon energy $h\nu$ exceeds the binding energy of 8979 eV of the 1s core level, K-electrons can be excited into vacuum. The recombination from the L- or M-shell causes the K_α and K_β fluorescence emission lines (green arrows).

2.3 Elasticity and strain in crystals

As one of the basic goals of this work is to explore the growth mode of epitaxially grown crystals, it is of importance to have some basic knowledge of the fundamental elastic properties of materials. Additionally, the analysis of the elastic distortions of nanocrystals via x-ray diffraction will be an important tool to analyze their composition.

2.3.1 Tensorial description of stress and strain

In the experimental part of this work, x-ray diffraction is employed as a tool to measure lattice parameters and the orientation of crystal axes. The precise measurement of lattice parameters allows the determination of deformations caused by stresses. This section will be a short introductory review of the mathematical description of the interaction between stress and strain in materials. We will focus in our description on cubic crystals and direct the reader to the excellent introduction given in [30].

A small local deformation can in the general 3D case be written as

$$e_{ij} = \frac{\delta u_i}{\delta x_j} \tag{2.31}$$

where $i, j = 1, 2, 3$ stand for the three space coordinates x_i, and u_i describe the displacement field. It is clear that a local deformation is caused by a local stress. Therefore the deformation is defined as the local derivative of the displacement field. Imagine we look *e.g.* at a rubber rod that extends from 0 to 5 in z-direction, and where we stretch the part between 1 and 2 to about twice its length via an external force. Then the parts formerly between 0 and 1 and between 2 and 5 will move half a unit down- or upwards. So all points in these parts suffer from the same displacement of -0.5 or +0.5, as they are not dilated. Therefore the derivative of the displacement field remains zero in these parts. The material which is therefore in elastic equilibrium suffers according to Eq. (2.31) from no deformation. For reasons of symmetry, we generally use a strain tensor ϵ_{ij} defined as

$$\epsilon_{ij} = \frac{1}{2} \left(e_{ij} + e_{ji} \right) \tag{2.32}$$

which is the symmetric part of e_{ij} that describes the rotation free pure tensile strains in its diagonal components ϵ_{ii}, and the shear strains in the other components. In general the strain tensor ϵ_{ij} is caused by the reaction of the material to an external field, that can be expressed as the stress tensor σ_{ij}. As we are considering small deformations, we can assume Hooke's law to be valid, and we expect some linear relation between the applied stress σ_{ij} and the dilatation or compression expressed by ϵ_{ij}. This linear

relation is given by the elastic properties of the material. As there might be a directional dependence of these properties, they also have tensorial character:

$$\sigma_{ij} = c_{ijkl}\epsilon_{kl} \tag{2.33}$$

c_{ijkl} is a fourth rank tensor that represents the elastic stiffness. As σ_{ij} and ϵ_{kl} are always symmetric tensors which have (in the general case) 6 independent elements. They are therefore often written in the Voigt notation as 6-dimensional vectors. The tensor of the elastic stiffness, c_{ijkl}, can contain a maximum of 36 independent elements. In the Voigt notation, it is written as a 6x6 tensor to link the vectors σ andϵ. In the case of cubic symmetry we can reduce the number of independent variables in c_{ij} down to 3, c_{11}, c_{12}, and c_{44}. For the reductions due to symmetry see [31].

2.3.2 The Poisson coefficients of a cubic crystal

Out of the three independent parameters of the elastic stiffness, we can combine three important and descriptive properties of a cubic crystal.

1. $C = c_{44}$ describes the shear resistance for shearing the (100) plane in the [010] direction.

2. $\bar{C} = \frac{c_{11}-c_{12}}{2}$ describes the shear resistance for shearing the (110) plane in the [1$\bar{1}$0] direction.

3. $K = \frac{c_{11}+3c_{12}}{3}$ describes the resistance against compression under hydrostatic pressure.

For an amorphous (isotropic) material C and $\bar{C}$ are equal, their ratio is called the elastic anisotropy $C/\bar{C}$. As an example for the materials in this work, this anisotropy is around 1.56 for (crystalline) silicon, and in an extreme case 0.26 for PbTe. An example of exploitation of these properties is given in [41], where the self organized growth of quantum dots is induced by extraordinarily high elastic anisotropies.

A further set of descriptive elastic parameters can be introduced via the Poisson numbers ν: they describe the ratio between a longitudinal dilatation (or alternatively a compression) and a transversal contraction (expansion) in an isotropic medium. For the case where C and $\bar{C}$ are known, we can derive two Poisson coefficients, for the longitudinal direction as being the (100)- or the (111) direction one can derive ([32]):

$$\nu_{100} = \frac{3K-2\bar{C}}{6K+2\bar{C}} \tag{2.34}$$

$$\nu_{111} = \frac{3K-2C}{6K+2C} \tag{2.35}$$

For crystals in general, elastic anisotropies influence the reactions to external stresses and deformations. A cubic material with native lattice constant a, which is *e.g.* com-

pressively strained to the lattice parameter $a'_{||}$ in the (100) plane, will react with an expansion in the perpendicular direction to

$$a'_\perp = a \left(1 + \frac{a - a'_{||}}{a'_{||}} \frac{1 + \nu_{100}}{1 - \nu_{100}} \right). \tag{2.36}$$

For strain in the (111) plane, we can write the equivalent formula

$$a'_\perp = a \left(1 + \frac{a - a'_{||}}{a'_{||}} \frac{1 + \nu_{111}}{1 - \nu_{111}} \right). \tag{2.37}$$

These characteristic material parameters can be exploited to distinguish *e.g.* between SiGe alloys with varying composition. When a tetragonal distortion of a cubic lattice is the result of epitaxial stress in a plane and one can measure the reaction of the system as a dilatation perpendicular to this plane, the knowledge of the Poisson ratio allows us to calculate the equilibrium lattice parameter, which is itself linked to the composition of a binary alloy. Strictly spoken this reciprocity in the poisson ratio (note that cause and effect are reversed in it's definition) is only valid in the case of an isotropic medium. As Crystals in general are anisotropic, one has to apply a more sophisticated treatment. Nevertheless the poisson ratio can be used as an approximation in the case of small asymmetries

2.3.3 The influence of stress on the epitaxial growth modes

In epitaxial crystal growth, as *e.g.* molecular beam epitaxy (MBE), used for the samples investigated in this work, crystals with slightly different lattice parameters grow on top of each other. The misfit between their lattice parameters induces what is known as epitaxial stress. Suppose we have an infinitely thick substrate on top of which we evaporate a material of different lattice parameter, this deposit can show three major reactions to the induced stress:

1. The response is elastic strain. The material is forced to have the same in-plane lattice constant as the substrate, and therefore expands or contracts in the perpendicular direction. This growth is called pseudomorphic growth.

2. The response is plastic. Dislocations are formed during the growth and allow the crystal lattice to relax towards its native lattice constant. This is also called plastic relaxation.

3. The stress is so high that the growth no longer forms a smooth surface but changes to an island formation. These three dimensional objects can now laterally expand or contract without the formation of dislocations. This is called elastic relaxation.

The growth modes **1** and **2** are also called Frank-van der Merwe growth [33], mode **3** is called Stranski-Krastanow growth [34].

Which of these growth modes is observed depends of course on the elastic properties of the materials, but also sensitively on the growth temperature, as *e.g.* the formation of dislocations requires a certain energy. Therefore a material can grow pseudomorphic below a certain temperature and change the growth mode to Stranski-Krastanow growth for higher temperatures. It is the competing effects of the system's tendency to reach thermodynamic equilibrium, and the limited mobility of the atoms to achieve it. Typically for most epitaxial structures is a meta stable state: a huge amount of elastic energy is stored and "frozen" in the distorted crystal lattices. A good review of the thermodynamics and kinetics of the various growth modes is given in [34]

2.4 Kinematic diffraction from epitaxial systems

In this section, some examples for typical epitaxial systems are discussed considering the opportunities of their investigation via diffraction methods. The basic question that we seek to answer is: "which x-ray diffraction methods can we employ to measure strain distribution and interdiffusion?"

2.4.1 Non-uniform distorted nano crystals in reciprocal space

If we consider the growth of islands in the Stranski-Krastanow growth mode, we expect the formation of non-dislocated non-uniform distorted islands on top of a perfect crystal. For that reason we expect (even in the case of vanishing interdiffusion between substrate and deposited material) a position at the interface where the in-plane lattice parameters of both materials are equal. We further expect the lattice parameter to relax towards its native constant if we move away from the interface. A common and established technique to measure the strain distribution in such a structure is grazing incidence diffraction (GID) [35, 36]. This experimental method will be introduced later, we want to state here that it allows diffraction only in the plane of the substrate surface. This means we can only gain information about the in-plane lattice parameter. We can in this case at least measure how much material scatters at which lattice parameter, and how far the islands relax towards the top. If we have non-vanishing interdiffusion, however, we can no longer make clear statements about stress in the crystal. As we do not know its composition, we cannot determine the lattice constant for the unstrained state. According to what we have learned in section 2.3 in particular in 2.3.2 about the response of a cubic material to non-hydrostatic pressure, we are able to calculate the native lattice constant of a cubic crystal if we know about his strain state. The conditions are, that we know the in-plane strain and the response of the crystal in the perpendicular z-direction. This reaction is the changed lattice parameter in growth direction, and if the elastic constants are known this will allow us to calculate the equilibrium lattice parameter of the material. In the range of the validity of Vegard's law (the linear interpolation of lattice parameters in alloys), it is then possible to extract the composition [37, 38]. In the case of a growth in [001] direction, the quantity to be measured can also be called tetragonality. If the tetragonality is 0, the material is unstressed (as far as we can exclude hydrostatic compression) and we directly measure its native lattice constant. For growth along the [111] direction, the distortion will be rhombohedral.

Before we proceed, it will be helpful to understand how the lattice spacings, and in

particular the orientation of the netplanes, changes under these distortions. As an example, we consider Ge grown on top of Si. Their lattice parameters differ by 4.2 %. A pseudomorphic distortion of Ge to the Si lattice parameter in the (001) (xy-) plane would cause a well defined expansion in the z-direction. Figure 2.8 shows symbolically interpenetrating unit cells of undistorted, cubic Si and undistorted Ge (a) or pseudomorphic distorted Ge as described before (b). The (004) and (113) net planes are sketched for both materials and both strain states as blue (Ge) or red (Si) planes. In addition, the red axes represent the reciprocal coordinate system of the crystals. The reciprocal lattice points for the (004) and (113) reflections for the two crystal lattices are indicated as red (Si) and blue (Ge) bullets.
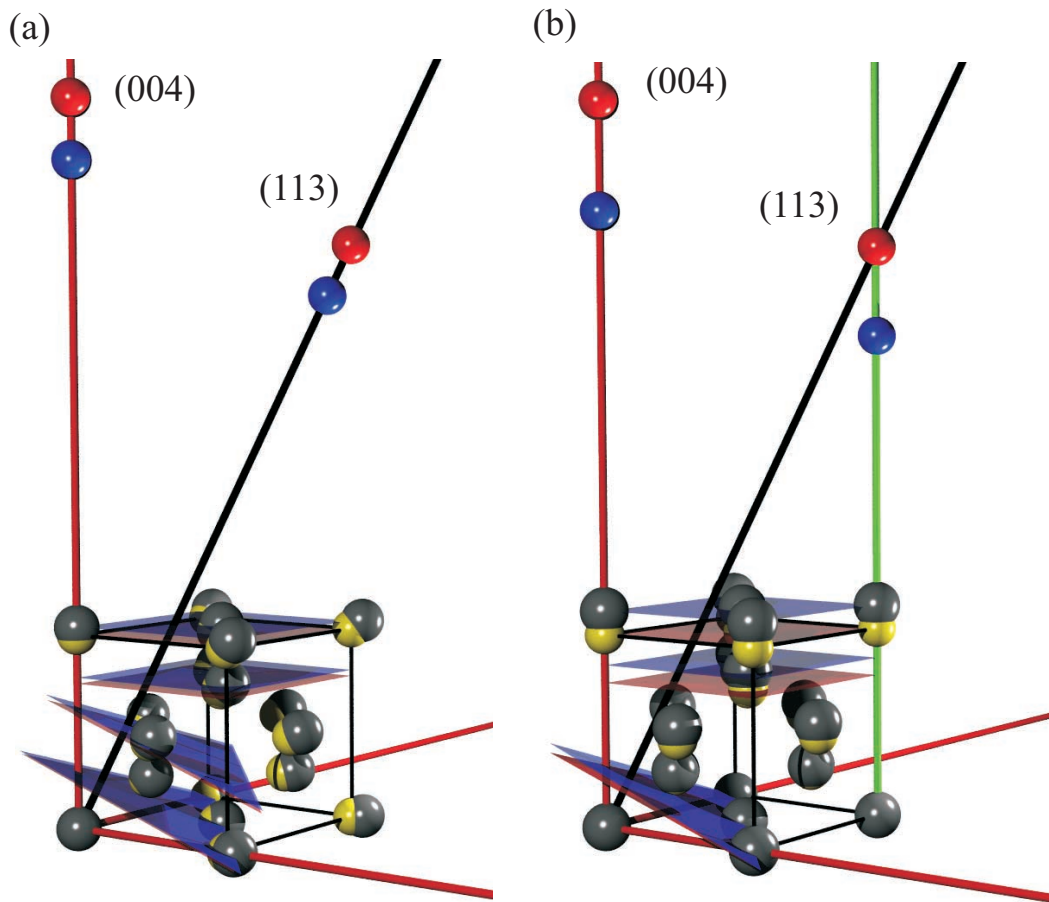
Figure 2.8: Interpenetrating unit cells of Si (yellow bullets) and Ge (grey). The (004) and (113) planes are highlighted for Si (red) and Ge (blue). The reciprocal coordinate system is added as red axes. The reciprocal lattice points for the (004) and the (113) reflection are represented by red (Si) and blue (Ge) bullets. (a) Both lattices are cubic. (b) Ge is tetragonally distorted to the in-plane lattice parameter of Si.

Note that the in-plane compression of Ge leads to an even larger separation of the

symmetric (004) Bragg reflections from Si and Ge. Two successive (004)-planes are drawn as blue planes. In both strain states however, these reflections lie on the same radial line from the origin, in this case the z-axis. The only information we gain here is the out-of-plane lattice parameter. This parameter changes through strain as well as through interdiffusion.

The second indicated reflection is (113). Looking at drawing (b) in Fig. 2.8 we can see that the (113) planes have a different tilt angle for Si and Ge. The Ge (113) reflection deviates of the radial path for cubic structures that is indicated as a black line in (a). It now lies on the green line that marks the pseudomorphic path of Si. All (113) reflections of tetragonally distorted crystals which have the same in-plane lattice parameter as Si are to be found here. So we can note *two* important changes in the (113) reflection of Ge depending on the strain state: the distance to the reciprocal lattice point of Si changes *and* the direction in which we find the reflection pointing from the origin changes. If we know about the elastic constants of Si and Ge, in this case, measuring an *asymmetric* reflection, (*i.e.* a reflection which is neither in-plane nor out-of-plane), can yield information about the composition. If the structure is pseudomorphic, we can determine the composition from the out-of-plane d-spacing: the in-plane distortion originates from the Si-lattice parameter and the out-of-plane expansion as the elastic response from the system, as a function of its equilibrium lattice constant. The latter again depends on the composition. If we find the asymmetric reflections to lie on the cubic path, it is strain free, and we can directly derive the equilibrium lattice constant and therefore the composition.

For every state in between the extremes pseudomorphic and fully relaxed, we can extract an in-plane and an out-of-plane lattice parameter. Their absolute values, together with their ratio (the tetragonality) can again be used to determine strain state and composition. Figure 2.9 shows a magnified region around the (113) reflection. Again the cubic radial path and the pseudomorphic path are indicated by black and green lines. At their intersection point lies the Si (113) reflection. The two extreme cases of pure relaxed Ge and pure pseudomorphic Ge are represented by the full blue spheres. As we get closer to the reciprocal lattice point of Si, the Ge content gets lower (blue transparent spheres). All combinations of compositions and strain are to be found within the relaxation triangle between relaxed Ge, pseudomorphic Ge, and Si.

It should be mentioned however, that this method is only possible if we can exclude hydrostatic compression. In addition, the knowledge about the elastic properties of Si, Ge, and their alloys is necessary. For alloys, the elastic properties are derived via a linear interpolation of the elastic properties of the elements. In the case of 2D layered

systems, hydrostatic pressure can be excluded. For growth of coherent islands on a surface, however, the stress will have a more complicated form. Therefore hydrostatic pressure inside these islands can be caused by inhomogeneous strain fields and by surface tension. For overgrown islands hydrostatic pressure becomes even more important. It can be useful in these cases, to apply numerical simulations of the lattice elasticity via molecular dynamics or finite element methods, as recently done by Albe *et.al.* [39] and Hesse *et.al.* [38]. This needs a calculation of the 2D diffraction pattern which is later compared with the recorded reciprocal space map of the region sketched in Fig. 2.9.
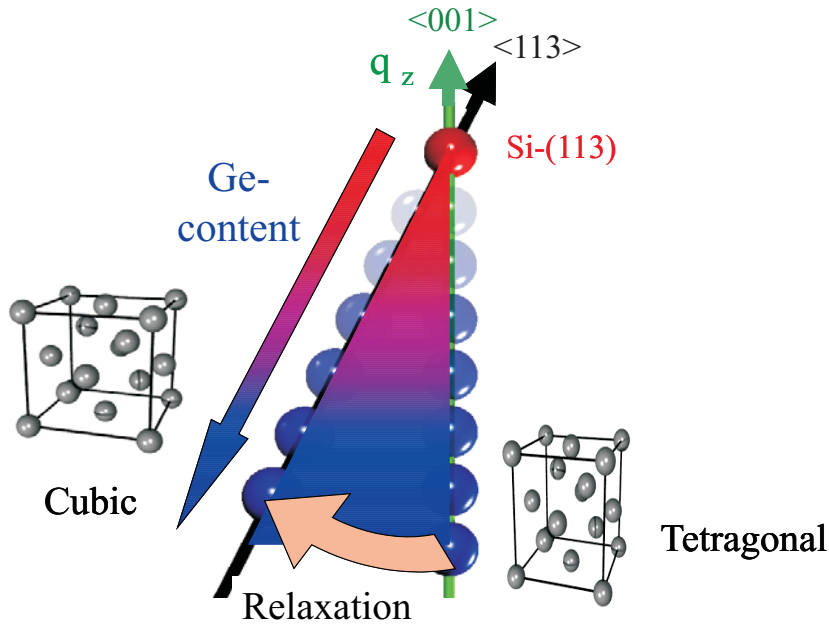

Figure 2.9: Reciprocal lattice points for the (113) reflection of Si (red sphere), relaxed Ge, and pseudomorphic Ge (blue spheres). The transparency of the blue spheres approaching the Si indicate decreasing Ge content.

We keep in mind that for a quick data analysis and a first estimation of our composition, the relaxation triangle method can be used based on the Poisson ratio. We will apply and discuss it in section 3.3.2.

2.5 Effects of resonances on kinematic structure amplitudes

2.5.1 Resonant effects in crystals with more than one element

The possibility of being element sensitive via changing the scattering power of a single atom through the choice of the x-ray wavelength has been discussed. A rather simple theoretical treatment of the anomalous data is usually suitable, when we want to determine concentrations in disordered alloys, as in the SiGe case treated in this work. In those cases, the recorded intensity is proportional to the square of the momentum of the atomic scattering factor. In Bragg reflections from crystals with different elements on well defined sites in the unit cell, other effects might play a dominant role. Parallel net planes can be occupied with different species of atoms leading to superstructure reflections. Prominent examples of two element crystals are the ZnS (zinc blende), the CsCl, and the NaCl (rock salt) structure. The lead and europium chalcogenides treated in the experimental part are representatives of the rock salt structure. The III-V semiconductors GaAs, AlAs, InAs are examples for the zinc blende structure. In the rock salt lattice, the crystal is formed by two fcc lattices that are shifted with respect to each other by $(\frac{1}{2}, 0, 0)a$ with a being the cubic lattice parameter. Figure 2.10 shows a PbSe unit cell. The (111)-planes marked by triangles are alternating occupied with Pb- or Se-atoms.
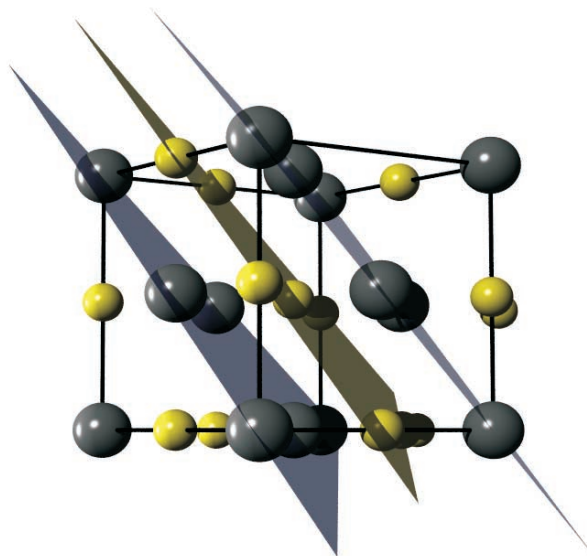

Figure 2.10: Unit cell of PbSe. The (111) planes are successively occupied by Se atoms (small yellow bullets) and Pb atoms (grey bullets).

If we now excite the (111) Bragg reflection from these planes, we obtain a phase shift of π between the waves reflected from the Pb- and the Se-planes. Therefore the waves

scattered by Se and Pb interfere destructively. Bragg reflections that show this behaviour are called *superstructure reflections*. This is of course nothing else than the more descriptive equivalent to what we get when we simply calculate the structure amplitude of such a unit cell. In this case we achieve the following amplitude for Bragg reflections from PbSe with all Miller indices h, k, and l being odd numbers:

$$F_{hkl} = 4\left(f_{Pb} - f_{Se}\right) \tag{2.38}$$

If h, k, and l are all even, we get

$$F_{hkl} = 4\left(f_{Pb} + f_{Se}\right) \tag{2.39}$$

and we expect a strong or also called fundamental reflection. If h, k, and l are mixed, the reflection is forbidden.

In the case of the zinc blende structure, with GaAs as the most prominent semiconductor example, we have again two fcc-lattices this time displaced by $(\frac{1}{4}, \frac{1}{4}, \frac{1}{4})a$. Here we observe superstructure reflections with

$$F_{hkl}^2 = 16\left(f_{Ga} - f_{As}\right)^2 \tag{2.40}$$

for all h, k, and l that satisfy $h + k + l = (2n + 1)2$. This holds for e.g. the (200) reflection. It becomes evident from Eqs. 2.38-2.40 that a change in the atomic scattering factor can have dramatic consequences on the scattered intensity from a superstructure reflection. Here, not the absolute change in the atomic scattering factor is decisive, but the change of a difference between the two elements. In particular this allows in theory an annihilation of a superstructure Bragg reflection in the case where the scattering factors for the two elements are equal. One has to bear in mind however, that the atomic scattering factor is a complex number, therefore "equality" means that imaginary *and* real part of both numbers have to be equal. In other words, their momenta and their phases have to coincide. This is, however, *never* the case. Nevertheless for equal momenta the difference in phase can be small and therefore a pronounced minimum in the scattering amplitude from a Bragg reflection is possible. In the following, we will see two examples for a typical and an extreme case of the suppression of superstructure reflections.

As a first example, let's consider GaAs, a common semiconductor that crystallizes in the zinc blende structure. With only element number 32 (Ge) in between, Ga (31 electrons) and As (33 electrons) are almost neighbours in the periodic table. Their scattering factors do generally not differ very much, making the superstructure (200) reflection very weak compared to the (400) fundamental reflection. In the vicinity of the

K-absorption edge of As, one observes two intersection points for the modules $\mid f_{Ga} \mid$ and $\mid f_{As} \mid$ as shown in Fig. 2.11 (a) together with their anomalous phases in (b). The Q-correction for f_0 is taken into account for the GaAs (200) momentum transfer.
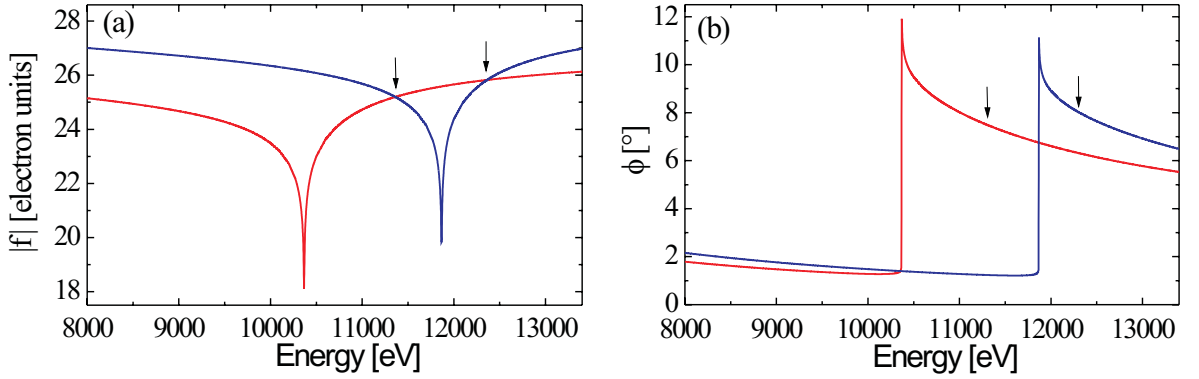

Figure 2.11: (a): Modules of the atomic scattering factors $\mid f_{Ga} \mid$ (red line) and $\mid f_{As} \mid$ (blue). (b): Anomalous phases ϕ_{Ga} (red) and ϕ_{As} (blue). In both graphs, the intersection points of $\mid f_{Ga} \mid$ (red line) and $\mid f_{As} \mid$ are marked with arrows.

At the first intersection point, we are just below the resonant energy of As, and just above the resonance of Ga. This leads to a strong difference between their phases $\phi_{Ga,As}$. The second intersection point lies just above the resonance of As and slightly further above the resonance of Ga. Both atoms have non-negligible phases in these points and their difference is significantly smaller than at the first intersection point. The global minimum of the (200) structure amplitude therefore is to be found here. Figure 2.12 (a) shows polar plots of the modules $f_{Ga,As}$ in the complex plane. The phases $\phi_{Ga,As}$ are scaled in degrees. Small arrows mark the beginning of the curves at 2000 eV. With increasing x-ray energy one moves along the curves up to 17000 eV. The long arrows indicate examples of points for the distinct energies 8100 eV (black arrows), 11373 eV (green), and 12352 eV (magenta). The latter two correspond to the two intersection points of $\mid f_{Ga} \mid$ and $\mid f_{As} \mid$ as mentioned before. In (b), the expected kinematic x-ray (200) Bragg intensity is plotted as a function of energy. The energies marked in (a) are indicated by arrows in the same colours. The intersection points from Fig. 2.11 (a) correspond to the local and the global minimum for the intensity. An example for an experimental exploitation of these pronounced minima can be found in [42].
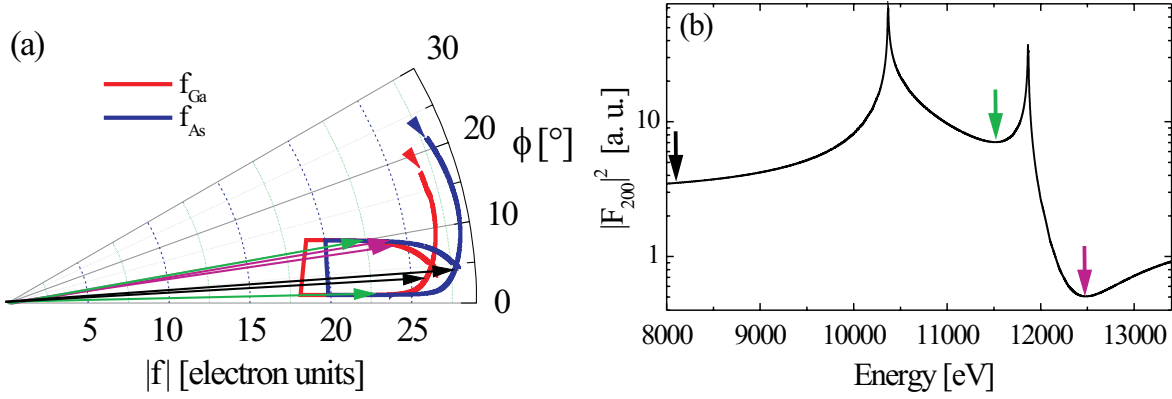
Figure 2.12: (a): Polar plots of f_{Ga} (red line) and f_{As} (blue line) in the complex plane. The x-ray energy serves as the curve parameter. Coloured arrows represent the scattering factors for the energies 8100 eV (black), 11373 eV (green), and 12352 eV (magenta). (b): Expected x-ray intensity for the GaAs (200) reflection. The same energies as in (a) are marked by arrows.

In the second example we have a look at the more extreme case of the PbSe (111) reflection. From Eq. (2.38) we know that in this rock salt lattice, the (111) Bragg reflection is a superstructure reflection. Differing from the case discussed before, these two elements are far away from each other in the periodic table. Lead has 82 electrons, and Se 34 electrons. Therefore one does not observe a dramatic difference in the strength of the superstructure or fundamental reflections from these crystals (as can be calculated from Eqs. (2.38+2.39) their kinematic intensity ratio is 6). In addition, it is evident that it will be a lot more difficult to equalize the scattering contribution from Pb and Se via resonant effects in order to suppress the superstructure reflections. Nevertheless we have more resonant energies available from lead, than we had from Ga or As before. The "availability" is of course limited by our flexibility in the choice of the x-ray energy. Even under the best experimental conditions there are limitations due to the required wavelength regime for diffraction. To excite a Bragg reflection, we need a wavelength which is at least smaller then twice the distance of the net planes. This defines a lower limit for the x-ray energy exploitable for diffraction. For our system of PbSe, the lowest indexed reflection is the (111) reflection and its net plane distance amounts to 3.54 Å. The longest wavelength that can excite this reflection therefore is $2 * 3.54$ Å$= 7.08$ Å, corresponding to an x-ray energy of 1750 keV. As backscattering usually takes considerable experimental effort and does not allow us to probe a reasonable Q-range around the Bragg reflection it is always necessary to use a higher energy than this limit. Nevertheless we can state, that we could excite the PbSe (111) reflection down to x-ray energies of about 2000 eV. In the energy range $2000 eV - \infty$

we can take advantage of the K-, L-, and M-edge of Pb. The K-edge at 88 KeV will not be considered here, as the energy is above the limit of the energy regime that is generally employed for HXRD. Additionally its resonance effects will be fairly weak compared to those at the L- and M-edges. The momenta of the scattering factors of Pb and Se are plotted as a function of energy in Fig. 2.13(a) together with their phases in (b). The plotted energy range covers the regime of the Pb M-edges around 2500 eV and the regime of the Pb L-edges starting around 13000 eV. The values of $| f_{Pb} |$ and $| f_{Se} |$ are corrected for the PbSe (111) momentum transfer.
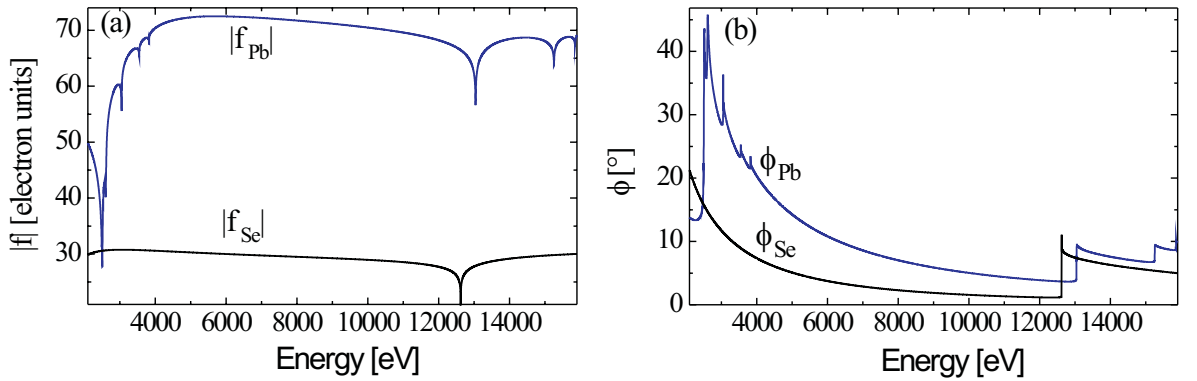

Figure 2.13: (a): Modules of the atomic scattering factors $| f_{Pb} |$ (blue line) and $| f_{Se} |$ (black). (b): Anomalous phases ϕ_{Pb} (blue) and ϕ_{Se} (black).

The strong resonance at the Pb M_V-edge allows for an intersection between $| f_{Pb} |$ and $| f_{Se} |$. Over the whole range of the remaining energy spectrum, the scattering factor of lead is much stronger than that of selenium. We therefore have a closer look at the region in the vicinity of the Pb M_V-edge in Fig. 2.14 (b) and (c). In Fig. 2.14 (a), f_{Pb} and f_{Se} are plotted in the complex plane in the energy regime 2000-16000 eV. Note the qualitative difference compared to Fig. 2.12 (a), where both atoms showed a similar evolution. The green arrows represent the position at an energy of 2490 eV, where the minimum for the PbSe (111) structure amplitude is expected. The red arrows represent 8000 eV as an example for rather typical x-ray energies. In (b), $| f_{Pb} |$ and $| f_{Se} |$ are plotted as a function of energy as in Fig. 2.13 (a), but for the energy range 2100-2900 eV. Fig. 2.14 (c) shows the expected kinematic PbSe (111) intensity for the discussed energies. The expected global minimum is located 10 eV below the first intersection point of $| f_{Pb} |$ and $| f_{Se} |$ at about 2490 eV. This position is marked by the green arrows.
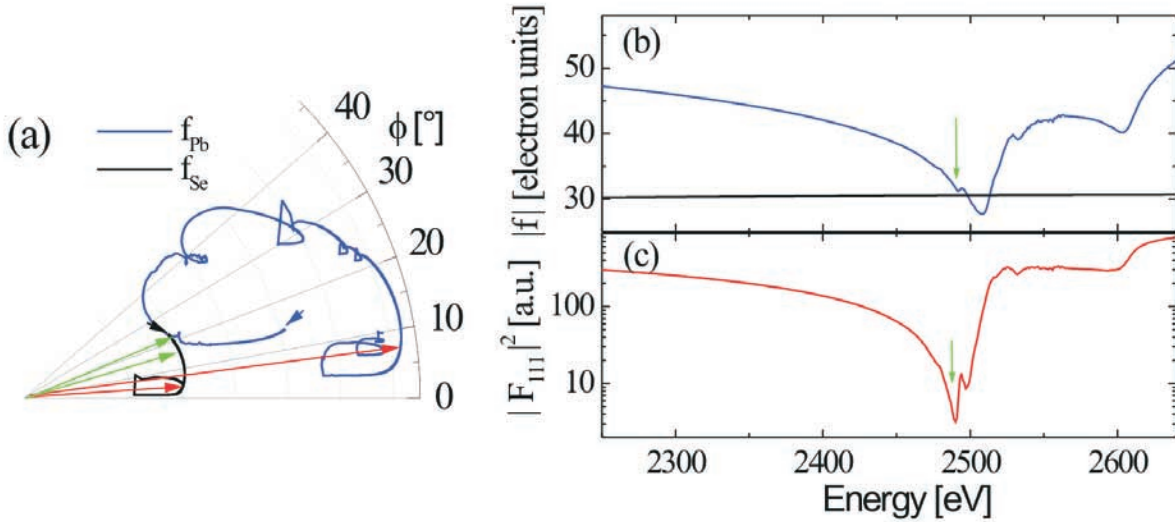
Figure 2.14: (a): Polar plots of f_{Pb} (blue line) and f_{Se} (black line) in the complex plane. Coloured arrows represent the scattering factors for the energies 2490 eV (green) and 8000 eV (red). (b): Modules of the atomic scattering factors $\mid f_{Pb} \mid$ (blue line) and $\mid f_{Se} \mid$ (black). (c): Expected intensity for the PbSe (111) Bragg reflection. The green arrow marks the global minimum.

Due to its experimental importance, we will have a more detailed look at the exact location of these minima in the experimental part 3.4.4

2.5.2 The linear chain as a thin film model

One of the major benefits of the kinematic treatment of diffraction is the fact that it often opens up the opportunity to find analytical solutions. In the case of 2 dimensional epitaxial samples we often deal with highly perfect systems that are still kinematic scatterers due to their finite size. In this work, multilayers of thin films of IV-VI semiconductors as PbSe, PbTe, or EuSe will be studied. These are grown in the (111) direction, in which we observe an alternating stacking of the two compound species as shown earlier in Fig. 2.10. If we are interested in the Fourier transform of these thin films perpendicular to the film plane, *e.g.* because we want to find out about the pseudomorphic distortion or interface roughness, we only have to consider a 1 dimensional model of this structure. As sketched in Fig. 2.15, we can project such a 2D film over all x-y-directions onto its z-axis perpendicular to the film-plane. The reciprocal space description on this axis can therefore be limited to the Fourier transform of a linear stack of atoms.
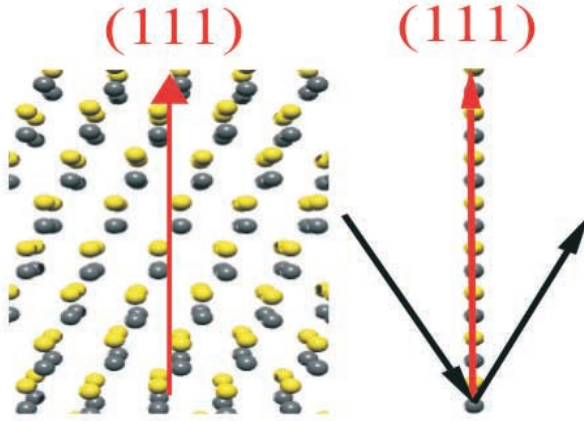
Figure 2.15: Replacement of a thin film by a linear chain. If only the scattering perpendicular to the film plane is considered, as *e.g.* the (111) direction in this case, the Fourier transform of the perfect film is equivalent to that of a stack of atoms.

We may start the description with an even more simple structure than the one in Fig. 2.15: a perfect film of an elemental crystal. This can be simplified by a linear chain of N_a atoms at distances a with an atomic scattering power f_{a_1} and an anomalous phase ϕ_{a_1} defining the atomic formfactor to be $f_{a_1} e^{i\phi_{a_1}}$ as introduced in Eq. (2.30). The linear charge density distribution $\varrho(z)$ of such a chain is represented by a convolution of a sum of N_a delta functions with the charge distribution $\rho_{a_1}(Z)$ of a single atom:

$$\varrho(z) = \left[\sum_{n=0}^{N_a-1} \delta(na - z) \right] \otimes \rho_{a_1}(Z) \tag{2.41}$$

To evaluate the Fourier transform as the scattering amplitude of 2.41, we apply the convolution theorem 2.14 and are able to replace it by the product of the Fourier transforms of the convoluted objects. For $\rho_{a_1}(Z)$ this results in the atomic scattering factor $f_{a_1} e^{i\phi_{a_1}}$. For the sum in 2.41 we can evaluate a sum of integrals due to the linearity given in Eq. (2.9). Each of these integrated delta functions leads to a simple exponential term from the Fourier integral 2.8. The scattering amplitude of the linear charge distribution 2.41 is therefore

$$A(Q) = f_{a_1} e^{i\phi_{a_1}} \sum_{n=0}^{N_a-1} e^{iQna} = f_{a_1} e^{i\phi_{a_1}} \frac{e^{iQN_a a} - 1}{e^{iQa} - 1} \tag{2.42}$$

The last step in 2.42 uses the solution for the geometrical series

$$\sum_{n=0}^{N-1} x^n = \frac{x^N - 1}{x - 1} \tag{2.43}$$

The scattered intensity $I(Q)$ is described by the absolute square of the Fourier transform. Together with the relation $e^{iQz} = \cos Qz + i\sin Qz$ it results in

$$I(Q) = AA^* = |f_{a_1} e^{i\phi_{a_1}} \frac{e^{iQN_a a} - 1}{e^{iQa} - 1}|^2 = f_{a_1}^2 \frac{\cos QN_a a - 1}{\cos Qa - 1} = f_{a_1}^2 \frac{\sin^2 \frac{1}{2} QN_a a}{\sin^2 \frac{1}{2} Qa}. \tag{2.44}$$

This solution is generally known from textbooks as *e.g.* [43] as the solution for a well-defined truncated crystal. It will be derived in more detail in the appendix (A.1). Around the Bragg maxima at positions $n\frac{2\pi}{a}$ it shows Laue oscillations caused by the truncation of the system. We note that in 2.44 the atomic phase factor $e^{i\phi_{a_1}}$ plays no role in the scattering but only the modulus f_{a_1} determines the intensity. Figure 2.16 gives an example for N_a=12 and a=3.3 Å. The Q_z range across the first Bragg reflection is plotted. The higher order Bragg reflections are shown in the inset. Note that in this analytical treatment the momentum dependence of the atomic scattering factor is ignored. The distance of the Laue-oscillations corresponds to the reciprocal thickness of the film, the number of oscillations between two Bragg points contains the information about the number of atoms across the film: for N atoms one counts N-2 oscillations. (equivalent to the N-2 side maxima of the grating diffraction function in classical optics [15]).
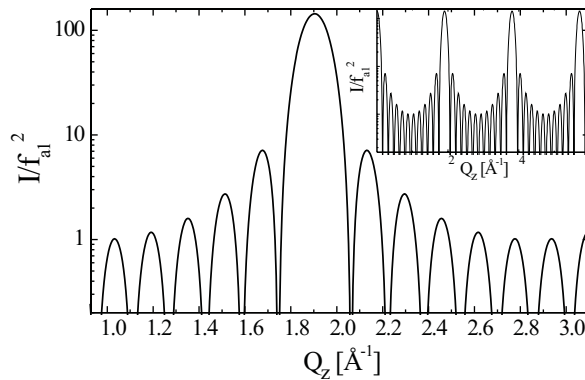

Figure 2.16: First order Bragg reflection from a thin film. The diffraction in Q_z-direction was calculated according to Eq. (2.44) for N_a=12 and a=3.3 Å. The inset show the higher order Bragg reflections.

It is no surprise here that the intensity of the Bragg reflections is proportional to N_a^2 and to $f_{a_1}^2$, and is the same for all Bragg reflections (when ignoring the momentum effect on f_{a_1}). In the case where our crystal is a compound material and has *e.g.* 2 atoms in the unit cell, we might have a look at the linear chain with two different species. This situation has already been illustrated in Fig. 2.15. It can be described by two linear chains of lattice spacing a as before but displaced with respect to each other by $\frac{a}{2}$. These two linear chains may be occupied by the scatterers represented by $f_{a_1}e^{i\phi_{a_1}}$ and $f_{a_2}e^{i\phi_{a_2}}$. Then we can apply a similar treatment as in eqs. (2.41)-(2.44). The evaluation of the square of the complex amplitude also yields cross-terms as we have to square a sum. The derivation of the analytical solution can be found in the

appendix (A.2). In total we can write for this intensity distribution:

$$I\left(Q\right) = AA^* = |f_{a_1}e^{i\phi_{a_1}}\frac{e^{iQN_a a}-1}{e^{iQa}-1} + e^{iQ\frac{a}{2}}f_{a_2}e^{i\phi_{a_2}}\frac{e^{iQN_a a}-1}{e^{iQa}-1}|^2$$

$$= \left[f_{a_1}^2 + f_{a_1}^2\right]\frac{\sin^2\frac{1}{2}QN_a a}{\sin^2\frac{1}{2}Qa} + 2f_{a_1}f_{a_2}\cos\left(\phi_{a_1} - \phi_{a_2} - \frac{Qa}{2}\right)\frac{\sin^2\frac{1}{2}QN_a a}{\sin^2\frac{1}{2}Qa} \qquad (2.45)$$

The first term in Eq. (2.45) represents the phase-independent solutions for the two interpenetrating monoatomic lattices, the second term containing the cosine describes their interference. Considering the first order Bragg reflection at $Qa = 2\pi$ will help to understand the importance of this term: if we are far from edges and if we can neglect the phases, the cosine will then turn out to be -1. Therefore the "intensity" represented by the interference term has to be subtracted from the phase-independent part. In the extreme case of $f_{a_1} = f_{a_2}$ the intensity of both terms is equal and the first order Bragg reflection is annihilated. This is the case as discussed before in section 2.5.1. The fact that we have destructive interference between the two species of atoms at this reflection makes it a so called superstructure reflection.

It can be observed for films of *e.g.* GaAs grown in (001) direction or PbSe grown in (111) direction. The separated results for Eq. (2.45) are plotted in Fig. 2.17 (a) and (b) in the vicinity of the first two Bragg points.

As an example, atoms with negligible or equal phase where chosen. In 2.17(a), the two independent solutions for the two interpenetrating linear chains are plotted for the scattering power f_{a_1}=34 (red atoms+line) and f_{a_2}=29 (blue atoms+line) and for N_a=12. The black line is their interference part. In (b), the diffracted intensity from (2.45) as the sum of these contributions is plotted on a logarithmic scale. The interference part plotted as the black line in (a), finally determines the dramatic difference in the intensity between the first order (superstructure peak) and the second order (fundamental peak) Bragg reflection.

As already explained, this example does not show the effect of the atomic phases, as they were neglected here. This is justified when we are far away from edges, or because their phases are equal. In both cases, they would cancel out in Eq. (2.45). Therefore the interference contribution (black line in Fig. 2.17(a)) has a pronounced minimum exactly at the superstructure Bragg position and a strong maximum at the fundamental Bragg position. At these positions, the argument in the cosine of the interference part is a multiple of π. The position of the interference minimum at the superstructure reflection is therefore defined by the *spatial* interference between the two linear chains of atoms. In reciprocal space, it is exactly located at the Bragg points of the

non interfering contributions from the two separate chains. If we now take a significant phase contribution into account, this coincidence between the minima and maxima of the interfering and non-interfering parts of the structure will change.
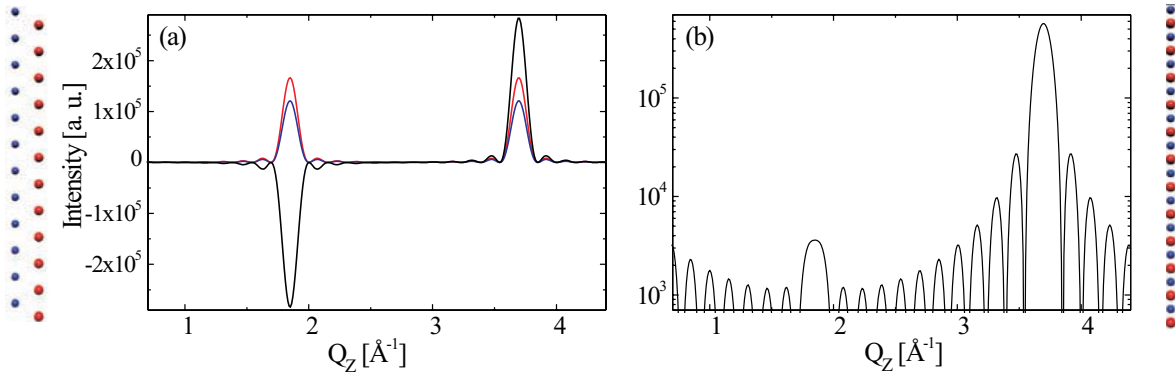

Figure 2.17: (a): Separate plots for the contributions to the diffracted intensity from a perfect thin film of a biatomic compound (here PbSe at an x-ray energy close to the Pb M_V-edge. The intensity as expected from the single linear chains from the two species of atoms is plotted as a red line for the stronger scatterer and as a blue line for the weaker scatterer. The interference part is plotted in black. (b): Sum of the three contributions in (a).

In the following we want to focus on the first order Bragg reflection. Due to the destructive interference at this point, we will be particularly sensitive to changes in the interference term of Eq. (2.45). We may simply consider a similar example as before, with N_a=12 atoms represented by f_{a_1}=34 and f_{a_2}=29. We take into account anomalous phases of ϕ_{a_1}=0.7 and ϕ_{a_2}=0.26 (in radians). These are reasonable values for $e.g.$ PbSe in the vicinity of the Pb M_V-edge, as seen in Fig. 2.13. As the argument in the minima and maxima of the cosine in the interference part of Eq. (2.45) are now shifted, the destructive interference no longer lies on the first order Bragg point, but is slightly displaced to higher values. This should cause a depression in the intensity on the right side of the Bragg peak. In the vicinity of the fundamental reflection, the maximum of the positive interference also lies slightly above the Bragg position. As all three terms of Eq. (2.45) add here, the effect is less important than on the superstructure reflection. The calculated intensity profiles for this example are plotted in Fig. 2.18 for the superstructure reflection in (a) and for the fundamental reflection in (b).

The effect of the anomalous phases causes the strong asymmetry of the superstructure reflection, which was not observed in Fig. 2.17 (b). Note that an exchange of the anomalous phases or even the atoms in Eq. (2.45)would cause a reversed asymmetry

of the Bragg peaks in Fig. 2.18, as it would change the sign in front of the larger phase ϕ_{a_1} in the argument of the cosine. This is a very interesting observation: Consider *e.g.* a rock salt (as in the case of PbSe) or a zinc blende (as for GaAs) structure. Both lattices contain two elements which each occupy complete fcc-lattices, the two lattices are just displaced with respect to each other. An exchange of these two lattices now leads to a change in the asymmetry of the Bragg reflections from a thin film. The reason is the following: the structure described here is *not* centro-symmetric. As we have the same number of atoms of both species in our film, the stacking starts *e.g.* with atom a_1 and ends with atom a_2. Therefore an exchange of the atoms would have the same effect as diffracting from the top or the bottom of the film, probing either the (111) or the ($\bar{1}\bar{1}\bar{1}$) reflection, leading to the known effect for Friedel pairs [18]. Asymmetries due to phase effects have been exploited to study interfaces and stacking order at the substrate film interfaces [44]. It is evident that the effects discussed above opens up the possibility to be sensitive to the absolute stacking order of a *free* superstructure film independent from the underlying substrate *i.e.* to determine the last atomic layer at the free interface between film and air or vacuum.
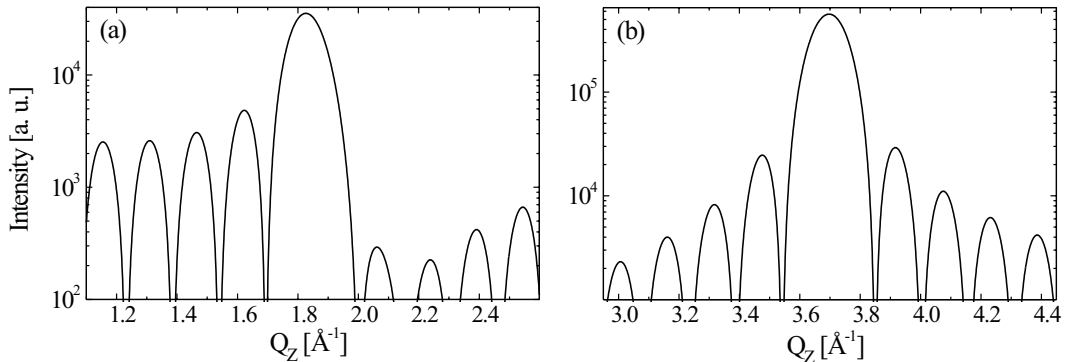

Figure 2.18: Effect of the anomalous phase at an x-ray energiy close to the Pb M_V-edge on the reflections from a thin PbSe film. (a): (111) superstructure reflection for the same example as in Fig. 2.17 (b) with anomalous phases taken into account. (b): (222) fundamental reflection for the same structure. The phase effect is less dominant here.

2.5.3 Influence of the atomic scattering factors on the reciprocal position of superstructure reflections

The effects of the anomalous phase on the interference part in Eq. (2.45) as discussed before, do not only affect the asymmetry of the Bragg reflections. The fact that the minimum position of the cosine term is shifted by the atomic phases f_{a_1} and f_{a_2} can

also influence the centre position of the Bragg reflection. Again, the superstructure reflections are more significantly affected than the fundamental ones. In the investigation of epitaxial systems, superstructure reflections often offer the opportunity of a better discrimination between materials. Therefore it is important to have a closer look at the positional dependence on the atomic scattering factors. Still employing Eq. (2.45) we might take a very common system as an example: a thin GaAs film. We consider the possibility of strain determination in the GaAs film via the reciprocal position of its (002) reflection. We assume a film thickness of about 68 Å corresponding to $N_a = 24$ for a GaAs lattice constant of 5.654 Å. (Note that each unit cell in the zinc-blende structure contains 2 laterally displaced bilayers of GaAs). Having a look back at Fig. 2.11, it seems reasonable to start with 4 points in the energy range generally used for crystallography: below both K-edges at around 8000 eV, between the Ga and As K-edges at 10368 eV and 11867 eV, right above the As K-edge, and finally somewhere above both edges. These situations are simulated in Fig. 2.19 (a)-(d) as black lines together with Gauss-fits (red lines) as a typical experimental method to determine the peak position.
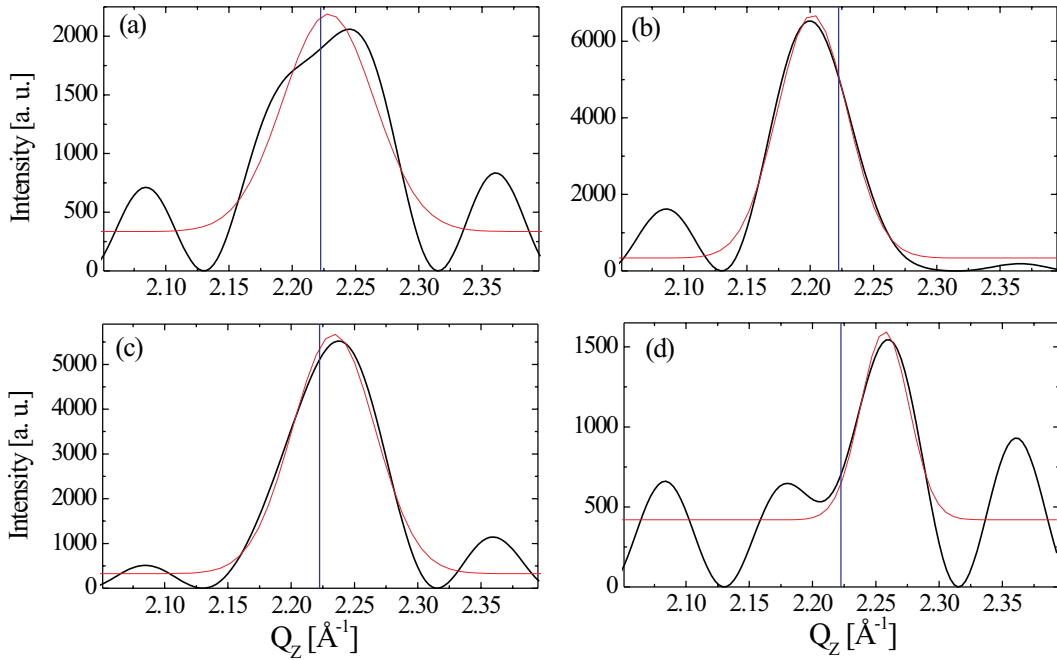

Figure 2.19: Energy dependent variation of the GaAs (002) position. Plot of the diffracted intensity from a 68 Å (001) oriented GaAs film according to Eq. (2.45). The superstructure reflection is shifted with respect to the reciprocal (002) position indicated as a perpendicular blue line at 2.223 Å^{-1}. The energies chosen for the simulations are: 8000 eV (a), 11000 eV (b), 11900 eV (c), and 14000 eV (d).

The position of the reciprocal (002) lattice spacing is added as a perpendicular blue line at 2.223 Å^{-1}. Note that the changes in the interference term do not only affect the peak position, but also lead to a change in the peak width. The positional shift of such a film also depends on its thickness. As the interference part in Eq. (2.45 is a product of the cosine term containing the energy dependent atomic phases ϕ_{a_1} and ϕ_{a_2} and the oscillating term that determines the reciprocal position and width of the peak according to the lattice constant a and the thickness $N_a a$ of the film. For small thicknesses $N_a a$, it leads to a broad Bragg peak. If the envelope changes its center and shape significantly, it will as well shift the maximum of the resulting curve. With increasing thickness, the oscillating term gets sharper, and therefore its position can be less influenced by a deformation of its envelope function. The evolution of the (002) peak position through the energy regime from 8000 to 14000 eV is plotted for a 68 Å thick GaAs film in Fig. 2.20 (a). For a fixed energy of 12200 eV, the dependence of the peakshift on the film thickness is shown in (b).
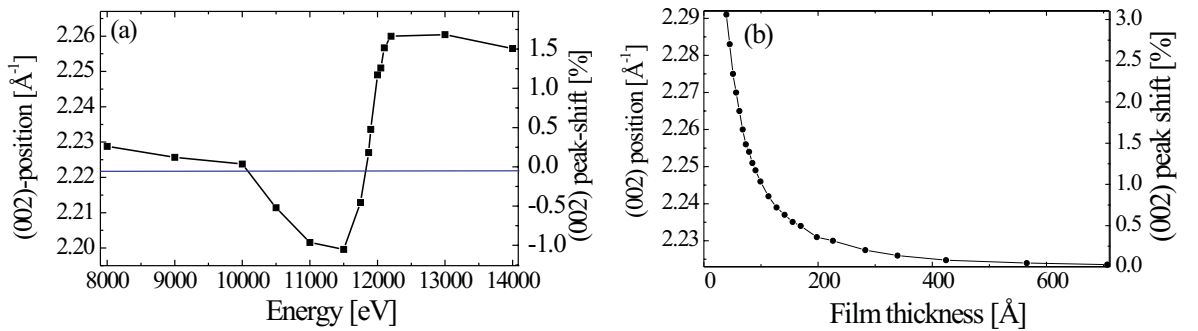

Figure 2.20: Dependence of the GaAs (002) peak position on energy and film thickness. (a): Energy dependence of the peak position of the GaAs (002) reflection from a 68 Å thick film. (b): Peak shift at 12200 eV as a function of the film thickness.

In the characterization of epitaxial structures, superstructure reflections often give the opportunity for a better material discrimination. Therefore it is important to know about this positional shift. As it is an effect that appears even in the theoretical treatment of a "free" thin film, it is caused by the scattering process itself and should not be confused with *e.g.* a disturbance effect from the underlying substrate as has been reported upon be Fewster *et al.* [45].

2.5.4 Analytical treatment of an epitaxial bilayer

The results derived for the diffraction of a thin film in chapter 2.5.2 are now to be extended to an epitaxial system: Two films with slightly different lattice parameter grown on top of each other. This model will then serve to simulate multilayered systems. Due to the convolution theorem of Fourier transforms given in Eq. (2.14) we can state, that in reciprocal space, a multilayer of two materials is described by the product of the Fourier transform of a bilayer and the Fourier transform of the grating with the bilayer thickness as the grating constant. Thus we can understand all fundamental structural properties as strain or interface quality via the envelope function corresponding to the perfect bilayer. The fact that this system is then periodically repeated does certainly not change the properties of a single bilayer. In reciprocal space, this additional periodicity leads to oscillations which modulate the envelope function of the bilayer. As the main interest in this work is focussed on strain, we might think about how well we can separate the contributions of both layers in reciprocal space, and what advantage we can take from the influence of resonant behaviour. To get started we will again treat the perfect 2 dimensional system as a linear chain of stacked atoms. The only difference to the treatment of a thin film grown in a superstructure direction in chapter 2.5.2 is now that we have two successive linear chains with lattice constants a and b, and species of atoms represented by the scattering factors $f_{a_1}e^{i\phi_{a_1}}$, $f_{a_2}e^{i\phi_{a_2}}$, $f_{b_1}e^{i\phi_{b_1}}$, and $f_{b_2}e^{i\phi_{b_2}}$, if we still limit ourselves to systems of two compounds. Their thicknesses are again described by the number of atomic layers N_a and N_b. If we suppose the fact, that we have a pseudomorphic growth and that both materials have the same crystal structure, their out-of-plane lattice parameter will differ only slightly. Therefore the interference terms we expect to get in an analytical solution will be of special interest. In an equivalent way as in chapter 2.5.2, we can simply start with our linear sum over the atoms. Again every single film ist described by two linear chains, displaced by half its lattice parameter. One of the two films is additionally displaced by the thickness of the other one. Using again the compression of the finite sums to geometrical series, we can write for the intensity:

$$I(Q) = AA^* = \left| f_{a_1}e^{i\phi_{a_1}}\frac{e^{iQN_a a}-1}{e^{iQa}-1} + e^{iQ\frac{a}{2}}f_{a_2}e^{i\phi_{a_2}}\frac{e^{iQN_a a}-1}{e^{iQa}-1} \right.$$
$$\left. + e^{iQN_a a}f_{b_1}e^{i\phi_{b_1}}\frac{e^{iQN_b b}-1}{e^{iQb}-1} + e^{iQ\frac{b}{2}}e^{iQN_a a}f_{b_2}e^{i\phi_{b_2}}\frac{e^{iQN_b b}-1}{e^{iQb}-1} \right|^2. \quad (2.46)$$

The evaluation of this intensity will lead to the same terms as in Eq. (2.45) *i.e.* fundamental- and interference terms for both single films. In addition however, we expect four more interference terms for the superposition of the amplitudes from the atomic chain pairs (a_1, b_1), (a_1, b_2), (a_2, b_1), and (a_2, b_2). With a proper treatment of

Eq. (2.46) we can separate all these terms in an analytical solution. The intensity distribution on the specular path of such a bilayer then reads:

$$I(Q) = AA^* =$$

$$2\left[f_{a_1}^2 + f_{a_2}^2 + 2f_{a_1}f_{a_2}\cos\left(\phi_{a_1} - \phi_{a_2} - \frac{1}{2}aQ\right)\right]\left(\frac{\sin\left(\frac{1}{2}aN_aQ\right)}{\sin\left(\frac{1}{2}aQ\right)}\right)^2$$

$$+ \quad 2\left[f_{b_1}^2 + f_{b_2}^2 + 2f_{b_1}f_{b_2}\cos\left(\phi_{b_1} - \phi_{b_2} - \frac{1}{2}bQ\right)\right]\left(\frac{\sin\left(\frac{1}{2}bN_bQ\right)}{\sin\left(\frac{1}{2}bQ\right)}\right)^2$$

$$+ \quad 2\left[f_{a_1}f_{b_1}\cos\left(\phi_{a_1} - \phi_{b_1} - aQ - \frac{1}{2}aN_aQ - \frac{1}{2}bN_bQ\right)\right.$$

$$+ \quad f_{a_1}f_{b_2}\cos\left(\phi_{a_1} - \phi_{b_2} - aQ - \frac{1}{2}aN_aQ - \frac{1}{2}bN_bQ - \frac{1}{2}bQ\right)$$

$$+ \quad f_{a_2}f_{b_1}\cos\left(\phi_{a_2} - \phi_{b_1} - \frac{1}{2}aQ - \frac{1}{2}aN_aQ - \frac{1}{2}bN_bQ\right)$$

$$+ \quad \left. f_{a_2}f_{b_2}\cos\left(\phi_{a_2} - \phi_{b_2} - \frac{1}{2}aQ - \frac{1}{2}aN_aQ - \frac{1}{2}bN_bQ - \frac{1}{2}bQ\right)\right]$$

$$* \quad \frac{\sin\left(\frac{1}{2}an_aQ\right)\sin\left(\frac{1}{2}bN_bQ\right)}{\sin\left(\frac{1}{2}aQ\right)\sin\left(\frac{1}{2}bQ\right)}$$

$$(2.47)$$

The derivation of this equation is presented in the appendix part A.3. The first two lines Eq. (2.47) are the separate solutions for the two single films, the following lines describe the pair interferences mentioned above. Resonant effects on the single film have been discussed in the previous chapter. Before studying them in the bilayer system, we will focus purely on the interferences due to the spatial periodic arrangement of the atoms in such a bilayer. Therefore we first assume, that all atomic phases are negligible. As we have maxima in intensity at the Bragg points, *i.e.* when either $bQ = 2\pi$ or $aQ = 2\pi$, we can then state, that the cosine terms of the interferences have maxima or minima deviating from these points, as soon as a and b are different. As all these cosine terms are multiplied with $\frac{\sin\left(\frac{1}{2}an_aQ\right)\sin\left(\frac{1}{2}bN_bQ\right)}{\sin\left(\frac{1}{2}aQ\right)\sin\left(\frac{1}{2}bQ\right)}$ however, it becomes clear that if a and b are too different, the influence of the interference on the Bragg peak shape and position vanishes very quickly. As the mentioned term is a product of functions that have pronounced maxima at the Bragg peaks, a larger difference between a and b would leave this term to be very small almost all over reciprocal space.

In real epitaxial systems we might usually face the fact, that a and b differ by a few percent, making it worth to discuss the influence of the interferences in Eq. (2.47). In a diffraction experiment from such an epitaxial structure, one might expect to have two peaks at each Bragg point, expressing the lattice parameters in the two materials. As an example we have a look at a bilayer of EuSe/PbSe grown along [111]-direction.

The structure shall be pseudomorphically grown with an in-plane parameter of PbSe. In growth direction this leads to an undistorted growth of PbSe with its equilibrium lattice parameter of a_{PbSe}=6.122 Å. The EuSe is tetragonally distorted in the growth direction to a_{EuSe}=6.3 Å. For this case and for thicknesses $N_{PbSe} = 25$ and $N_{EuSe} = 35$, simulations are performed as shown in Fig. 2.21. The first order Bragg reflection perpendicular to the film plane (as these are the ones described by Eq. (2.47)) is the (111) reflection. For this Bragg reflection, the scattered intensities from the single films described by Eq. (2.45) are plotted as a red line for EuSe and as a blue line for PbSe in Fig. 2.21 (a). They represent the first two lines in Eq. (2.47). Their incoherent sum is drawn as a black line. In (b), the single film intensities are again represented by the red and blue lines. Together with the interference part in green (representing the last 5 lines in Eq. (2.47)) the complete solution for the coherent bilayer is plotted in black.
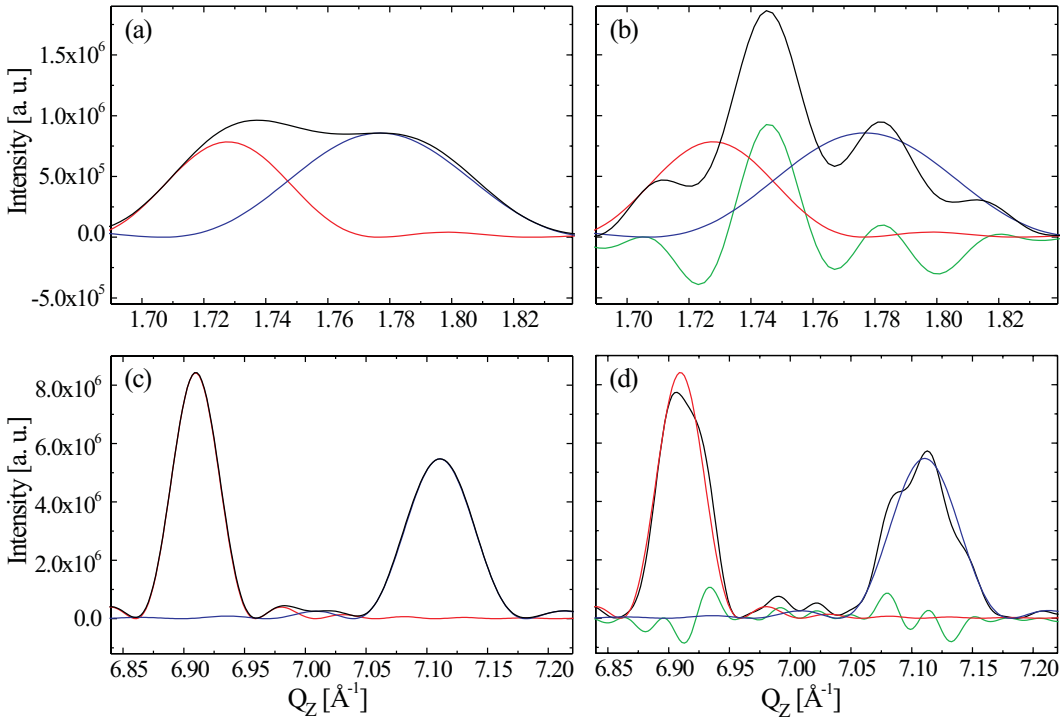

Figure 2.21: Effect of interference in an epitaxial bilayer. (a): Plot of the diffracted intensities from a 89 Å PbSe film (blue line) and a 127 Å EuSe film (red) together with there incoherent sum across the (111) reflection. (b): Interference part (green) and coherently diffracted intensity(black) from the films in (a) when grown on top of each other. (c)+(d): Similar plots as in (a)+(b), but for the (333) reflection.

It demonstrates that the two separate peaks from the films, representing the two lattice parameters of EuSe and PbSe have rather little influence on the shape of the total intensity described in the complete solution of Eq. (2.47). It is rather the interference

part, which influences the position of the maximum. In Fig. 2.21 (c)+(d), the same plots as in (a)+(b) are shown for the (333) reflection. The better discrimination of strain in reciprocal space now leads to a significantly lower interference between the amplitudes of both films. Therefore the single peak positions and the total intensity show a better agreement than for the (111) reflection.

So far, we have ignored resonant effects in the simulations of the bilayer diffraction shown in Fig. 2.21. In the following we will include and try to exploit them in the materials to be investigated in this work. The advantages that we might deduce from Fig. 2.21 in measuring high indexed reflections can in reality be quickly consumed by other effects. These are $e.g.$ the weakening of the higher indexed reflections by the decay of the atomic scattering factor or the Debye-Waller factor. Furthermore, other effects like thermal diffuse scattering might affect the measurement. Therefore it appears reasonable to invest more effort in the possibilities that are offered by low indexed reflections. For the IV-VI semiconductors studied in this work, the interest focussed on the possibility of a precise strain measurement inside a europium-chalcogenide layer, typically EuSe. The strain was caused by the underlying lead-chalcogenide buffer, and the lead chalcogenide layers in the multilayer. in our cases PbSe or an alloy $PbSe_{1-x}Te_x$. To achieve a pseudomorphic strain in a multilayer to the in-plane lattice constant of the PbSe, one usually has to supply a certain material overweight of PbSe. Therefore these layers were thicker than the EuSe-layers. This, together with the fact that Pb (82 electrons) is a very strong scatterer, leaves a particular challenge to extract the EuSe lattice-parameter in a diffraction experiment. As discussed before (chapter 2.5.1), resonant effects open up the opportunity to change the intensity of superstructure reflections significantly. This however requires the similarity of the two atomic scattering factors that form the compound. If we want to suppress PbSe with this method, we have to go in resonance at the Pb M_V edge, at around 2500 eV.

Using Eq. (2.47), we may consider a system consisting of a 400 Å PbSe film, and a 40 Å EuSe film that is pseudomorphically strained to the PbSe in-plane lattice. As before, the growth direction shall be (111). We may then chose the appropriate values for the atomic scattering factors and their phases, as plotted $e.g.$ for Pb and Se in Fig. 2.13, and enter Eq. (2.47). In Fig. 2.22 the evaluation of the diffracted intensity is plotted for two different x-ray energies. The graphs show the separate contributions of the 40 Å EuSe film (red line) and the 400 Å PbSe film (blue line). The black line represents the coherent diffraction pattern from the epitaxial bilayer according to Eq. (2.47). Fig. 2.22(a) represents the situation at 2490 eV, below the Pb M_V-edge, whereas (b)

is calculated for 10000 eV, as a representant for any "normal" crystallographic x-ray energy. The comparison clearly expresses a similarity of the total diffraction pattern to that of the PbSe film in (b). An evaluation of the peak position would indeed determine the PbSe out-of-plane lattice parameter in this structure. In (a), the broad envelope of the central peak corresponds to the width and the centre of the EuSe film.

It is important to note, that this strong accentuation of the EuSe features in the complete diffraction pattern for such a structure is not possible at any other x-ray energy, as can also be deduced from Fig. 2.13. A strain analysis in the EuSe layers therefore requires the use of anomlous diffraction at x-ray energies in the vicinity of the Pb M_V-edge below 2500 eV.
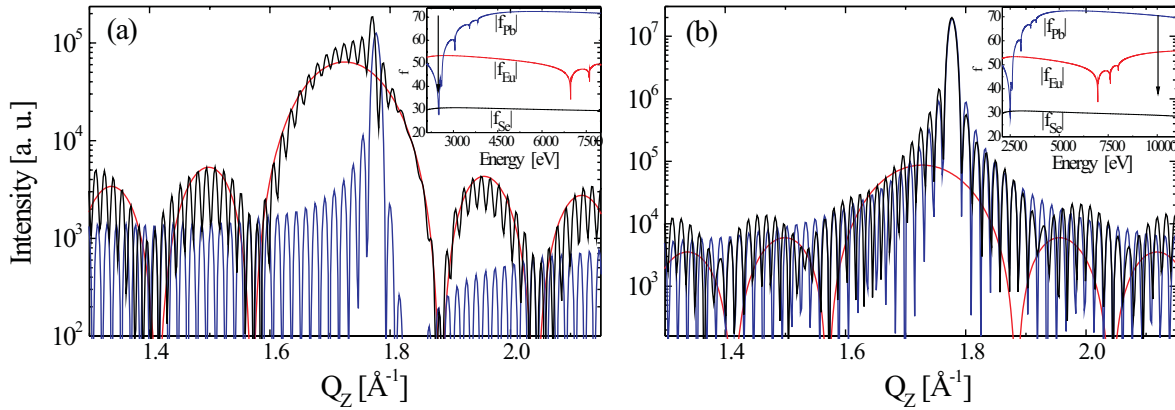

Figure 2.22: Simulation of a 40 Å EuSe/ 400 Å PbSe bilayer for two different energies. The black lines are calculations performed according to Eq. (2.47). the red lines represent the diffraction from the single EuSe film, the blue lines the one from the single PbSe film. In (a) the diffraction pattern corresponds to 2490 eV, in (b) to 10000 eV. The insets are plots of the atomic scattering factors for Pb, Eu and Se as a function of energy. Black arrows mark the energies for which the simulations were performed.

2.5.5   Some remarks about multilayers

The 2D semiconductor hetero-structures studied in this work consist of multilayers rather than single films or bilayers. One simple form of a multilayer is the periodic replication of a bilayer. These systems are common structures applied as quantum well structures or Bragg mirrors in solid state lasers [46, 47]. Using the solutions we have gained for bilayers in section 2.5.4 and applying the convolution theorem from Eq. (2.14) we can deduce a few simple rules for the interpretation of the kinematic diffrac-

tion pattern from a multilayer. However, we should keep in mind that in the case of strong reflections, as in the reflectivity regime close to the origin of reciprocal space and at strong Bragg reflections, dynamical effects might have an important impact on the diffraction. The considerations pointed out here refer only to the kinematical case, where the purely mathematical treatment of the Fourier transform in reciprocal space has to be taken into account. The real space of a simple multilayer consisting of M bilayers can be described as a convolution between a sum of M delta functions displaced with respect to each other by the thickness of one bilayer period. Applying the convolution theorem, we can then state that the Fourier transform of this structure is the product of the grating interference function from a grating with M slits, and the Fourier transform af a bilayer. In reciprocal space, we therefore expect to see the envelope of the bilayer diffraction, modulated with the interference peaks of the grating diffraction function. These peaks are separated from each other by $\frac{2\pi}{D}$, D being the thickness of the bilayer (one multilayer period). Every peak represents an optical path difference between neighbouring bilayers of an integer multiple of 2π. This path difference is 0 for forward scattering, *i. e.* for Q=0. It appears therefore suitable to introduce the index "0" for the path difference of $0*2\pi$. These regularly spaced superlattice peaks are now enveloped by the Fourier transform of the bilayer. At the Bragg peak positions of the bilayer, we will therefore strongly pronounce the visibility of the superlattice peaks but their positions are not influenced. The position of a Bragg peak is defined by an optical path difference between the atoms of the corresponding netplanes of 2π and therefore is to be found at the position $\frac{2\pi}{d_1}$, d_1 being the netplane distance in *e. g.* film 1 in the bilayer. If now the thickness D of the bilayer is not an integer multiple of this atomic distance d_1 in *one* of the two bilayers, the Bragg peak position indicating the atomic distance will *not* coincide with the position of a superlattice peak. In real systems it is indeed very unlikely, that D is an integer multiple of d_1 or d_2, as d_1 and d_2 stem from different materials and therefore differ slightly. It should therefore be avoided to attribute the superlattice satellites observed in the vicinity of a Bragg peak to be a precise measure for the lattice parameter inside the bilayer structure. Furthermore, the lattice parameter or the distribution of lattice parameters in the case of a non-uniform distorted structure, is expressed in the shape and position of the envelope function of the superlattice peaks. A sketch of the situation in real- and reciprocal space is presented in Fig. 2.23. The convolution of the two structures grating and bilayer produces the multilayer in real space. The multiplication of their Fourier transforms leads to the multilayer in reciprocal space. As already mentioned, multiple scattering effects might change this pattern under the influence of strong Bragg reflections. The description

to be chosen in this case is usually an approximation for a multi beam case and the interpretation of the positions of the interference peaks will be less straightforward [48].
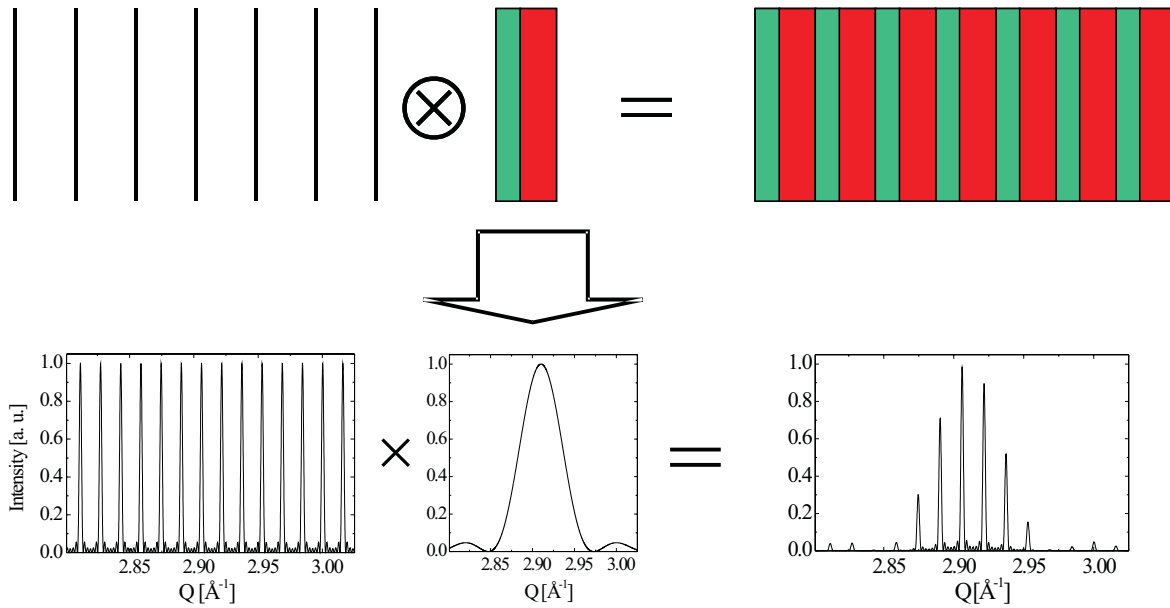

Figure 2.23: Multilayers in real- and reciprocal space. In real space, a multilayer can be described as the convolution of a grating of delta functions and a bilayer. Its Fourier transform is therefore the product of the Fourier transforms of a grating and a bilayer.

Fortunately we will look at Bragg reflections, which are weak enough to apply the mathematical treatment of the Fourier transform and hence justify to neglect dynamic effects. In addition the high absorption of the low energy x-rays used in the diffraction from multilayers in this work causes the penetration depth of the waves to be limited by inelastic absorption rather than by extinction.

„Die circa fünfzig seitdem noch hinzuent-
deckten Planetoiden sind eine Neuerung,
von der ich nichts wissen will. Ich mache
es daher mit ihnen, wie mit mir die Phi-
losophieprofessoren: Ich ignoriere sie; weil
sie mir nicht in meinen Kram passen"
Arthur Schopenhauer, „Aphorismen zur
Lebensweisheit", Diogenes Verlag Zürich
(1977).

3 Experimental Details

3.1 Objective of the experiments

This section shall give a brief overview about the investigated sample system and the objective of the x-ray studies.

3.1.1 Strain tuning in magnetic semiconductor multilayers

The magnetism in materials in general can be both of nuclear or electronic nature. For the magnetic materials that are omnipresent in our temporary information technology, it is always the electronic or also called atomic magnetism. The macroscopic magnetic properties of a material as ferro-, ferri-, or antiferromagnetism depend on the coupling of the magnetic spins of the atoms. The latter have their origin in the uncompensated spins from electrons, or in the more rare cases, from the unsaturated orbital moments. The quantum mechanical interaction between these spins illustrates the nature of their coupling which might be *e. g.* parallel in the case of ferromagnetism or antiparallel in the case of antiferromagnetism. As the driving forces for parallel or antiparallel ordering are dependent on the spin-spin distance as well as on the chemical environment of the spins, this opens up a wide field of possible applications in epitaxy. Thin layers in heteroepitaxy are generally strained by the misfit of the crystal lattice with the underlying material. In principle, the strain and therefore the spin-spin distance in a magnetic film can be influenced by the choice of the lattice parameter of the materials on top of which the magnetic material is grown.

In the case of europium chalcogenides, studies of the bulk material under high pressure have demonstrated a significant influence of the lattice parameter on the nature of the magnetic order and the ordering temperature [49, 50, 51]. The effect of influencing the lattice parameter can also be achieved by epitaxial strain of thin films. The growth of superlattices of lead-/europium chalcogenides on top of lead-chalcogenide buffer layers results in a semiconducting system with a variety of exotic properties. The small misfit of about 1 % between PbSe and EuSe leads to a high growth perfection with pseudomorphic distortions in both materials. The amount of strain in the EuSe can be tuned via changing the lattice parameter of the PbSe by alloying it with Te. $PbTe_xSe_{1-x}$ crystallizes in the same crystal structure, but with a lattice parameter dependent on the Te-content x. The fundamental band gap of the lead chalcogenides corresponds to energies in the infrared regime. For EuSe it extends to the visible and can be influenced by magnetic fields and strain [52, 53]. In the case of thin films, quantum well effects lead to additional changes in the band structure and the magnetic

properties. The first task in the study of the influence of epitaxial strain in thin films on their magnetic and electronic properties is to *measure* the amount of strain induced in a selected material via epitaxy. Furthermore the quality of the growth concerning the interfaces is important for the confinement effects achieved in a quantum well structure. In this work, anomalous x-ray diffraction will be employed to investigate strain and interdiffusion in lead-/europium chalcogenide multilayers. The anomalous technique allows us to selectively look at the lattice parameter in either of the two materials. The determination of strain is crucial in the interpretation of the change in the magnetic properties. For the samples described in this thesis, the latter were measured via superconducting quantum interference devices (SQUID) and neutron scattering, and will be published elsewhere [54].

3.1.2 Ordering and interdiffusion in semiconductor quantum dot systems

Semiconductor quantum dots have attracted interest world wide as they offer fascinating opportunities for the fabrication of novel optoelectronic devices. Confinement effects in general strongly affect the density of states in the system. In a perfect "0-dimensional" system, the density of states corresponds to set of delta functions. In the case of quantum well laser diodes for example, the threshold current is reduced when using quantum wells (2D-confinement) as the active medium vs. the bulk. It can be further reduced by the use of quantum dots. The growth of these nanocrystals is less straightforward than the growth of quantum wells. In the Stranski-Krastanow growth of such quantum dots a fundamental morphological instability in the heteroepitaxy of semiconductors with a certain lattice mismatch is exploited, which is driven by the elastic relaxation of strain energy at the expense of an increase of surface energy [55]. The advantages of this self organized bottom-up growth versus lithographic top-down methods are the very small achievable sizes and dislocation free structures. However, besides the size of these dots, their size distribution plays also a crucial role. An ensemble of quantum dots with a large size distribution shows a broadening of the discrete electronic energy levels as compared to a mono disperse system. The highest spatial order together with the narrowest size distribution in quantum dot systems grown by epitaxy is observed in IV-VI semiconductor hetero structures [41, 84]. PbSe quantum dot embedded in a PbEuTe matrix form a 3D ordered arrangement of quantum dots. The strain driven almost perfect ordering of these dots also supplies their excellent monodispersity in size. When deposited on a PbTe (111) surface, PbSe forms trigonal pyramids with $\{010\}$ facets. Overgrowth of these pyramids with $Pb_{0.92}Eu_{0.08}Te$ and successive deposition of PbSe and $Pb_{0.92}Eu_{0.08}Te$ cap layers leads to the 3D superlat-

tice of PbSe quantum dots.

X-ray diffraction in general is used to characterize the degree of order in such structures. In this work, we will take a more detailed look at the intensity distribution in reciprocal space for various x-ray energies. This technique will reveal the orientation of internal interfaces of the quantum dot superlattice. The existence of well defined interfaces is of interest for the confinement effects induced by 0-dimensional quantum dots. Furthermore we show with anomalous x-ray diffraction that the overgrowth with PbTe instead of $Pb_{0.92}Eu_{0.08}Te$ significantly enhances the dilution of the PbSe dots by interdiffusion. Furthermore, the shape of the dots and the orientation of their facets is affected by the overgrowth.

Another system of nanocrystals grown by epitaxial self-organization, SiGe islands on a Si(001) surface, are also investigated. SiGe islands on Si have been the subject of numerous studies, such islands show interesting morphological shape transitions as a function of growth parameters [56]. Despite the fact that they consist of semiconductors with an indirect energy gap, electroluminescence even at room temperature has been achieved from buried Ge rich islands in Si at about a wavelength of $1.3\,\mu m$ [57]. The recombination energy of the electron-hole pairs depends crucially on the size, the shape, the strain status and the chemical composition of the islands. From a series of studies, including e.g. transmission electron microscopy (TEM) investigations, using energy selective imaging or digital image analysis, it is known that intermixing in such islands exists, but difficulties in the quantification of the composition profile along the growth direction remain [77, 58, 59]. This profile, together with the strain distribution is crucial for the electronic band structure of the embedded islands and thus for any application. The experiment presented here shows that anomalous x-ray diffraction can indeed be used to obtain the necessary chemical sensitivity for a *direct* determination of composition profiles in SiGe islands along the growth direction. A lateral resolution of the Ge profile cannot be obtained by this method.

3.2 Experimental instrumentation for anomalous diffraction

3.2.1 Experimental environment for x-ray diffraction over a wide energy range

The experimental requirements for x-ray diffractometers depend on the samples to be investigated and on the x-ray source. For a divergent source the angular resolution of the mechanical equipment is less important than in the case of high-resolution diffraction with the use of synchrotron radiation. In the case of anomalous diffraction another important point has to be considered. If the experimental setup is supposed to reach high energy ranges, the angular *resolution* can be of importance for short x-ray wavelengths. With $Q = \frac{4\pi \sin \theta}{\lambda}$ as the momentum transfer for the Bragg angle θ and the wavelength λ we can state for our Q-resolution ΔQ:

$$\Delta Q = \frac{\Delta \Theta 4\pi \cos \Theta}{\lambda} \tag{3.1}$$

For a given angular resolution $\Delta \Theta$ of the diffractometer, the Q-resolution gets worse for shorter wavelengths, therefore for high energies, the angular *resolution* is of importance. On the other end of the energy scale, for very low x-ray energies and very long wavelengths, the maximum achievable angular *range* of the diffractometer becomes important.

The low end of the energy scale is indeed limited by the diffraction angle of the monochromator itself. As the monochromator is in general a crystal, the Bragg reflection with the lowest index sets the limit for the lowest achievable energy. Due to technical limitations the backscattering geometry is in general not applicable. At the anomalous scattering beamline ID01 at the ESRF in Grenoble, the maximum tilt angle of 70° of the Si(111) double crystal monochromator sets the lowest x-ray energy to 2100 eV compared to possible 1977 eV for backscattering at a Bragg angle of 90°. In diffraction from the sample, anomalous diffraction at very low energies faces the similar problem of a low number of achievable Bragg reflections. Therefore we state, that for anomalous or resonant *diffraction* the useful energy range ends around 2000 eV at the "*Bragg-limit*".

As an example for the limitations in reciprocal space for *coplanar diffraction* (see section (3.3.2) two systems at two absorption edge energies are presented in Fig. 3.1. The reflections accessible for a (111) surface of PbSe at 2500 eV (Pb M$_V$-edge) are plotted

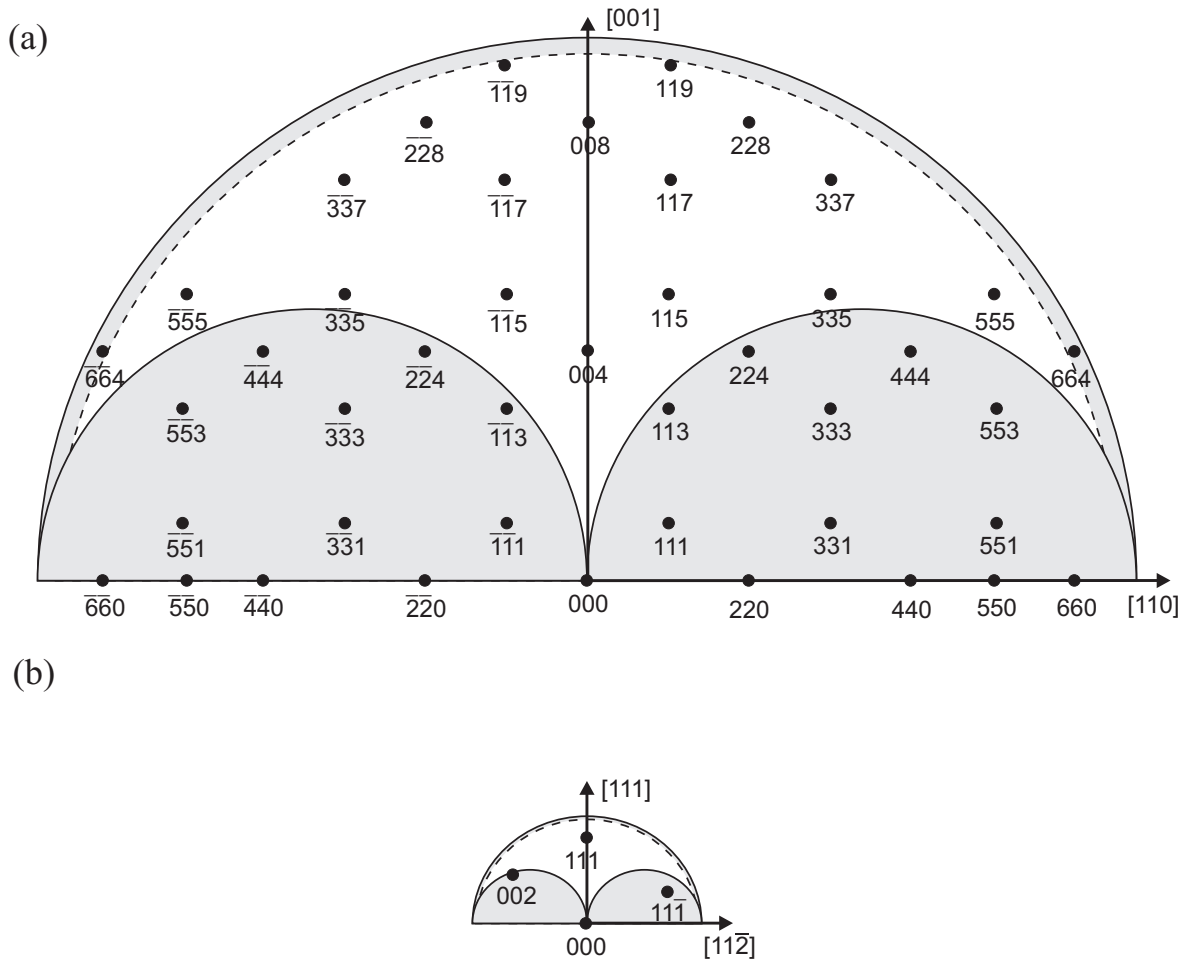in (a), those for a Si (001) surface at 11103 eV (Ge K-edge) are plotted in (b).

Figure 3.1: Limits in reciprocal space for diffraction at a fix energy. (a): Accessible reflections in the (100) plane of a Si (001) surface at 11103 eV (Ge K-edge). The large hemisphere indicates the maximum momentum transfer for backscattering ($Q_{max} = \frac{4\pi}{\lambda}$. The small grey hemispheres cover the area that is inaccessible in the coplanar scattering geometry. The reflections in this part can still be accessed via other scattering geometries. (b): Equivalent sketch for the $(1\bar{1}0)$ plane of a PbSe (111) surface and an x-ray energy of 2500 eV (Pb M_V-edge).

Apart from this fundamental restriction in the accessible Q-range other technical difficulties appear in the low energy regime. The absorption of x-rays by all materials becomes important, leading to difficulties due to intensity losses in windows and air. Figure 3.2 shows a plot of the transmitted intensity through 400 μm beryllium, 100

μm capton (Polyimide) and 10 cm air in the x-ray energy range from 2000 eV to 8000 eV. Capton and beryllium are materials of choice for x-ray windows. In particular the absorption from air becomes a problem below 5000 eV. It is this absorption problem, which sets the experimental limits on the exploitation of the low x-ray energies in diffraction.
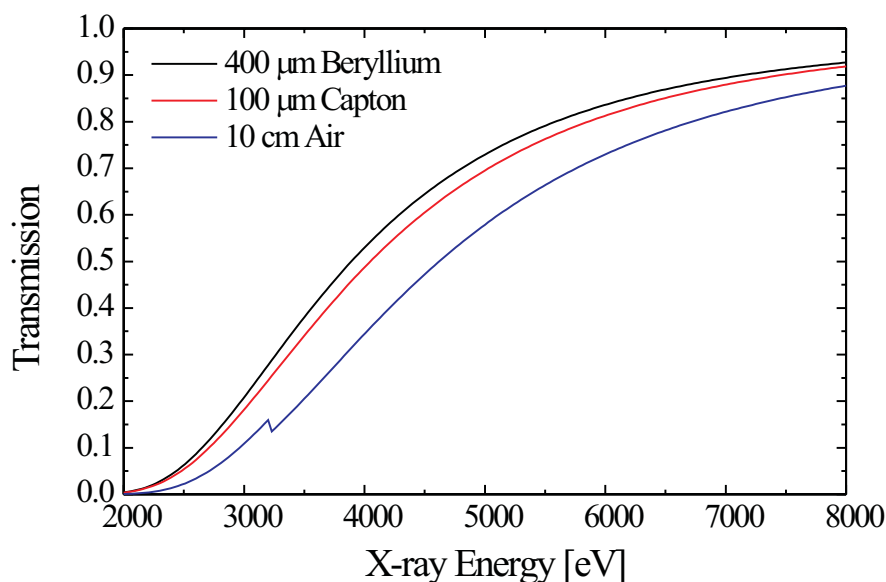
Figure 3.2: X-ray transmission through windows and air. The transmitted intensity is plotted as a function of energy for 400 μm beryllium (black line), 100 μm capton (red) and 10 cm air (blue). At 3200 eV, the Ar K-edge is visible in the air absorption.

The strong absorption of x-rays in materials requires additional provisions in the sample environment. If the sample surface is exposed to air, the ionization by the x-rays induces ozone generation. The latter then chemically attacks the sample and can lead to corrosion of the surface. This is of particular importance in anomalous scattering as the main ozone generation is caused rather by the photo- and Auger electrons emitted from the sample than from the x-ray beam itself. If we probe in the vicinity of an absorption edge, and then exceed the edge with the x-ray energy, we will cause a strong increase in the photoelectron emission. For the diffraction experiments carried out in this work, two solutions were applied. In the case of x-ray energies higher than 6000 eV, the sample was kept in a capton tent filled with He. For lower energies, the whole sample environment was evacuated to 10^{-2} mbar. A photo of the He-tent is presented in Fig. 3.3 (a), together with an example of a chemically corroded sample in (b) after

exposure to a 2400 eV X-ray beam under poor vacuum conditions (10 mbar).
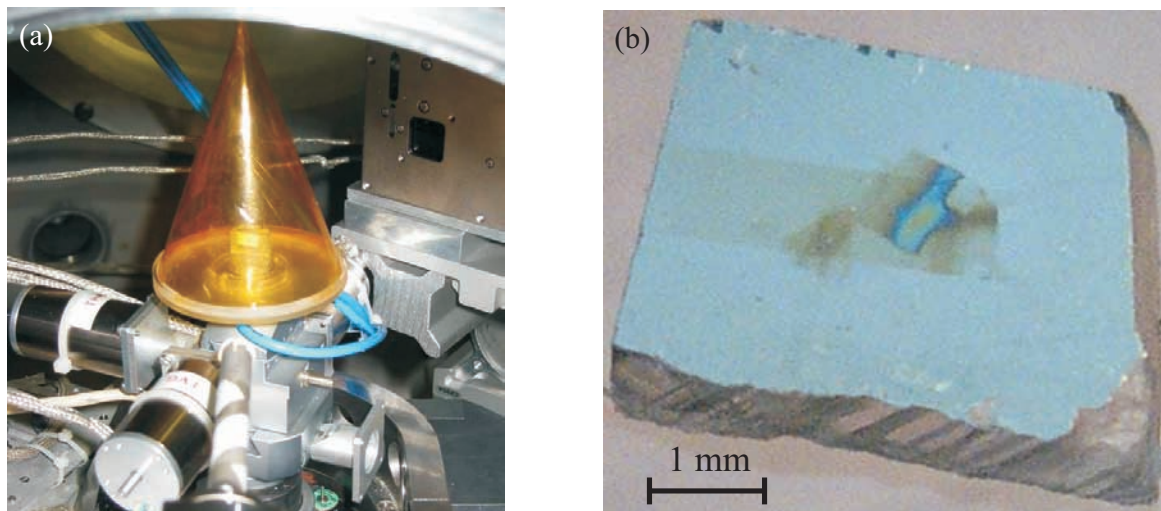

Figure 3.3: (a): Sample holder with capton tent to keep the sample under helium atmosphere during the experiment. (b): Chemically attacked surface due to irradiation under a low pressure air atmosphere of about 10 mbar.

3.2.2 The Beamline ID01

All diffraction experiments presented in this work were carried out at the beamline ID01 at the ESRF in Grenoble. The beamline is dedicated to anomalous scattering and diffraction. The angular range of the double crystal monochromator permits the use of x-ray energies between 2100 eV and 40000 eV. The high energy limit is not a geometrical restriction, but rather limited by the decrease in the photon output of the x-ray source for higher energies. As an x-ray source two insertion devices can be chosen. For the majority of experiments, a 42 mm undulator with 38 periods is used. Its gap can be varied between 16 mm and 200 mm. Depending on the required energy, the 1st, 3rd or 5th harmonic is chosen. For x-ray energies below 2300 eV, a 70mm wiggler can be used. The minimum gap of 20 mm is set by the heat load that otherwise would damage the liquid nitrogen cooled monochromator. The gap of the wiggler can be varied between 20 mm and 300 mm. In the low energy regime (below 5000 eV), the gap is wide open and therefore the wiggler operates in the undulator regime. After the selection of the x-ray energy via the gap of the insertion device and the monochromator angle, the "monochromatic" x-ray beam still contains higher harmonics. If *e.g.* the x-

ray energy is selected to be 8000 eV on the 1st harmonic of the undulator and the Bragg reflection from the Si(111) monochromator, we will get as well 24000 eV x-rays from the 3rd harmonic being reflected as the Si(333) reflection at the same Bragg angle as the Si(111) reflection. The suppression of these contributions is achieved by two mirrors. Figure 3.4 presents the arrangement of the optical components of the beamline ID01.
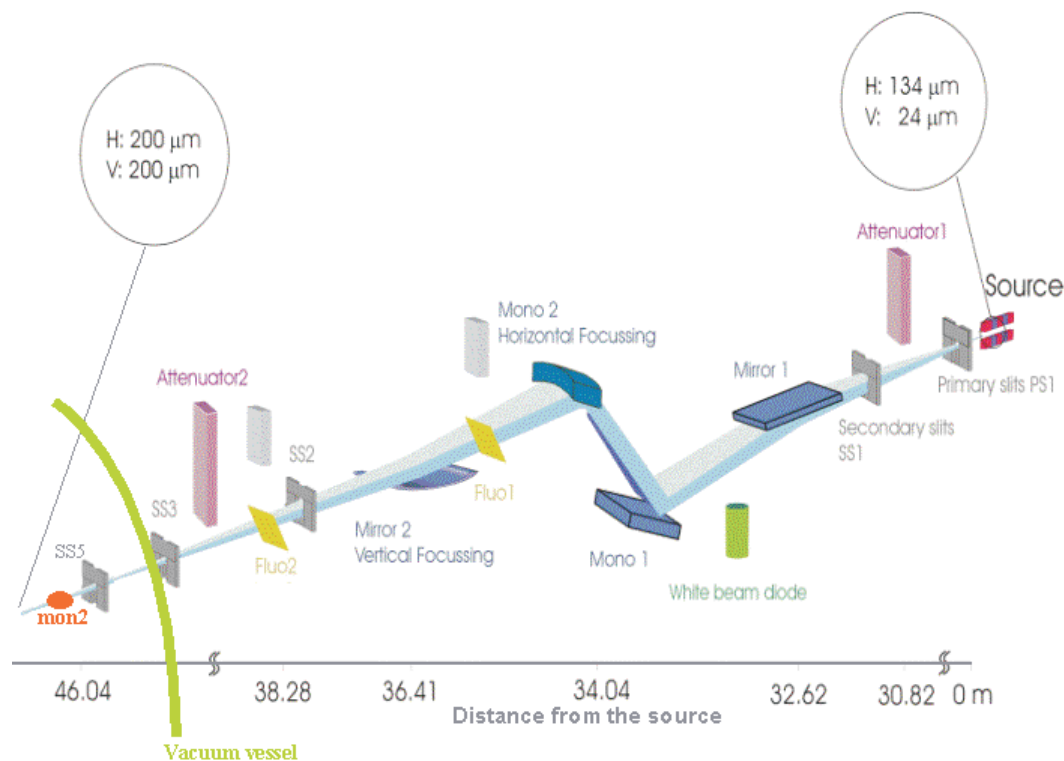

Figure 3.4: Schematic view of the beamline ID01 optics. The drawing is not to scale but the distances of the components to the x-ray source are indicated. The fluorescent screens Fluo1 and Fluo2 can be used to visualize the beam or can be exchanged by thin scattering foils to monitor the beam intensity.

The mirrors sandwich the monochromator and make sure that the exiting beam is fixed at the sample position when the energy is changed. The fact that the critical angle of total external reflection changes significantly with the x-ray energy permits the choice of an incident angle on the mirror that is below the critical one for the 1st harmonic, but well above the critical angle for the 3rd harmonic. The second mirror also serves as a focussing device in the vertical direction. The slits SS2 and SS5 can serve to set a collimation path to define the beam divergence. After SS5, before the sample, a scattering foil labelled "Mon2" serves as a intensity monitor for the primary beam. Downstream of the sketch in Fig. 3.4 the diffractometer is situated. It is mounted in a vacuum vessel that permits windowless operation of the beamline. The diffractometer

works in the "4S+2D" geometry with 4 sample circles μ, θ, χ and ϕ and 2 independent detector circles δ and γ [60]. A drawing is presented in Fig. 3.5 (a) together with a photograph in (b).
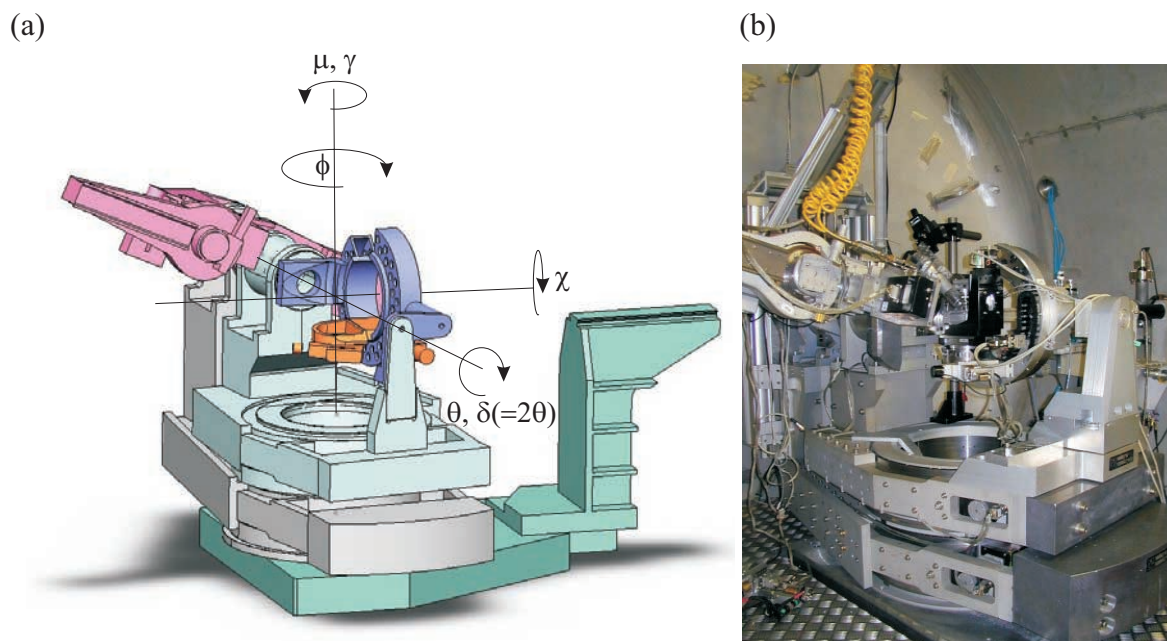
(a)   (b)

Figure 3.5: (a): The "4S+2D" diffractometer of the beamline ID01. The axes of the 4 sample circles μ, θ, χ and ϕ and the 2 independent detector circles δ and γ are indicated. The beam enters from the right, in this diffractometer position along the χ-axis.

3.2.3   Low energy detectors

In the previous section, a few problems concerning diffractometry at the low energy Bragg limit were discussed. As the absorption problem can be overcome at the vacuum diffractometer at ID01, the question of the detection of low energy photons arises. In this energy regime, the difficulty of the detection systems designed for rather standard x-ray energies above 5000 eV can be split into two general problems:

1.: These detectors are usually equipped with windows in order to be protected from light or for thermal isolation. Therefore the window absorption problem arises.

2.: The problem of the vacuum environment causes particular difficulties due to over-heating of preamplifier electronics that are designed to run under atmospheric pressure. For high-voltage supplies, the rather poor vacuum in the millibar regime can provoke flashovers and therefore destroy high voltage devices.

These two points were solved for two different detection systems. The first detector to be used at energies down to 2200 eV was a Roentec XFlash 1000 silicon p-i-n diode.

This detector is equipped with a 8 μm thin Be-window, having a transparency of almost 90 % for 2000 eV photon energy. This semiconducting diode is operated in the reversed direction with a voltage close to the breakdown voltage of the p-n junction. This leads to a charge carrier depletion in the diode that thereby becomes insulating. To increase the size of the active volume, an undoped highly pure Si crystal is placed between the p- and the n-doped parts. The reversed bias voltage leads to a depletion of the whole intrinsic conducting Si, giving the name to the p-i(intrinsic)-n diode. An ionizing particle or photon can now create electron-hole pairs in the depleted volume and leads to a charge pulse that is amplified and detected. The number of created electron-hole pairs defines the energy of the photon. The energy resolution of such semiconductor detectors is of the order of 2-3%. They are therefore suited for the particular use in anomalous diffraction as they permit a discrimination of elastic and inelastic contributions (as fluorescence or resonant Raman scattering). The operating voltage of the diode and the preamplifier card is below 30 V, therefore no particular problems in the feedthrough of high voltage at low pressures occurs. However the preamplifier card cannot be run under vacuum conditions as electronic components such as transistors are dependent on convection cooling in an air atmosphere. Furthermore, the detector head is Peltier cooled to suppress thermal noise in the diode and the field effect transistor as the first amplifier level. The Peltier element is itself cooled by a fan. To keep these devices in normal operation even when used at the in-vacuum diffractometer at ID01, the detector head was encased in an aluminium box that was supplied with a permanent air-flow via hoses. Figure 3.6 (a) shows the XFlash head and the vacuum compatible version in (b).
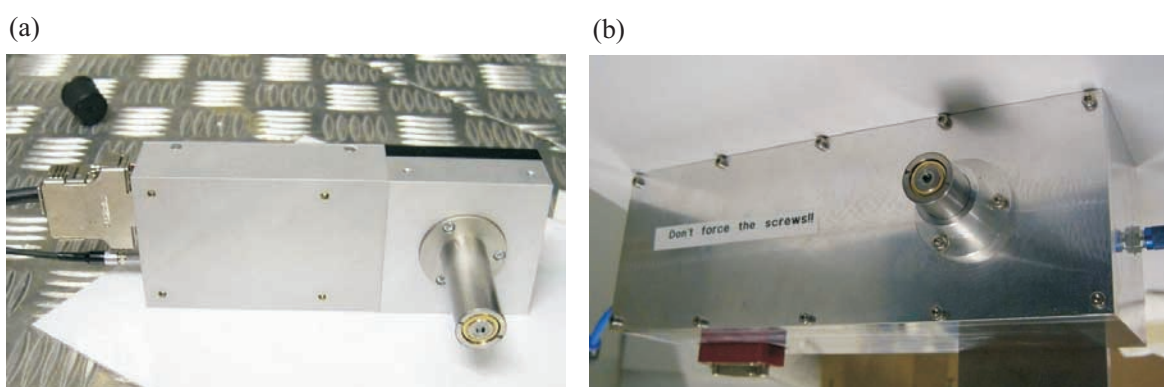
(a)

(b)

Figure 3.6: (a) The Roentec XFlash 1000 p-i-n diode detector. The active area measures 10 mm^2 in size and is situated in the centre of the round "nose". (b) Encased vacuum compatible version of the detector in (a).

An energy dispersive spectrum recorded from a radioactive source can be used to

calibrate the absolute energy resolution. The signals as read out by a multichannel analyzer are plotted in Fig. 3.7. The two highest peaks can be attributed to the Mn K_α and K_β emission energies at 5895 eV and 6490 eV. More precisely they are called "full energy peaks". To their low energy side one can find a more or less continuous intensity distribution together with another small peak about 1740 eV below the Mn K_α peak. This is the Si K_α escape peak, caused by ionization of Si atoms in the p-i-n diode crystal and their successive K_α x-ray emission. If one of the emitted Si K_α photons escapes from the crystal without further creation of electron-hole pairs, the exact amount of the Si K_α photon energy is missing from the full-energy peak. The continuous intensity distribution below the full energy peaks is called the "Compton-continuum" as it is caused by energy loss of the photons due to (multiple) Compton scattering processes either before entering the detection volume or by Compton scattered electrons escaping the detection volume. At the position of twice the full energy peak we observe another weak maximum caused by pile-ups. If the coincidence of two photons occurs within the collection time of the created electron-hole pairs, their created charge amount is accumulated and detected as one event with an energy twice as high as from one photon.
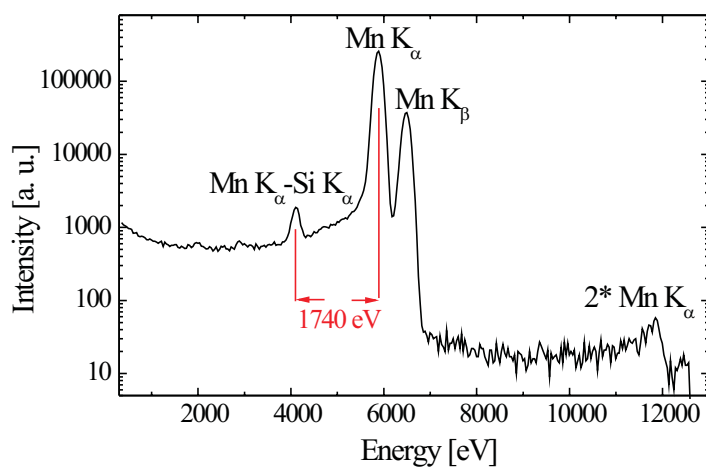
Figure 3.7: Energy spectrum of Mn K-fluorescence recorded by a Roentec XFlash 1000 p-i-n diode. The radioactive source emits Mn K_α and K_β lines. The Si detector spectrum shows an additional Si K_α escape peak and the continuous compton escape spectrum.

Together with the high quantum efficiency of more than 80 % at 2000 eV, the energy resolution and the high dynamic range of up to 250,000 counts per second this detector presents no disadvantages compared to any other point-detector at higher x-ray energies.

For several diffraction setups it is, however, of a significant advantage to work with

a linear 1D detector, rather than a point detector. A very reliable system employed in grazing incidence diffraction and reciprocal space mapping is a position sensitive detector (PSD-"Braun"-detector) based on gas ionization. The detector consists of a 50 mm long counting tube with a square cross section and a thickness of 8 mm. It is filled with $Ar_{0.9}(CH_4)_{0.1}$ as detection gas at 7 bar pressure and operated at 3700 V. The photons enter the tube through a 400 μm thick beryllium window. The position sensitive device is the back of the tube. It is equipped with a silver cathode that consists of two set of triangular teeth isolated with respect to each other. If a photon ionizes the counting gas, the electrons are accelerated towards the counting wire in the centre of the tube, whereas the ion cascade reaches the cathode at the back as a relatively broad spot. Depending on the position of the spot along the tube, the ion current is detected in different proportions by both sets of triangles. The differential signal from both "jaws" is converted into a position along the tube. The spatial resolution achieved by this process is about 100 μm. Figure 3.8 (a) shows a sketch of the position detection system. A photograph of the detector head is presented in (b).
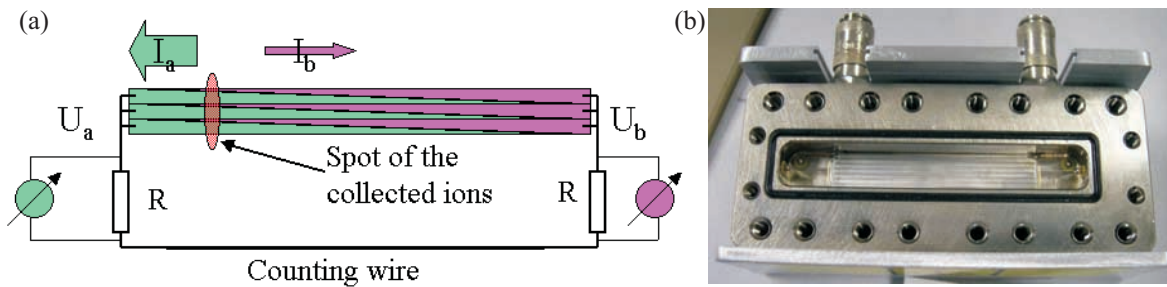
Figure 3.8: Position sensitive detection principle of the Braun PSD. (a): Sketch of the cathode on the back of the detection tube, consisting of two sets of triangles isolated with respect to each other. The position of the ion spot is determined through the ratio $\frac{I_a - I_b}{I_a + I_b}$. (b): Photograph of the counting tube. The entrance beryllium window is removed and the silver cathode on the backside is visible.

To extend this system for low energies, the first problem is the thickness of the beryllium window. The thickness of 400 μm is determined by the required mechanical stability from an internal gas pressure of 7 bar. The first step to thin the window is a reduction of its size. In the original PSD, the window length was 50 mm, its height 10 mm. In the low energy version developed in this work, a height reduction of the window to 1 mm was chosen. The detector front was replaced by a steel plate that supported the beryllium window leaving only a 1 mm wide unsupported slit. The beryllium window used in this combination is only 100 μm thick and withstands pressures up to 5 bar. The reduced pressure can be tolerated for lower energies, as the absorption in the gas

rises. Indeed pressures between 3-4 bar where found to be the ideal operating pressures at photon energies from 2500-4500 eV. As the Ar K-edge is found at 3200 eV, the use of $Ar_{0.9}(CH_4)_{0.1}$ as detection gas is not suitable in the low energy regime. The choice of $Ne_{0.9}(CH_4)_{0.1}$ avoids this problem. Furthermore, the Ag L_{III}-edge at 3351 eV, leads to fluorescence from the Ag-cathode if used in this energy regime and therefore significantly affects the spatial resolution of the detector. To be dedicated to this energy regime, the low energy PSD was equipped with a copper cathode, thereby limiting its use to energies below the Cu K-edge threshold of 8900 eV.

Having all the window and fluorescence problems solved, the problem of overheating of the electronics under vacuum conditions has to be treated in the same way as at the point detector presented before. The gas counter head together with the preamplifier was encased in an aluminium box that was flushed with air via a hose feedthrough in the vacuum vessel. Another set of flexible gas pipes supplied the counting gas. The third problem to be overcome is the high voltage supply under low pressures in the flashover regime around 1 mbar. The high voltage was generated by a DC-DC voltage converter that was included in the aluminium box and supplied with a 12 V laboratory source from outside the vacuum vessel. A photograph of the interior of the aluminium box is presented in the Fig. 3.9.
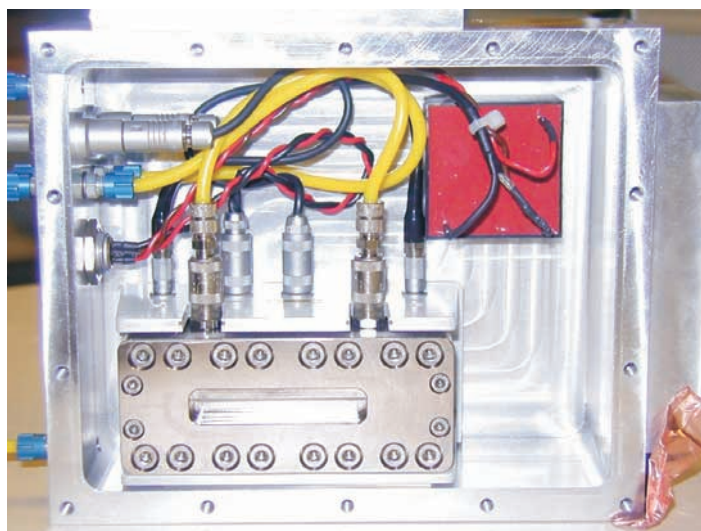
Figure 3.9: The encased vacuum PSD for low energies (cover removed). The steel front plate of the detector head at the bottom leaves only a 1 mm slit of unsupported beryllium. The red box in the upper right is the high voltage converter, the yellow hoses supply the detector gas.

Taking into account the 50 % transparency of the 100μm beryllium window at 2500 eV and the 80 % effiency of the counting gas ($Ne_{0.9}(CH_4)_{0.1}$ at 3 bar pressure) the

quantum efficiency of this detection system is still 40 %. When recording reciprocal space maps, this slight loss of intensity is easily compensated by the amount of points recorded along the 1D detector. Another important feature is the ability to count single photons with neglible background noise, even at energies as low as 2000 eV. In the case of very weak signals, this means that the photon statistic is indeed the experimental limit, rather than *e.g.* read-out noise which is usually present in CCD devices.

3.3 Diffraction in angular and reciprocal space

3.3.1 Grazing incidence diffraction

In the case of x-ray diffraction studies on nanostructures or surfaces, an appropriate scattering geometry that is often chosen is the grazing incidence diffraction (GID) setup [35, 36]. It exploits the fact that the refractive index of condensed matter is slightly smaller than 1. According to Snell's law an angle of total external reflection is present at the interface between *e.g.* a perfect crystal surface, and vacuum or air both which have a refractive index equal to 1 [61]. The angle of total external reflection depends on the material and the x-ray energy, as the dielectric properties are energy dependent. In the case of "real" surfaces, other effects on the reflectivity have to be considered. The most important ones are oxide layers and surface roughness. Both tend to influence the refractive index of the surface and hence change its reflectivity behaviour [62, 63, 64]. In the investigation of nanocrystals on top of the surface of a perfect crystal the GID geometry is used to suppress the background scattering that stems from the bulk crystal. For the GID experiments as performed in this work, grazing incidence and exit conditions where chosen for the incident and exit angles α_i and α_f. The intensity distribution along the exit angle α_f was recorded using a position sensitive detector (PSD), which was mounted perpendicular to the surface. This geometry gives access to Bragg reflections that lie in the surface plane. This situation is sketched in Fig. 3.10.
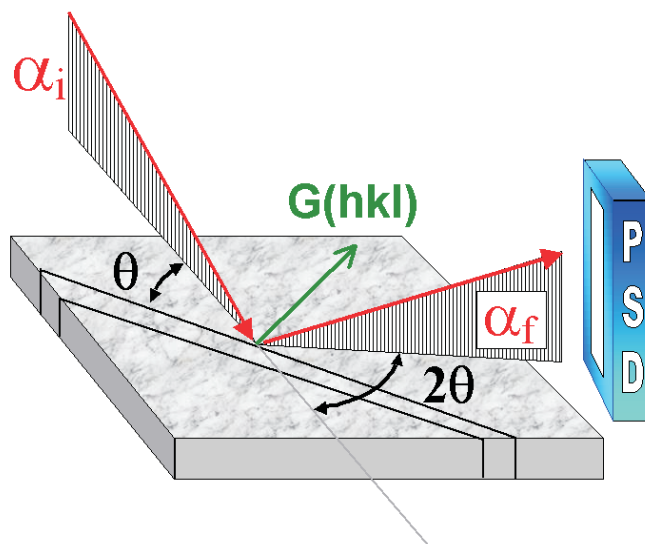
Figure 3.10: The grazing incidence diffraction geometry (GID). The incident and exit angles α_i and α_f are chosen close to the critical angle of total external reflection. The α_f spectra are recorded with the PSD, which is mounted perpendicular to the sample surface.

Scans along the reciprocal lattice vector G(hkl) are performed by turning the sample around its surface normal by an angle θ and the detector arm supporting the PSD by 2θ around the same axis. These scans are called *radial scans* as they cross a Bragg reflection on the radial path that points from the origin to the Bragg point. The momentum transfer achieved in radial direction in such a scan is given by

$$Q_{rad} = |\vec{k}_f - \vec{k}_i| = 2|k|\sin\frac{2\theta}{2} = \frac{4\pi\sin\frac{2\theta}{2}}{\lambda}. \tag{3.2}$$

Where $\vec{k}_{i,f}$ represent incident- and exit wave vectors, λ is the x-ray wavelength. The *angular scan* or *rocking scan* considers a simple rotation of the sample around its surface normal at a fixed detector angle 2θ. If we define $\Delta\theta$ as the deviation of the sample rotation θ from the double-angle-condition $\theta = \frac{2\theta}{2}$, we can write for the angular momentum transfer:

$$q_{ang} = \frac{4\pi\sin\frac{2\theta}{2}}{\lambda}\sin\Delta\theta \approx Q_{rad}\Delta\theta \tag{3.3}$$

With the definitions in eqs. (3.2) and (3.3), Q_{rad} and q_{ang} are perpendicular directions in reciprocal space.

3.3.2 Coplanar diffraction and reciprocal space mapping

The disadvantage of the GID geometry as discussed above is the limitation to in-plane Bragg reflections. For the analysis of strain, it is often required to record information about the relation between in-plane and out-of plane distortion of the crystal lattice. A general way to achieve this is to measure asymmetric reflections *i. e.* reflections which are neither out-of-plane nor in-plane reflections. When using a linear detector, the *coplanar* geometry offers a variety of advantages. In this setup, $\vec{k}_i$, $\vec{k}_f$ and the surface normal lie in the scattering plane. If the PSD is mounted to lie in same plane a single scan records a flat 2D-reciprocal space map in the $Q_x - Q_z$ scattering plane. Q_z is defined as the direction in reciprocal space perpendicular to the sample surface, Q_x is the in-plane direction defined by the azimuth of the chosen asymmetric reflection. As the PSD is elongated in the direction of the scattering angle 2θ every point in the detector can be attributed to a well defined scattering angle. Together with the sample angle θ (which is generally not half of the detector angle 2θ in this geometry) for every "point" in a scan, the PSD spectra can be evaluated as a curved line in reciprocal space. In coplanar geometry all these curved lines lie in one plane and therefore a 2D $Q_x - Q_z$ map can be recorded. The ratio between the in-plane lattice parameter derived from Q_x and the out-of-plane lattice parameter derived from Q_z contains the

valuable information about the strain state as explained in section 2.4.1. The geometry is mapped in Fig. 3.11.
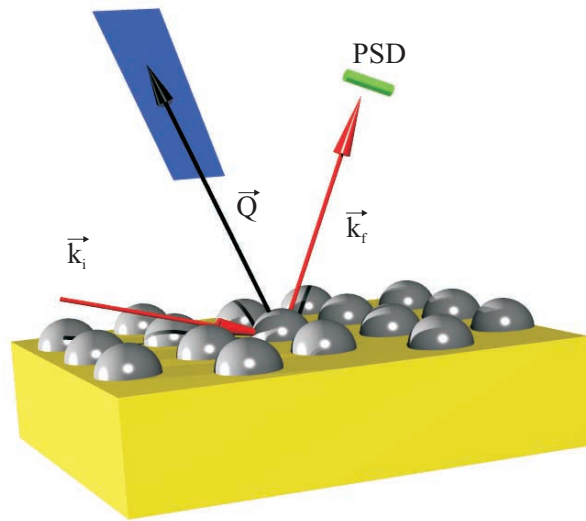

Figure 3.11: The coplanar diffraction geometry for an asymmetric Bragg peak with the use of a PSD (green tube) mounted in 2θ direction. The blue area is mapped while recording PSD spectra during a radial scan.

Incident and exit beams are drawn as red arrows, the momentum transfer $\vec{Q}$ as a black arrow. The PSD is sketched as the green tube mounted along the 2θ direction. The blue area around the Bragg point indicates the 2D region in reciprocal space that is mapped out during a radial scan.

3.4 Calibration and preparation of an anomalous scattering experiment

3.4.1 Measurement of the anomalous corrections f' and f"

As described in section 2.5.1 the Kramers-Kronig relations can be exploited for the precise determination of f' and f". Experimentally, integration boundaries of the form $\int_0^\infty$ have to be avoided. The structure of equation 2.26 shows that we can accept reaching "infinity" on the energy axis, as soon as the area under the remaining tail for f" can be neglected. Additionally, we see from the denominator, that we are especially sensitive to a more detailed structure of f" in the energy regime where we want a precise information about f'. As these energy regimes are usually the edges, it is recommended to measure f" (*e.g.* via the fluorescence yield) across the absorption edge that we want to use in our experiment. The recorded data are fitted into tabulated values for f" and replace the more crude theoretical evolution of f" across the edge (There are numerous references where f' and f" are tabulated. Most of them are based on self consistent solutions for many electron problems). This data table for f" is then numerically integrated up to energies well above the K-edge in order to fulfill the infinity criterion. A cut-off error due to the neglect of small f" values for higher energies results in a vertical shift of the f' curve. Examples of f' from Ge as calculated from Eq. (2.26) in the vicinity of the K-edge for various cutoff energies of 1.5, 2, 3 and 4 times the K-edge energy of Ge are plotted in Fig. 3.12. As a rule of thumb we can say that the integration should be carried out at least up to 3 times the K-edge energy at 11103 eV.
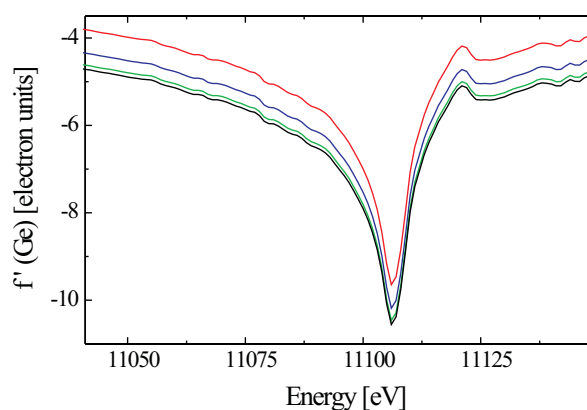
Figure 3.12: Influence of the integration limit on the Kramers Kronig integral and the calculation of f'. f' as derived from f" and Eq. (2.26) is plotted for various integration ranges of f". The high energy cutoff limits for f" were chosen at 16500 eV(red line), 22000 eV (blue) 33000 eV (green), and 44000 eV (black).

3.4.2 Influence of the momentum transfer on f_0

To enhance the anomalous effects, high momentum transfers can help to reduce $f_0(Q)$ and thus pronounce the change in f'(E) with the energy. If we are only treating the change in the scattering from one element, as it will be done in the case of a SiGe alloy in this work, it is recommended to perform a verification of the validity, in particular of the influence of $f_0(Q)$. This can be done using an elemental crystal. It should be mentioned, however, that besides being pure enough, the crystal also has to be a *kinematic* scatterer.

For Ge we used a 20 nm thick film grown on Si via MBE at 150°C, to prevent interdiffusion. At this temperature, the crystal quality is very bad, but we achieve an ideally imperfect crystal with a high mosaicity. The fluorescence yield across the Ge K-edge was measured from this film in order to determine the anomalous corrections. The derived real and imaginary part, together with the momentum $|f_{Ge}|$ corresponding to the momentum transfer at the (004) and the (008) reflection of Ge is shown in Fig. 3.13. The momentum dependence of f_0 causes a shift of the minimum position of $|f_{Ge}|$ to lower energies at the (008) momentum. The location of the Ge K-edge is marked by perpendicular red lines at 11103.5 eV, The calculated minimum for $|f_{Ge}|$ is marked by black lines. It shifts from 11103.0 eV at the (004) momentum in (a) to 11102.0 eV at the (008) momentum in (b).
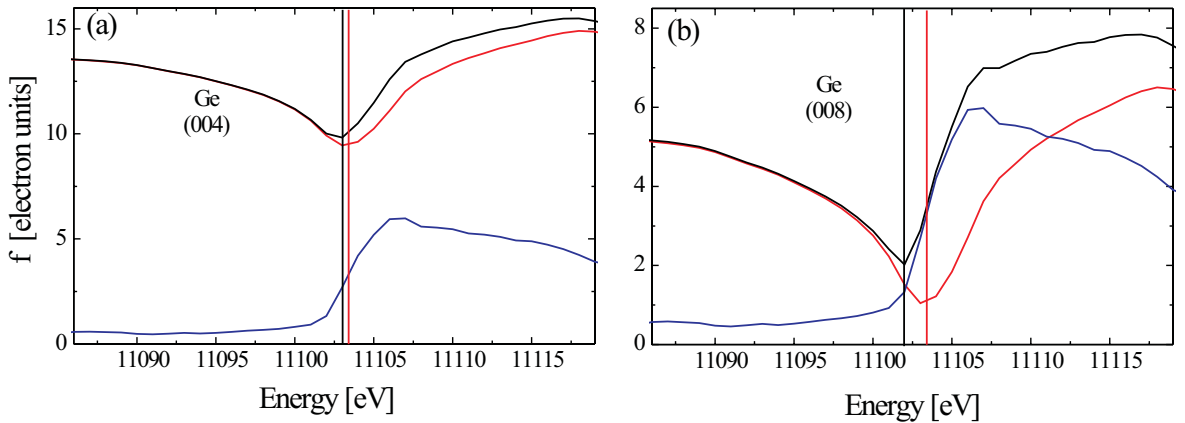
Figure 3.13: Real (red line) and imaginary (blue) part and $|f_{Ge}|$ (black) in the vicinity of the Ge K-edge. (a): The momentum dependence of f_0 is calculated for the Ge (004) reflection. (b): Values corresponding to the (008) momentum transfer. In both graphs, perpendicular red lines mark the Ge K-edge 11103.5 eV, black lines the minimum of $|f_{Ge}|$. Note that the minimum in $|f_{Ge}|$ is expected to shift between the two momentum values by about 1 eV (see text).

Across the Ge K-edge, the Bragg intensities of the symmetric reflections (004) and (008) were recorded. In Figs. 3.14 (a) and (b) the measured intensities (crosses) are plotted together with the calculated curves (the latter require the measured f" and the calculated f' input). The agreement gives confidence in the method, but also allows us to choose a reasonable energy close to the edge where the anomalous effect is strong, but still the changes due to energy fluctuations are small. It appears that it is better to avoid the exact edge and stay some electronvolts below. Due to the very low real part at the (008), the steep rise in f" at the edge dominates the intensity evolution across the edge and therefore shifts the intensity dip by -1 eV with respect to the (004) reflection (Of course this must be true, as the intensity probes $|f|^2$ and not $re(f)^2$). Figure 3.14 (c) shows a plot of the intensity ratio between the intensity recorded at 11040 eV and all other points for both reflections. Again the calculated values are drawn as full lines and show a good agreement between theory and experiment.
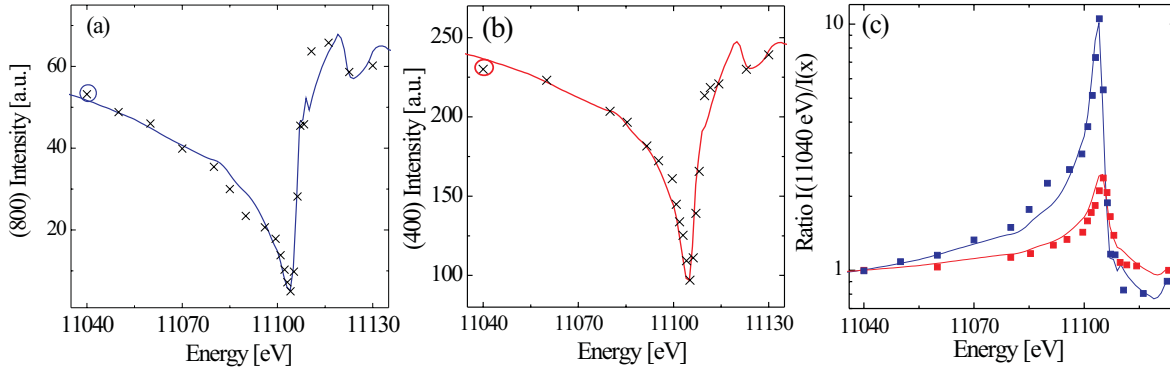
Figure 3.14: Calibration of the diffracted Ge (008) and (004) intensities from a Ge (001) film across the Ge K-edge. (a): Recorded (008) intensity (crosses) together with the calculated intensity (full line). (b): The same data as in (a) but for the (004) reflection. (c): Measured (squares) and calculated (lines) anomalous intensity ratio between the intensity recorded at 11040 eV and the diffracted intensities of all other points for the (008) (blue) and the (004) (red).

3.4.3 Exploitation of the momentum dependency of f_0 in a SiGe alloy

In the case of a (generally disordered) SiGe alloy, the scattering factor can be averaged in the form

$$f_{SiGe} = x f_{Ge} + (1 - x) f_{Si} \tag{3.4}$$

with x as the Ge content. As Ge with 32 electrons is a much stronger x-ray scatterer than silicon with 14 electrons, the sensitivity for the Ge concentration in an anomalous diffraction experiment will be poor if we stay at low momentum transfers. The strategy

in such a measurement is to choose two energies in the vicinity of the Ge K-edge and to calculate the Ge content from the ratio of the recorded intensities. As shown in Fig. 3.14, this ratio rises for high momentum transfers. Thus the anomalous scattering effects can be enhanced considerably by measuring Bragg reflections for high momentum transfers, and hence improve the sensitivity for the composition in the SiGe system. Figure 3.15(a) shows the momentum dependence of the real parts of the scattering factors for Ge and Si at two energies E_1=11040 eV and E_2=11102 eV. The momentum dependent behaviour of $f_0(Q)$ of Ge and Si was calculated with a code based on the parameters derived by Monte-Carlo-simulations in [27]. At these x-ray energies, the corrections f' and f" can be neglected for Si. It is clear that for high Q the Si scattering becomes more pronounced and even larger with respect to the Ge scattering. In Fig. 3.15(b), the intensity ratios for pure Ge, $Si_{0.1}Ge_{0.9}$ and $Si_{0.3}Ge_{0.7}$ are plotted against the momentum transfer Q. The positions of some reflections that are accessible at the Ge K-edge are indicated (as perpendicular lines). This clearly illustrates the necessity of measuring high index reflections in order to improve the resolution of the composition in these alloys.
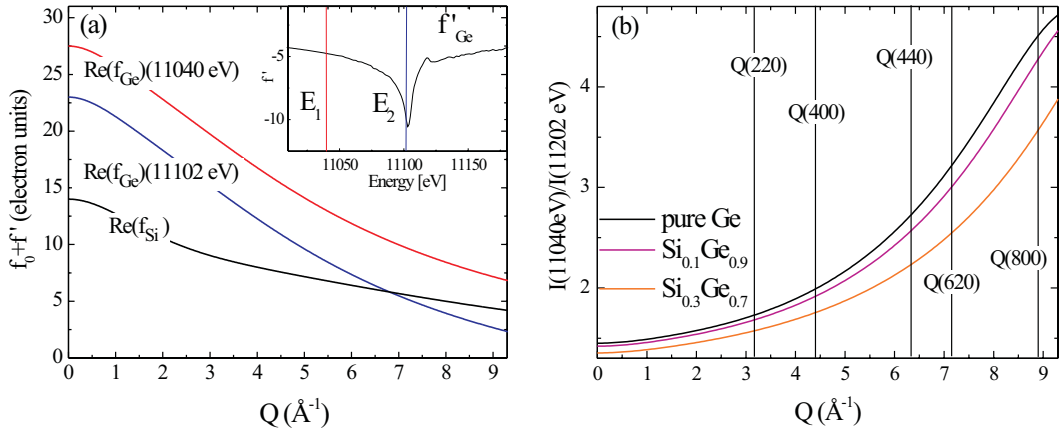
Figure 3.15: (a): Momentum dependent real part of the scattering factor for Ge at E_1=11040 eV (red line), Ge at E_2=11102 eV (blue) and Si (black). (b): Theoretical momentum dependence of the ratio of the diffracted intensities at E_1=11040 eV and E_2=11102 eV for pure Ge (black line), $Si_{0.1}Ge_{0.9}$ (magenta) and $Si_{0.3}Ge_{0.7}$ (orange). Perpendicular lines mark the positions of the probed in-plane reflections.

3.4.4 Calibration of the superstructure suppression in compounds

As explained in section 2.5.1, compound crystals offer the opportunity to almost completely suppress superstructure reflections via anomalous diffraction. The expected intensity minimum can be calculated, following the determination of the anomalous

corrections using the strategy described earlier. Additionally, it is recommended to verify the exact location of the minimum on the eV scale. In the case of intersection points between two scattering factors, small errors in the knowledge of the parameters $f_0(Q)$, $f'(Q)$ and $f''(Q)$ can lead to a considerable deviation of the intensity minimum from the theoretical value. In this work, the superstructure effect was exploited in lead and europium chalcogenides that crystallize in the rock salt structure. As discussed in section 2.5.1, in this lattice, all (hkl) Bragg reflections with h,k and l being odd numbers are superstructure reflections. Their structure amplitudes F_{hkl} then read $F_{hkl_{PbTe}} = f_{Pb} - f_{Te}$. A similar expression holds for the other investigated compounds PbSe, EuSe and EuTe. After calculating the location of the energy of the minimum intensity, the calibration experiment was performed. The diffracted intensity from a *kinematic* scatterer was measured for various energies across the minimum. The *kinematic* scatterer should in addition consist of a small enough volume to neglect the change in absorption when the edge is crossed during the experiment. For the momentum transfer in the vicinity of the (111) reflection of the lead salts, the real parts of the scattering factors for Pb, Eu, Te and Se are plotted in Fig. 3.16(a), together with a magnification of the low energy part in (b).
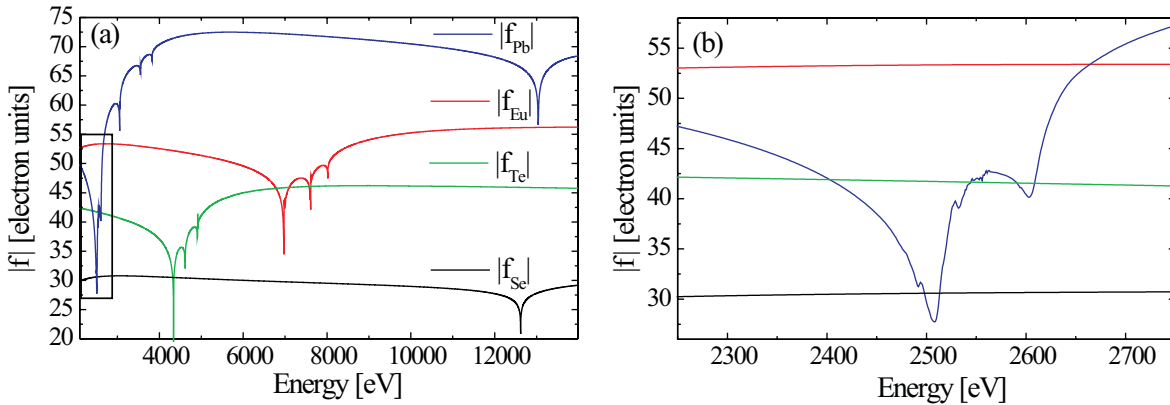
Figure 3.16: (a): Modules of the atomic scattering factors $| f_{Pb} |$ (blue line), $| f_{Eu} |$ (red), $| f_{Te} |$ (green), and $| f_{Se} |$ (black). (b):Magnification of the energy regime around the Pb M_V/M_{IV}-edges (marked by the frame in (a)).

The scattering factor of Pb was calculated via Eq. 2.26 from recorded fluorescence data in the vicinity of the M_V-edge and tabulated values for higher energies. The same was performed for the Eu scattering factor in the vicinity of the L_{III}/L_{II}-edges. It is visible from Fig. 3.16, that the EuTe and EuSe superstructure reflections will have minima close to the Eu L_{III}-edge, whereas PbTe and PbSe have the most pronounced suppression of the superstructure intensity in the vicinity of the Pb M_V-edge. As the

intersection points of the real parts usually determine the location of the minimum for the superstructure reflection, it becomes clear that the energy at the intensity minimum is different for PbTe, PbSe and PbSeTe alloys.

In our experiments, epilayers of the corresponding material were used as calibration samples. The behaviour in the vicinity of the Pb M-edge was of particular interest, as this energy regime is rather unusual in diffraction. Therefore only limited knowledge about the structure of this edge was accessible from the existing literature. In addition, the tabulated values for the scattering factor of Pb in the vicinity of the edge, as well as the tabulated 3d ionization energies vary between the different accessible tables (as *e.g.* [65],[25]). Therefore we not only measured the scattering factors in this energy regime, but also verified the location for the (111) superstructure diffraction minima for the binary and ternary compounds PbSe, PbTe, and $Pb_{0.92}Eu_{0.08}Te$. These calibrations, together with the calculated curves are presented in Fig. 3.17(a). The corresponding minima for EuSe and EuTe in the vicinity of the Eu L_{III}-edge as calculated are plotted in (b).
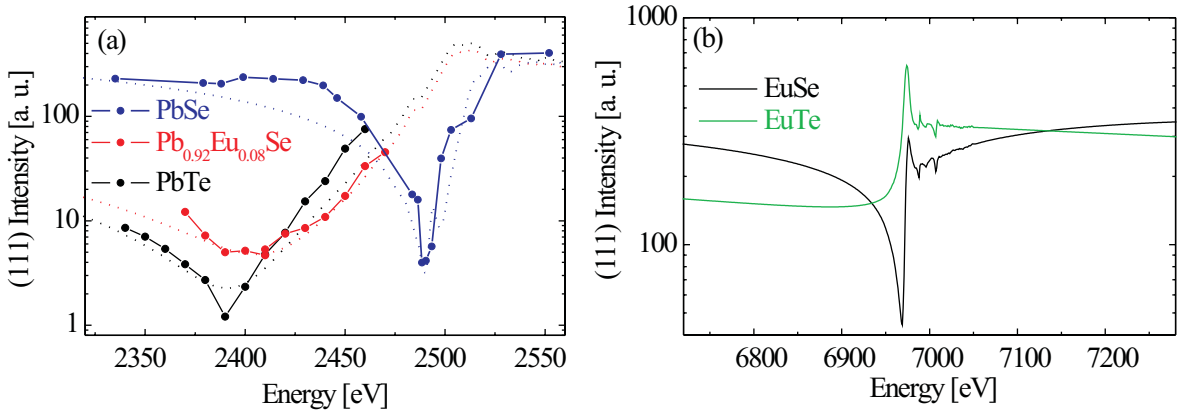
Figure 3.17: (a):(111) diffraction minima as calculated (dotted lines) and measured (connected dots) for PbSe (blue), PbTe (black), and $Pb_{0.92}Eu_{0.08}Te$ (red). (b):(111) diffraction minima close to the Eu L_{III}-edge for EuSe (black) and EuTe (green).

3.5 Anomalous diffraction from lead/europium chalcogenide multilayers

In this section, the anomalous diffraction from superstructure reflection will be demonstrated and exploited in the characterization of 2D $EuSe/PbSe_{1-x}Te_x$ multilayers. All investigated samples of this kind are presented in Table I.

Sample	T (°C)	d_{EuSe} (ML)	$d_{PbSe_{1-x}Te_x}$ (ML)	$EuSe/PbSe_{1-x}Te_x$ layers	x
M1420	380	10	18	30	0
M1553	230	12	120	100	0
M1555	260	10	80	100	0.2

Table I: Growth parameters of the investigated multilayers. The thicknesses of the epilayers as deposited in the MBE process are given in atomic monolayers (ML). In addition, the number of epitaxial bilayers and the Te content x in the $PbSe_{1-x}Te_x$ are given. All samples were grown by R. T. Lechner at the institute for semiconductor physics in Linz.

3.5.1 Comparison of the long wavelength diffraction with standard crystallography

Reflectivity and (symmetric) diffraction are established methods of choice in the characterization of multilayers. From the advantages discussed in sections 2.5.1 and 3.4.4 it becomes clear that for particular conditions it is worth also employing anomalous or resonant scattering at superstructure reflections in order to discriminate between materials. In our system of lead/europium chalcogenide multilayers, the use of the strong 3d-resonance at the Pb M_V-edge will supply the only tool to have a reasonable sensitivity for the lattice parameter in the europium chalcogenides. The first investigated sample, M1420, is a multilayer, consisting of 30 bilayers of 18 atomic monolayers (ML) PbSe (about 64 Å) and 10 ML EuSe (about 36 Å), grown on a 2 μm thick PbSe buffer on a BaF_2 substrate. The quantity of PbSe is larger in order to impose pseudomorphic stress on the EuSe. At conventional x-ray energies around 10000 eV, PbSe will dominate the scattering as it contains the heaviest component Pb and is, in addition, represented by more scatterers. At an x-ray energy of 2490 eV, however, we expect the PbSe (111) reflection to scatter a factor of 200 weaker than the EuSe (111) reflection. The anomalous diffraction experiment was performed on the beamline ID01 at the ESRF in Grenoble. High resolution line scans across the symmetric (111) reflection

were performed at 2490 eV and at 12300 eV (to represent "usual" crystallography conditions). These scans are presented in Fig. 3.18. Even without a quantitative treatment of the enhanced material sensitivity, a dramatic difference in the quality of the data is visible. In both scans, we can see 6 superlattice satellite peaks modulating the Bragg reflection. In the 2490 eV case, however, we can see 28 side oscillations, originating from the well defined number of 30 interfering bilayers. This compares to the side maxima from the grating interference function in optics: for N slits in a grating one observes N-2 side maxima ([15]). The reason why we see these has nothing to do with our resonant effects, but originates from the much longer coherence length of the long wavelength. With a relative energy resolution of a Si(111) monochromator of $\frac{\Delta E}{E} = 10^{-4}$ Looking back to section 2.1.1 at Eq. (2.2), the longitudinal coherence lengths for both energies can be estimated to be 0.5 μm for 12300 eV and 2.5 μm for 2490 eV. We therefore can state that in the 12300 eV case, the coherence properties of the beam defined the size of the coherently diffracting region, which is smaller than the total thickness of the multilayer. At 2490 eV, the 30 bilayers are coherently illuminated (at least perpendicular to their stacking direction) and therefore we can observe the complete interference pattern. From the 12300 eV data we could not state whether the sample quality would not allow those fringes to be seen or whether it is only our limited experimental setup that does not allow us to measure them.
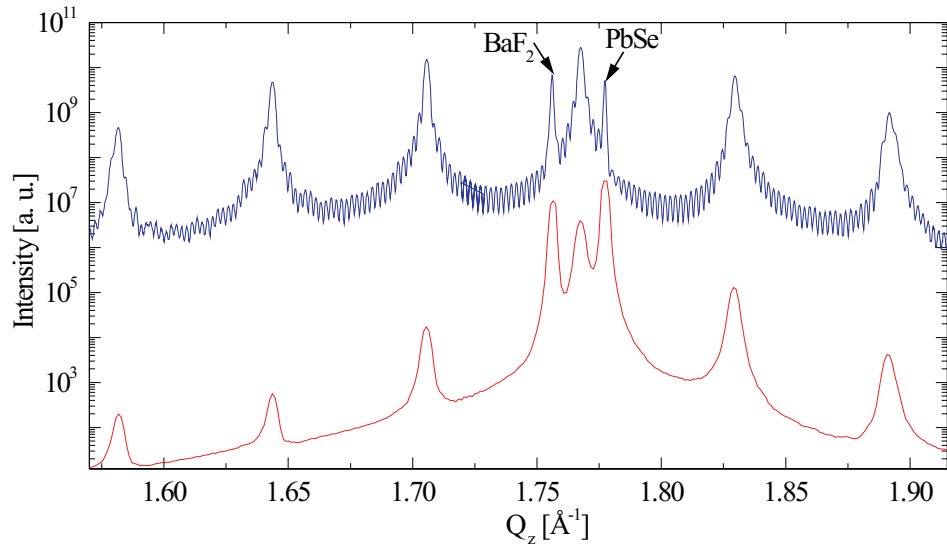
Figure 3.18: Radial scans across the (111) reflection of sample M1420, an EuSe/PbSe 30x multilayer at 2490 eV (blue line) and 12300 eV (red line). The scans are shifted with respect to each other for clarity.

It should be mentioned, that we still can increase our resolution in the 12300 eV case

by collimation. As the coherence *volume* is affected by the longitudinal and transverse coherence length, we can sensitively influence the latter by collimation. This would in principle allow us to compensate for the shorter wavelength and therefore even increase the visibility of the interference pattern for 12300 eV. The remaining intensity will be significantly reduced, however, making the low energy diffraction more suitable for the characterization of these highly perfect samples. Despite these resolution effects, we note that at 2490 eV the PbSe buffer peak to the right of the central superlattice peak is less dominant due to its anomalous suppression. Even the BaF_2 substrate reflection and its thermal diffuse scattering tail is much less disturbing, due to the increased absorption of the low energy x-rays in the PbSe buffer and in the multilayer.

Due to the obviously high perfection of the sample, it appears reasonable to simulate the measurement with the solution of a perfect multilayer derived in section 2.5.4. These simulations where performed for both energies and convoluted with the resolution function for the measurement. The latter could be extratced from the width of the BaF_2 substrate Bragg reflection, that can be considered as a perfect crystal. They are plotted as red lines on top of the data (blue lines) in Fig. 3.19.
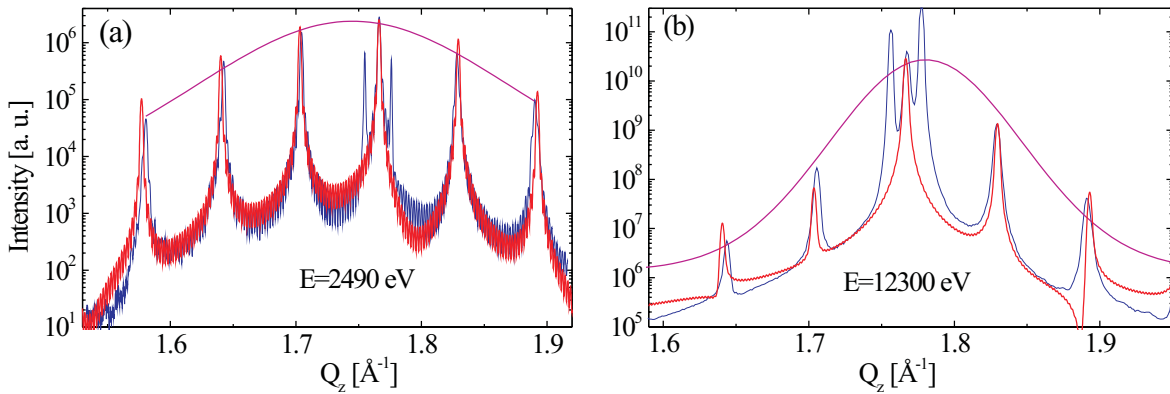
Figure 3.19: Radial scans across the (111) reflection of M1420 as in Fig. 3.18 (blue lines) together with convoluted simulations of a perfect multilayer (red lines) for 2490 eV (a) and 12300 eV (b). The magenta curves are fits to the envelope functions of the superlattice peaks.

Before coming to the indirect evaluation methods that are applied by fitting a model to the data, we can try to directly exploit the material selectivity of the anomalous method. As the envelope function of the superlattice peaks corresponds to the line shape for the diffraction of a bilayer, at 2490 eV, the scattering is mainly dominated by the EuSe layers. We can simply assume that the centre of the envelope function corresponds to the reciprocal lattice parameter of EuSe. At the "normal" diffraction

energy of 12300 eV, we assume the same for PbSe. The envelopes as fitted to the superlattice peaks are drawn as magenta curves in the graphs of Fig. 3.19

The centres of the envelope positions lie at 1.74 Å^{-1} for 2490 eV and at 1.78 Å^{-1} for 12300 eV. If we assign these to be the corresponding out-of-plane reciprocal lattice parameters of EuSe and PbSe, this results in a PbSe (111) d-spacing of 3.53 Å and a EuSe (111) d-spacing of 3.61 Å. Translated into a corresponding cubic out-of-plane lattice parameter, this would mean 6.11 Å for PbSe and 6.25 Å for EuSe. It is evident however, that this is a rather crude estimation, especially when we consider the influence of the substrate and the buffer layer in Fig. 3.19 (b) and the low number of superlattice peaks that contribute to this determination. In particular the intensity contribution from substrate and buffer makes the treatment of the data with elaborate fitting models impractical. If we want to be more sensitive to small strain deviations, these two problems have to be solved.

As mentioned in section 3.4.4, we observe a minimum in the EuSe (111) reflection in the vicinity of the Eu L_{III}-edge at 6977 eV. Therefore we can further optimize this method via choosing two complementary energies where we selectively suppress one of the epitaxial components. To avoid strong contributions from the underlying buffer layer and the substrate, it can help to grow a thicker superlattice, and get rid of these contributions by absorption. As in particular we are interested in the tuning of the EuSe lattice constant under epitaxial stress, we can choose the PbSe layers to be significantly thicker than the EuSe ones. This will lead to a closer spacing of the superlattice peaks, leading to a higher sensitivity for the requested envelope function from above. The envelope function in both cases will be the one of the bilayer and not the monolayer of one component. Even if we suggest that we suppress one component, we still have to take it into account as the amplitude never vanishes completely. Interferences between the stronger scattering material and the remaining amplitude from the weaker one can lead to distortions of the envelope and therefore lead to incorrect results if we directly evaluate its position. To estimate the expected effects on the recorded spectra, we can use Eq. 2.47 and simulate the scattering from a PbSe/EuSe bilayer for the two complementary energies. The sample to be considered consists of 100 bilayers of about 122 atomic monolayers PbSe and 13 atomic monolayers EuSe. Simulations for a perfect bilayer as a unit cell of this superlattice are shown for the two considered energies 2490 eV and 6975 eV in Fig. 3.20 (a) and (b). The huge difference in the thicknesses of these two layers causes the difference in the appearance of the spectra at the chosen energies. As the number of PbSe scatterers is about 10 times higher, its coherently scattered intensity is assumed to be 100 times higher, compensating approximately

for the suppression by a factor of 100 that we achieve by lowering the energy to 2490 eV. So the narrow peak in Fig. 3.20 (a) marks the PbSe film and its lattice constant, whereas the broader peak and its Laue oscillations stem from the thin EuSe film.
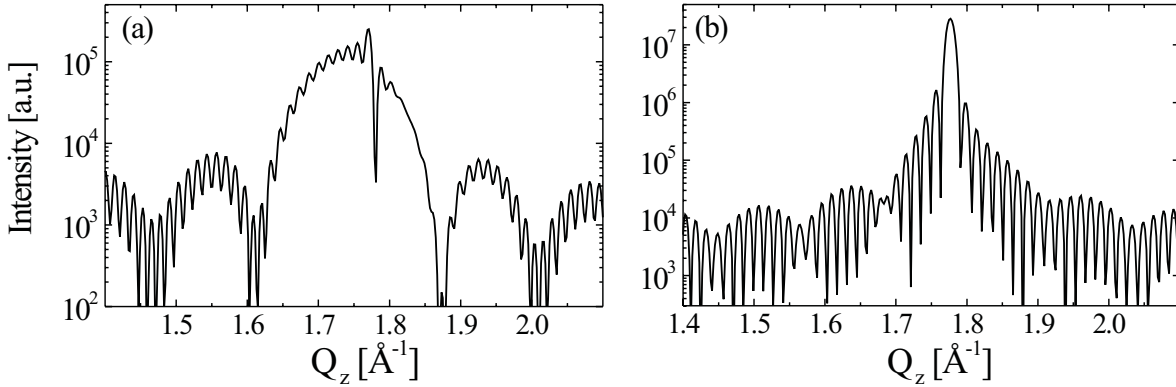

Figure 3.20: Simulation of the specular (111) reflection of a 46Å/430Å EuSe/PbSe bilayer as the expected envelope at 2490 eV (a) and 6975 eV (b). Superlattices have to be measured for these two complementary energies, in order to resolve independently the strain in the PbSe and EuSe.

3.5.2 Diffraction from thick multilayers

The experimental efforts and tools prepared for the anomalous diffraction technique are now applied to thick multilayers. The definition of *thick*, means in this case *infinite*, *i.e.* significantly thicker than the penetration depth of the x-rays in the case of a diffraction experiment. This penetration depth is generally either limited by photo absorption or by extinction (weakening by elastic scattering). The latter can only play a role in the close vicinity of Bragg reflections or in the lower reflectivity regime [40]. In the experiments performed here, the structure amplitude of the Bragg reflections is sufficiently weak to neglect extinction. In the case of absorption however, we have to deal with a peculiarity of the long wavelength: When probing a significant area in reciprocal space, the sample is tilted over a vast angular range. The incident direction of the beam therefore varies, leading to a change in the effective penetration into the multilayer. The situation is sketched in Fig. 3.21 for a reflectivity and diffraction measurement from sample M1553, a 100x{120 ML PbSe/ 10 ML EuSe} superlattice. The measured curve recorded at 2490 eV shows the reflectivity regime and the (111) Bragg reflection at a scattering angle of $2\theta = 88°$. The total thickness of 4.8 μm of the multilayer exceeds the penetration depth of 1.4 μm of the material. The influence of the incident angle on the effective $\frac{1}{e}$ penetration depth into the multilayer changes from *e.g.* 2 EuSe/PbSe bilayers at 15° to 10 at the Bragg angle of 88° and further to

14 at 140°. This effect cancels out partially by the decrease of the illuminated spot on the sample surface that leads to the so called "footprint-correction".
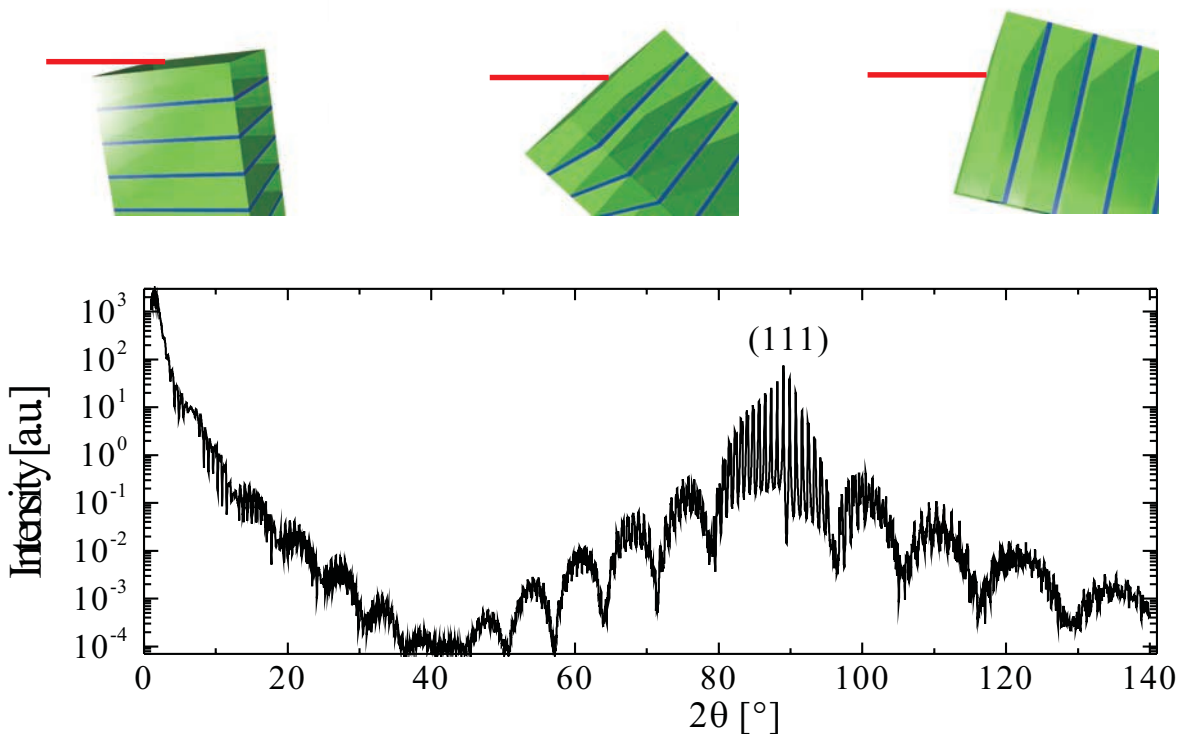

Figure 3.21: Specular scan on sample M1553, a 100x{120 ML PbSe/ 10 ML EuSe} superlattice at 2490 eV. The recorded intensity is plotted in angular space as a function of the scattering angle $2\theta = 88°$ from reflectivity over the (111) Bragg reflection at 88° up to the experimental limit of 140°. The sketch of the multilayer together with the incident beam (red) indicates the importance of the change in the effective probing depth through the scan.

In addition to the corrections required for the large angular region that is probed at the low energies, the atomic scattering factors change through the probed Q-range due to their momentum dependence. All these corrections make the application of our derived analytical solutions to our data impracticable as quantitative fitting models. They might serve for an estimation of the lattice parameters, but are in particular not well suited to take into account structural imperfections. The main structural features we are interested in are strain and interdiffusion. Another structural imperfection that is less important to us, but which crucially influences the diffraction pattern is a drift in the superlattice constant. This occurs due to unstable growth conditions during the MBE process. This drift leads to a loss of phase between the superlattice satellites and

therefore decreases their height in the valleys between the Bragg reflections. As this drift still has only a very small influence on the total thickness ratio in the PbSe/EuSe bilayers, we do not expect it to have an important influence on the structurally more important parameters of strain and interdiffusion. Nevertheless, such a drift has to be included in a model that can be fitted to the experimental data. In the description of these multilayers a numerical model was chosen, simulating the whole multilayer as a 1 dimensional stack of atoms. Interdiffusion at the interfaces was simulated via averaging the atomic scattering factors of the concerned elements in this region. In the same manner their lattice parameters are averaged. As a start for a simulation of the data, one can choose a simplified approach in the treatment of scans like the one shown in Fig. 3.21. If the model is slightly missing the precise thickness of the superlattice constant, the simulated satellites are displaced with respect to the experimental ones and the least squares error becomes very large. This can be avoided via a convolution of the data and the simulation with a Gaussian of the same width. This will flatten the satellites in both cases, therefore being rather insensitive to their small displacement. If these two convoluted spectra are then fitted, the superlattice drift does not play any role. The result of this convoluted fitting to the (111) Bragg reflection from the data of sample M1553 in Fig. 3.21 is plotted in Fig. 3.22.
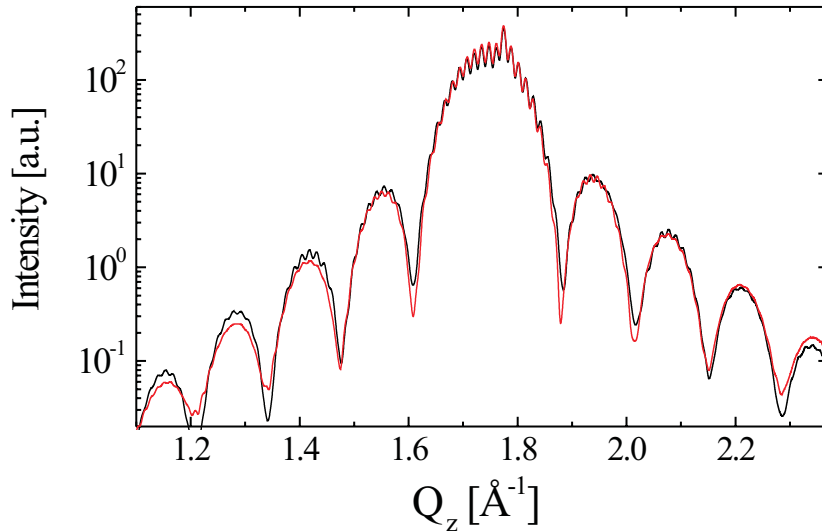
Figure 3.22: Convoluted fit to superlattice M1553 at 2490 eV. The superlattice data as shown in Fig. 3.21 is convoluted with a Gaussian of 0.01 Å^{-1} width and plotted as a black line. The numerical model is convoluted with the same Gaussian (red line), and fitted to the convoluted data.

It should be mentioned, that one parameter of interest in these samples is the distance of the Eu-atoms along the growth direction. We therefore will try to estimate the reliability of the result derived from our fitting procedure. The EuSe(111)-spacing that leads to the fit curve in Fig. 3.22 is 3.597 Å, corresponding to a cubic lattice parameter of 6.230 Å. As the sensitivity to this parameter is the highest at the Bragg point, we might have a closer look to this region. In addition, we can neglect the influence of the superlattice to the diffraction pattern and instead focus onto the central part of the convoluted data shown in Fig. 3.22. Here we have chosen a convolution with a Gaussian of 0.01 Å^{-1} in width. As the width of our EuSe Bragg peak is expected to be $\frac{2\pi}{45} = 0.14$ Å^{-1} we can neglect the influence of the convolution on this peak. The convoluted scan across the (111)-reflection is plotted in Fig. 3.23 (a)-(c) as a black line, together with the best fit in red in (a). The out-of-plane lattice constants corresponding to the measured d-spacings are 6.23 Å for EuSe and 6.123 Å for PbSe.

The sensitivity to the EuSe lattice parameter is demonstrated by simulations: The green line in (b) corresponds to an out-of-plane parameter of 6.20 Å, the blue line in (c) to 6.26 Å. With the cubic equilibrium lattice parameter of 6.187 Å for EuSe and Eq. (2.36), this corresponds to an in-plane lattice constant of 6.13 Å. In the (111) plane, the EuSe therefore is subject to a compressive strain of about 1 %.
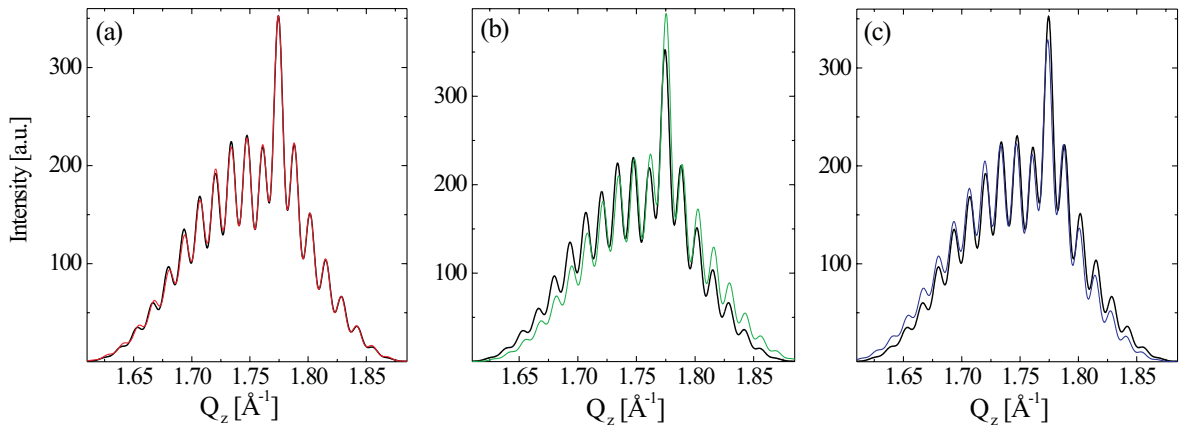
Figure 3.23: Convoluted fit to the centre of Fig. 3.22. The convoluted data recorded from sample M1553 are plotted in black in (a)-(c). The red line in (a) as the best fit represents a EuSe lattice parameter of 6.23 Å along the growth direction. The sensitivity to this parameter is demonstrated via simulations for an EuSe lattice parameter of 6.20 Å ((b), green line) and 6.26 Å ((c), blue line).

The second parameter of interest in these multilayers is the interface quality. Roughness and interdiffusion tend to "wash out" interfaces and mostly affect the intensity on

the truncation rod *i.e.* far away from the Bragg points [67]. In our model we do not discriminate between interdiffusion and roughness on a short lengthscale. The model does take into account however monoatomic steps produced by the cleaving of the substrate. These steps replicate in the highly perfect growth in these structures [68]. The interdiffusion is taken into account as a continuous change of the lattice parameters and the atomic scattering factors from PbSe to EuSe. A possibility to describe such a smooth step is the function

$$c\left(z\right) = \left(1 - e^{\frac{-z}{\mu}}\right)^{\tau}.\tag{3.5}$$

z is the spatial coordinate along the interface normal, μ and τ describe the decay. The atomic scattering factors representing Pb or Eu on the Pb/Eu lattice sites, are then averaged via

$$f_{Eu/Pb} = cf_{Eu} + (1 - c) f_{Pb}.\tag{3.6}$$

An equivalent expression refers to the lattice parameters. The advantage of the function (3.5) is its flexibility to express different forms of decay with only two parameters. For a decay length of $\mu =$ 1.3 Å, various evolutions of Eq. (3.5) are plotted in Fig. 3.24 for $\tau = 0.5$ (black line), $\tau = 5$ (red) and $\tau = 25$ (blue).
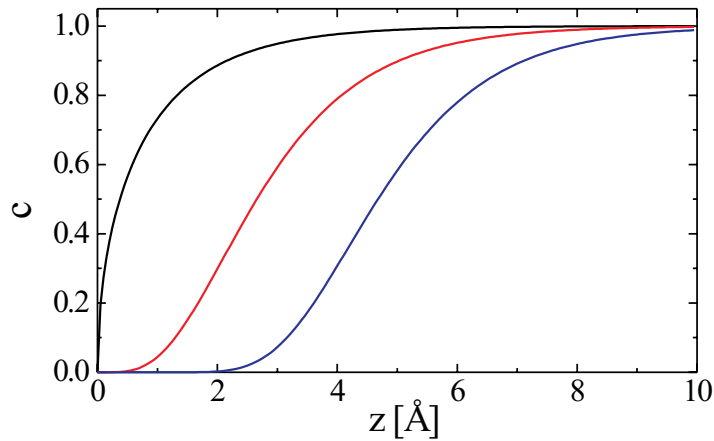
Figure 3.24: Plots for possible interdiffusion evolutions according to Eq. (3.5) for $\mu =$ 1.3 Å: $\tau = 0.5$ (black line), $\tau = 5$ (red), $\tau = 25$ (blue).

With the starting parameters derived by the fit presented in Fig. 3.22, the data recorded at the complementary energies 2490 eV or 6975 eV for either PbSe or EuSe suppression were fitted using a simplex algorithm. The measured and fitted curves for both energies are presented in Fig. 3.25 (a) and (b).
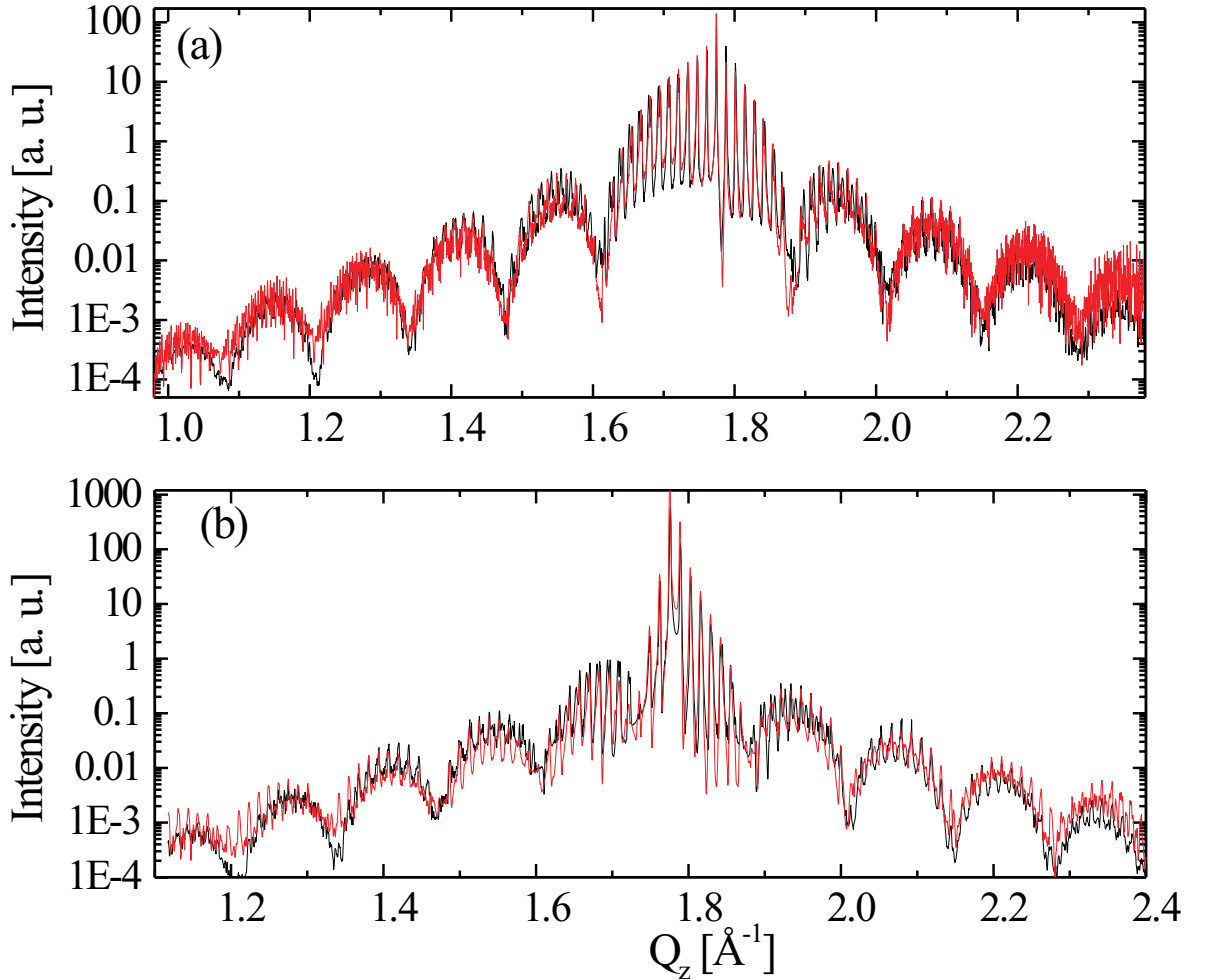
Figure 3.25: Fits to the superlattice diffraction data around the (111) reflection of sample M1553 at 2490 eV (a) and 6975 eV (b). The use of the complementary energies leads to a decoupling of the sensitivity to the out-of-plane lattice parameters of EuSe and PbSe. The fits of the numerical simulation are plotted as a red line on top of the data (black line). The interdiffusion parameters according to Eq. (3.5) are $\mu = 1.0$ Å and $\tau = 8.4$, the lattice parameters along growth direction were determined to be 6.232 Å for EuSe and 6.122 Å for PbSe.

The sensitivity to interdiffusion is expressed by the two simulations in Fig. 3.26(a) and (b). In both graphs the data as in Fig. 3.25 is plotted as a black line together with simulations as red lines. The insets represent the EuSe profile along the growth direction. A value of 1.0 represents pure EuSe, 0.0 represents pure PbSe everything between 0 and 1 corresponds to a mixture of $Eu_xPb_{1-x}Se$ as described in Eq. (3.6). The high sensitivity to interdiffusion is visible on the truncation rod, far away from the Bragg point. We find a steep interdiffusion decay from 25% to 75% EuSe within 1.2 Å at the interface.
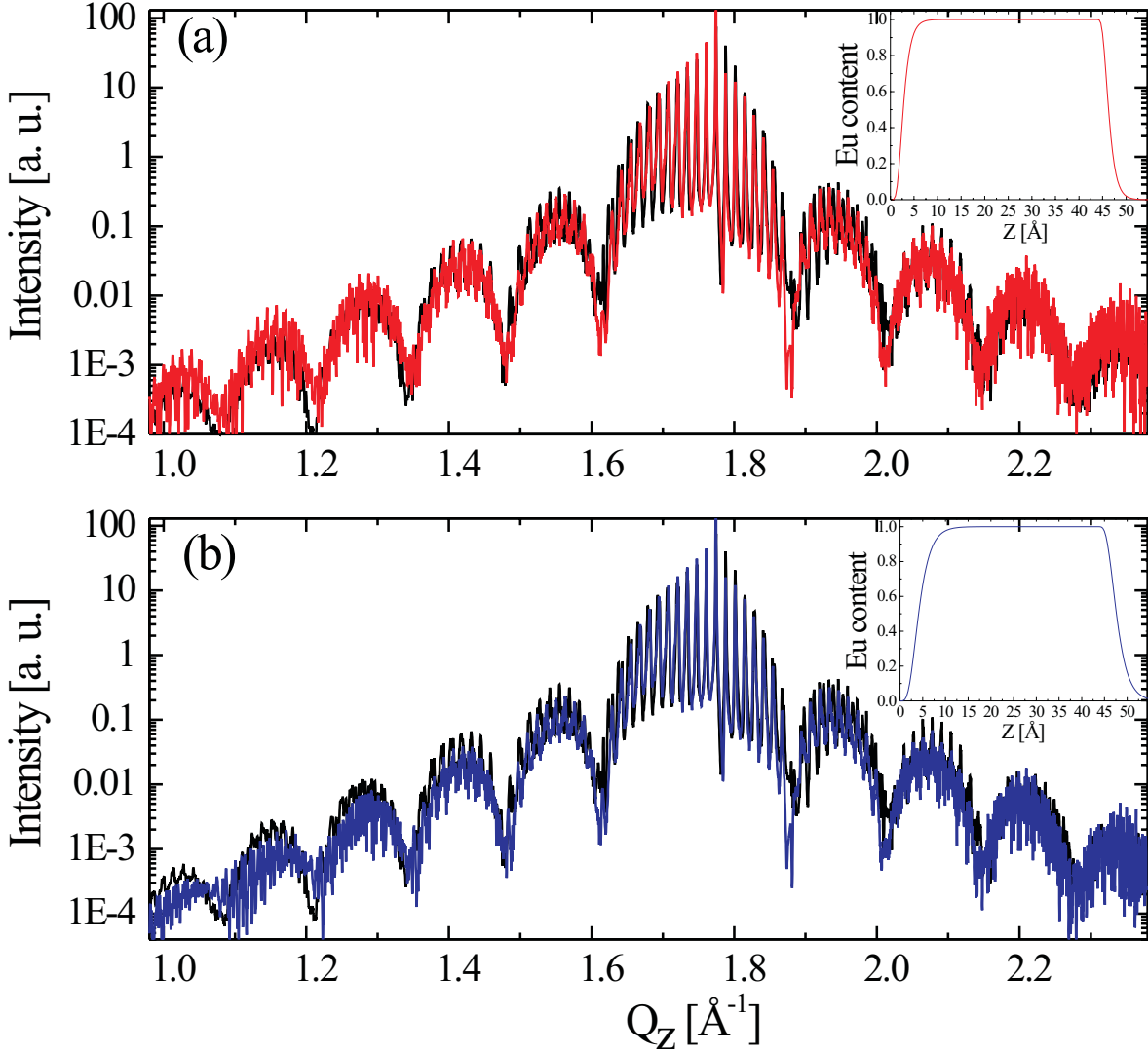
Figure 3.26: Influence of the interdiffusion profile on the scattered intensity. The data recorded for sample M1553 at 2490 eV is drawn as a black line. In (a) and (b), simulations for different interdiffusion profiles are plotted in red and blue. The insets describe the evolution of the EuSe concentration perpendicular to the film plane. Positive z-values indicate the direction of growth. The decay parameter μ from Eq. 3.5 for interdiffusion was chosen to be 1.0 Å in (a) and 1.8 Å in (b).

In order to apply the epitaxial strain from the PbSe to EuSe, the PbSe spacer layers were taken to be about 10 times thicker than the EuSe layers. One can now further tune the strain via a change in the lattice parameter of these spacer layers. This can be done by alloying the PbSe to $PbSe_{1-x}Te_x$. It is not easy, however, to have a precise control over the Te-content that is finally attained in the $PbSe_{1-x}Te_x$ alloy in the epitaxial process. The higher enthalpy of the PbSe compound formation versus the one of PbTe favours the formation of pure PbSe and the vaporization of the unbound

Te. The Te content accepted in the crystal therefore is sensitively influenced by the growth temperature. The choice of this temperature is limited on the other hand by the mobility of the EuSe. A too low growth temperature would not lead to a perfect 2D EuSe film. The amount of Te contained in the crystal lattice is generally measured via the $PbSe_{1-x}Te_x$ lattice parameter. In sample M1555, x was chosen to be 0.2 in order to compensate the lattice mismatch between PbSe and EuSe via alloying of the PbSe with Te. The diffraction experiment was carried out at 2475 eV, to minimize the $PbSe_{1-x}Te_x$ scattering with respect to the EuSe scattering. A scan across the specular (111) reflection of a superlattice with 100 bilayers is shown in Fig. 3.27 as a black line together with a best fit simulation in red. The fit corresponds to a $PbSe_{0.89}Te_{0.11}$ thickness of 290 Å and a EuSe thickness of 44 Å.
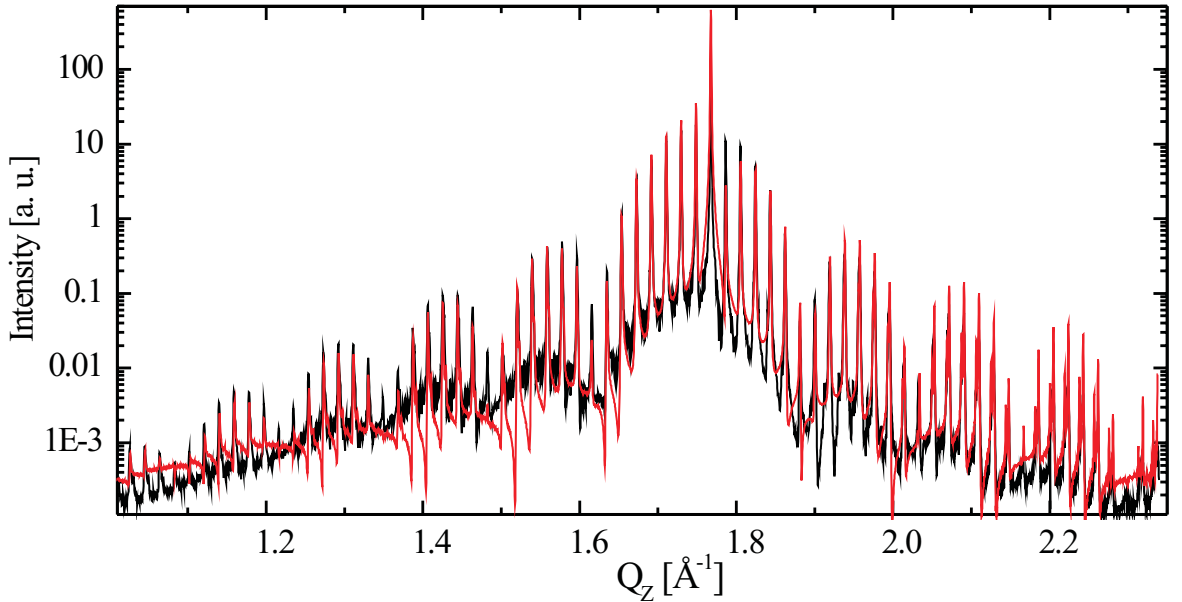
Figure 3.27: Scan across the (111) reflection of sample M1555, a 100x $PbSe_{1-x}Te_x$/EuSe (x=0.11) superlattice recorded at 2475 eV (black line), together with a simulation (red line). The Te content x determined via the $PbSe_{1-x}Te_x$ lattice parameter of 6.148 Å in growth direction. The corresponding EuSe lattice parameter amounts to 6.199 Å. The interdiffsuion decay parameters are μ=0.75 Å and τ=10.4.

In order to be more sensitive to the lattice parameters and hence also the Te content in the $PbSe_{1-x}Te_x$, the central part of the scan in Fig. 3.27 was measured at two complementary energies, 2475 eV and 6965 eV. These scans together with their best fit simulations are shown in Fig. 3.28 (a) (2475 eV) and (b) (6965 eV). The lattice parameters in growth direction that are derived from these are 6.148 Å for $PbSe_{1-x}Te_x$ and 6.199 Å for EuSe. Using the cubic lattice constants of 6.124 Å for PbSe and 6.462

Å for PbTe we can apply Vegard's law and Eq. (2.36) to calculate the in-plane lattice constants and the Te-concentration. The EuSe in-plane lattice constant therefore is 6.169 Å, still being 0.3 % strained with respect to the equilibrium constant of 6.187 Å. The $PbSe_{1-x}Te_x$ cubic lattice constant derived from this in-plane constant and the measured lattice constant in growth direction of 6.148 Å is 6.162 Å. This corresponds to a Te-content of 11 %. Despite the fact that 20 % Te was deposited in the MBE process, the crystallized alloy has the composition $PbSe_{0.89}Te_{0.11}$.
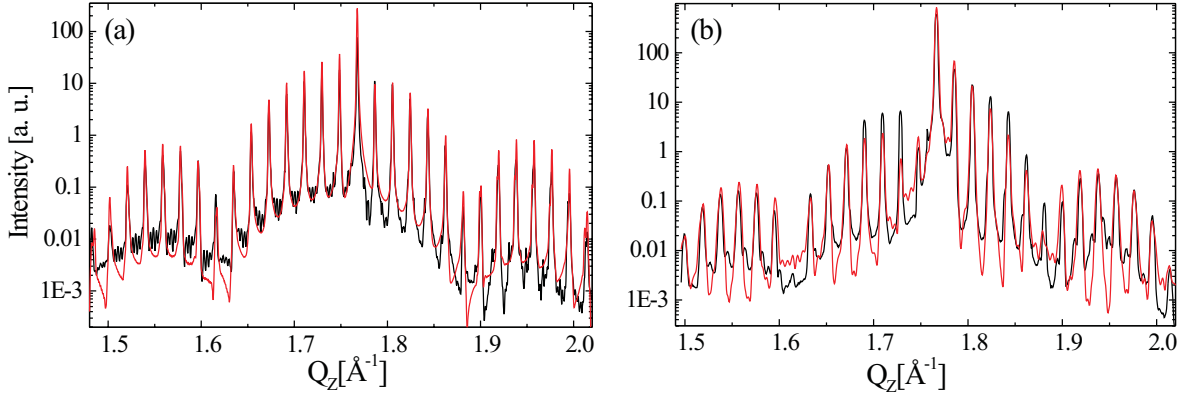
Figure 3.28: (111) reflection of the 100x $PbSe_{.89}Te_{.11}$/EuSe superlattice M1555 at complementary x-ray energies. (a): 2475 eV, $PbSe_{.89}Te_{.11}$ suppression. (b): 6965 eV, EuSe suppression. The best fit simulations are added in both cases as red lines using the same structural parameters for the lattice constants in growth direction. They amount to 6.148 Å for $PbSe_{.89}Te_{.11}$ and 6.199 Å for EuSe.

3.6 Strain and interdiffusion in SiGe islands on Si(001)

3.6.1 Interdiffusion in Ge-islands studied by anomalous diffraction

As explained in sections 3.4.1-3.4.3, anomalous diffraction can be used to determine the composition in a disordered binary alloy. The condition of disorder allows us to state, that the diffracted intensity is proportional to the average atomic scattering factor. The samples studied in this work were SiGe islands on a Si(001) surface. These were obtained via MBE deposition of pure Ge. In Table II, the growth conditions of the investigated samples are listed.

Sample	Growth Temperature (°C)	Deposition (ML)
z1282	600	7
s1901	620	6.7
s1896	650	9.0
s1892	700	11.0
s1919	840	6.0

Table II: Growth temperatures and Ge deposition rates of the investigated SiGe samples. sample z1282 was grown by Z. Zhong at the institute for semiconductor physics in Linz. The remaining samples were grown by M. Stoffel at the Max-Planck-Institute for solid state research in Stuttgart.

It is known that alloying takes place during the island formation and induces a phase transformation of the growth mode from pyramids towards facetted dome-shaped islands above a certain growth temperature. [69, 70, 71, 72, 73]. The first investigated sample of this type is sample z1282 where 7 monolayers of Ge were deposited at a temperature of 600 °C. The phase transformation of the growth mode is found to be below 600 °C [74], therefore domes are obtained in this sample. An atomic fore microscopy (AFM) image of sample z1282 (Fig. 3.29 (a)) shows a mono disperse size distribution of domes. Their base diameter is of the order of 700 Å, their height is about 130 Å. Figure 3.29 (b) shows a line scan from the cross section indicated in (a) as a red line. The scattering geometry of choice to investigate these samples via anomalous scattering is the grazing incidence diffraction technique (GID) described in section 3.3.1. In this geometry only in-plane reflections can be accessed, however it enables us to suppress the thermal diffuse scattering (TDS) from the Si-substrate significantly. As the alloy composition is evaluated from a ratio between two intensities, all background contributions have to be subtracted before. It is evident, that all these corrections in the data treatment introduce errors. It is therefore an advantage to use this technique in order

to keep the background from TDS as low as possible. The sample was illuminated at an incident angle of 0.1 °, which is well below the critical angle at x-ray energies of about 11100 eV.
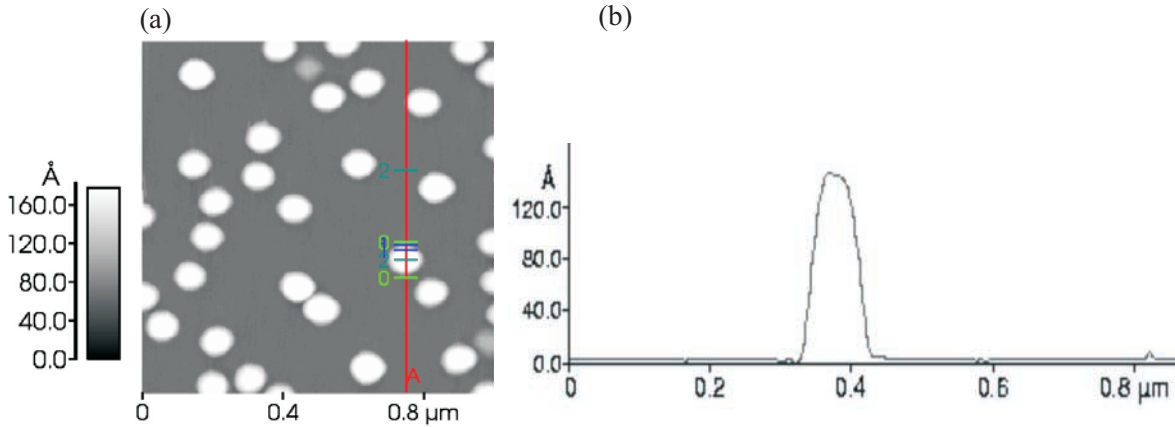

Figure 3.29: (a) Atomic force microscopy of Ge islands on Si(001). (b) AFM line profile as indicated in (a) by the red line.

In order to determine the Ge content in the islands by grazing incidence diffraction, two energies where chosen in the close vicinity of the Ge K-edge and 60 eV below. These two probed energies $E_1=11043$ eV and $E_2=11103$ eV are indicated in the graph in Fig. 3.30 where f'and f" are presented as a function of energy. For a precise determination of the atomic scattering factors, $f"_{Ge}$ was measured via fluorescence and f'_{Ge} was calculated using the Kramers-Kronig dispersion relation as explained in section 3.4.1. To demonstrate the increase of the relative anomalous effect with the momentum transfer, all accessible in-plane reflections where probed. The accessibility was limited by the energy of 11043 eV and the maximum scattering angle of 125°.
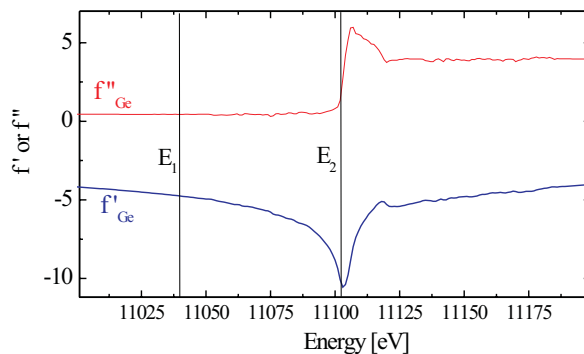
Figure 3.30: Correction terms f'_{Ge} and $f"_{Ge}$ in the vicinity of the Ge K-edge. The two perpendicular lines mark the energies $E_1=11043$ eV and $E_2=11103$ eV at which the anomalous diffraction experiment was performed.

All Bragg reflections as scanned in the radial direction are sketched in Fig. 3.31 (a) together with the recorded data for each reflection. The blue dots correspond to the intensity at E_1=11043 eV, the green dots represent the data at the Ge K-edge at E_2=11103 eV. The strong Si Bragg peak on the right part of each graph is cut off, as we want to focus on a linear scale on the broad intensity distribution caused by the strained SiGe nanocrystals. In Fig. 3.31 (b), perpendicular red lines mark the position corresponding to the relaxed reciprocal lattice spacings of pure Ge and pure Si. The lattice parameter distribution in the nanocrystal is much closer to Si than to the Ge position. This means that either a significant alloying has taken place, or that the islands are highly strained. As expected, the intensity ratio $\frac{I_{E_1}}{I_{E_2}}$ increases considerably for the high index reflections. In addition, the high index reflections allow for a better discrimination of strain and shape. The broadening of a Bragg reflection due to the finite size R amounts to $\frac{2\pi}{R}$ and remains constant in reciprocal space, whereas the strain-induced broadening $\frac{\Delta a}{a}$ increases with Q. Therefore, if the condition

$$\frac{2\pi}{R} < \frac{\Delta a}{a} Q \qquad (3.7)$$

is fulfilled we can extract directly the composition for different lattice parameters with the resolution Δa. To discriminate between two regions with a difference of *e.g.* 0.1 % in lattice parameter would require a size R of about 700 Å of the diffracting object if we probe the region of the Si (800) reflection. Evaluating the intensity ratio for the two energies E_1 and E_2 at a given momentum transfer Q_{rad}, one can now use this direct method on a high indexed reflection, to link composition and lattice parameter without any model assumptions. As the scattering amplitude in Si is virtually the same for both energies, no elaborate normalization of the intensities is necessary. Anomalous diffraction in the SiGe system was exploited independently from this work by Paniago *et al.* [72] however without exploiting high momentum transfers.

Qualitatively, the data as presented in Fig. 3.31 permit already some important statements: At the (440) reflection, a step like feature visible between the maximum of the intensity from the distorted islands and the Si-Bragg position. It gets more pronounced for the reflections (620) and (800). On the right hand side of this step, there is no observable difference in the intensities recorded at E_1 and E_2. We therefore can attribute this step as being the position of the interface between the SiGe island and the substrate of pure Si. As this location is found at a position that is 0.5 % lower than the Si Bragg point, the Si is under a tensile strain of about 0.5 % at the interface to the SiGe island.
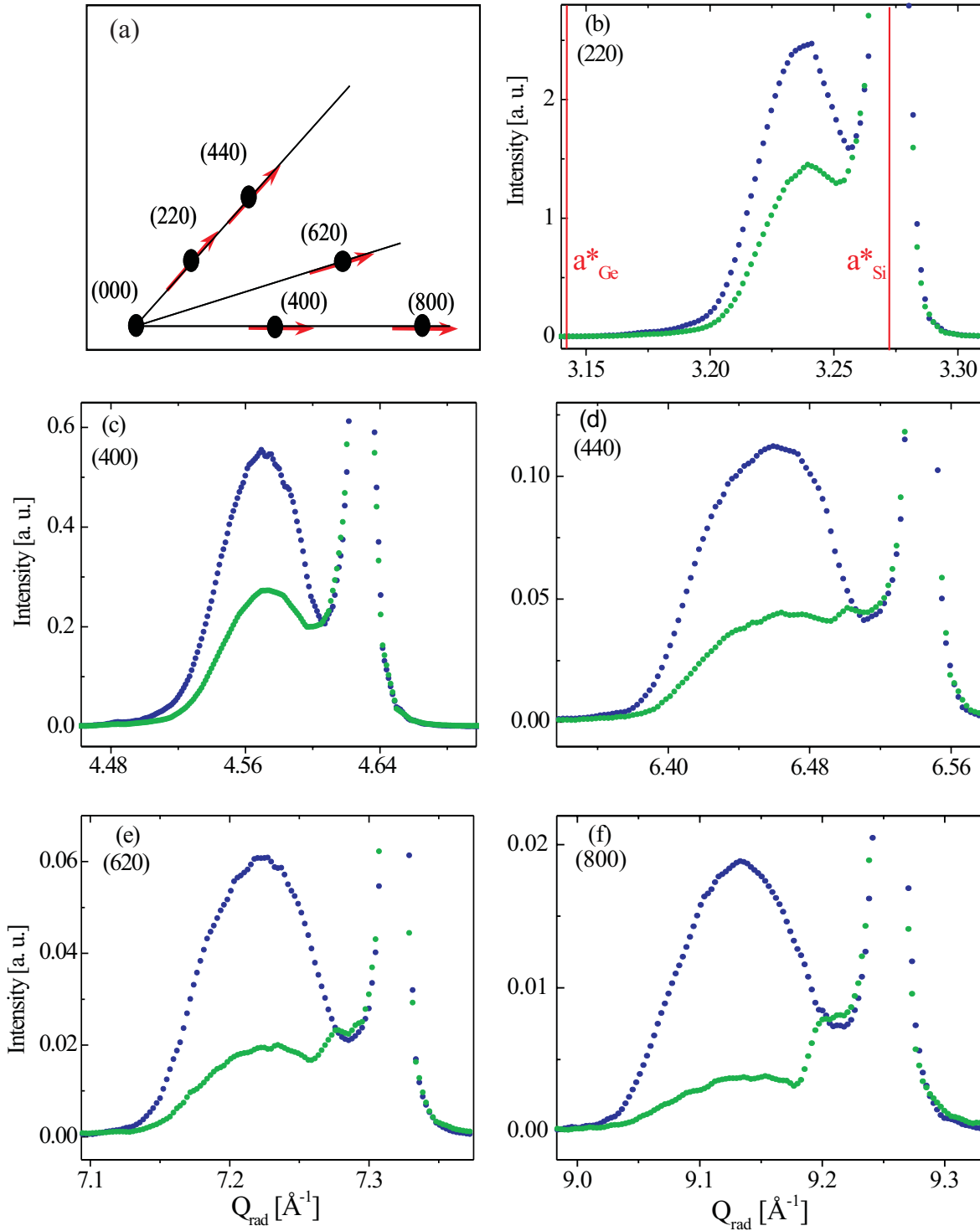
Figure 3.31: All probed in-plane reflections for SiGe islands on Si(001) on sample z1282. (a): Sketch of the radial scans across the in-plane reflections.(b)-(f): Data for all radial scans at E_1=11043 eV (blue dots) and E_2=11103 eV (green dots). The red lines in (b) mark the Bragg points for unstrained Ge and Si.

Considering Eq. (3.7) and the base diameter of about 700 Å of our dots we already derived our lattice parameter resolution to be 0.1 % at the (800) momentum transfer. In Q-space this means that our form factor of the dot base has a width of about 0.01 Å^{-1}. This corresponds to the width of the step in Fig. 3.31 (f). Therefore the steepening of the step for increasing momentum transfer is *purely related to the increase of the resolution.*

Assuming a monotonic relaxation of the lattice parameter for increasing height above the substrate we can state that this rather abrupt change in the Ge concentration is an indication for a perfect interface between the strained Si and the island with a certain SiGe alloy composition. For our further quantitative treatment of the Ge content we will take advantage of the attributes of the high Q-ranges and focus onto the data recorded at the (620) and the (800) reflection. Considering a disordered alloy of $Si_{1-c}Ge_c$, the diffracted intensity at all Bragg reflections is proportional to the square of the average alloy scattering factor $\bar{f}$. The intensity ratio for the two probed energies E_1 and E_2 then reads:

$$\frac{I_{E_1}}{I_{E_2}} = \frac{\bar{f}_{E_1}}{\bar{f}_{E_2}} = \frac{c\left(f_{0_{Ge}}(Q) + f'_{Ge_{E_1}} + if''_{Ge_{E_1}}\right) + (1-c)\left(f_{0_{Si}}(Q) + f'_{Si} + if''_{Si}\right)}{c\left(f_{0_{Ge}}(Q) + f'_{Ge_{E_2}} + if''_{Ge_{E_2}}\right) + (1-c)\left(f_{0_{Si}}(Q) + f'_{Si} + if''_{Si}\right)} \quad (3.8)$$

Except for the Ge content c all quantities in Eq. (3.8) can be calculated or measured before the diffraction experiment. The measured intensity ratio is therefore the parameter which can be unambiguously linked to this Ge content c. The simplest way of the data evaluation is to interpolate a set of scans at two energies, to obtain intensity values at the same positions in reciprocal space. A numerical comparison of the intensity ratios in these points with values which were calculated and tabulated before via Eq. (3.8) then yields the composition as a function of lattice parameter. This evaluated concentration is plotted in Fig. 3.32 as a function of the lattice parameter.

This concentration profile in the space of lattice parameters can also be interpreted as a direct measure of the elastic energy stored in the sample: for any binary composition of $Si_{1-c}Ge_c$, we can define an approximate cubic lattice constant a via the linear interpolation of the lattice parameters of Si and Ge. Using the intensities measured in Fig. 3.31 (b)-(f), we know the relative amount of scattering material in every point in reciprocal space.

If we compare our equilibrium lattice parameter for a certain Ge content c with the lattice parameter for which we determined this compositional parameter c, we can derive the amount of remaining strain. Together with the knowledge about the elastic constants this can be translated into the elastic energy per atom at a certain point in reciprocal space. Applying the weight function of the relative material amount gained through the diffracted intensity, one can define an average elastic energy per atom inside the epitaxial structure. As all nano-structures grown via Stranski-Krastanow growth are metastable systems far from equilibrium, this can be an important parameter in the description and comparison of *e.g.* samples grown at different temperatures.
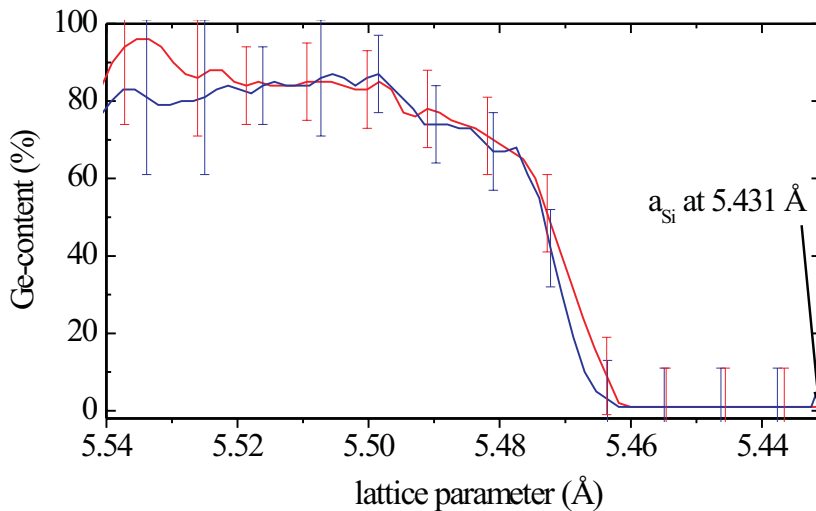
Figure 3.32: Ge concentration in sample z1282 as a function of the lattice parameter. The Ge content was evaluated from the data at the (620) (red line) and (800) (blue) reflection as plotted in Fig. 3.31 (e) and (f).

Another point of interest is the reconstruction of the composition profile in real space. In this particular case we can use a method introduced in [66]: the scans presented in Fig. 3.31 follow the radial path, and the shape and width of the signal from the nano islands is determined mainly by their lattice parameter distribution. Scans carried out in a direction perpendicular to the radial path (here: "angular scans") are therefore scans across the Fourier transform of the shape function of an iso-lattice-parameter area. Note that we already determined the composition for a fixed lattice parameter. Hence a procedure which can link a shape function with a lattice parameter also links shape, in this case lateral size, with the composition. On the radial scan across the (400) reflection 6 positions were chosen at which angular scans were recorded. These scans are presented in Fig. 3.33 (a) and (b). The angular scans show size oscillations, proving the monodispersity of the islands. These size oscillations get narrower for higher Q-

positions *i. e.* when we approach the reciprocal position of Si. This can be attributed to the fact, that the islands have a dome-like shape. The lateral size decreases for the higher parts, which are also the most relaxed ones.
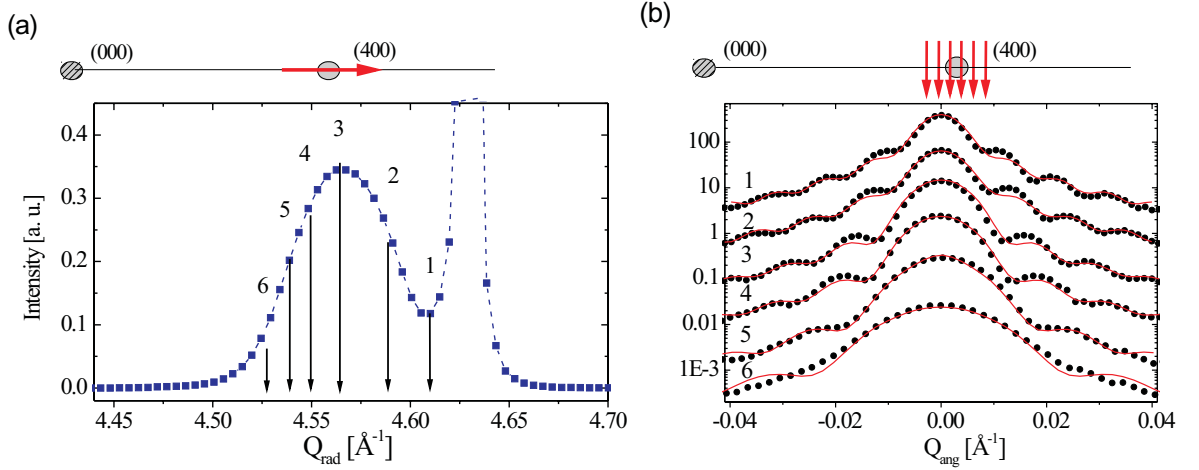

Figure 3.33: In-plane map of the (400) reflection of sample z1282. (a): Radial scan; for the numbered positions angular scans where performed in order to determine the lateral size of a region with common lattice parameter. (b): Angular scans at the 6 positions marked in (a), together with fits (red lines) to determine the shape function.

It is remarkable that size-oscillations are still visible at a radial point that corresponds to a position in lattice parameter space where pure Si is found. The strained parts of the substrate below the islands is also mono disperse and well defined as the islands themselves. The lateral sizes determined by the fits to the oscillations in Fig. 3.33 (b) can be linked with certain heights inside the domes via a comparison with AFM line scans of the dome profiles. In Fig. 3.34 the results obtained through this procedure are presented. The AFM line shape was corrected for the tip size broadening. The lattice parameter relaxation follows a rather continuous evolution whereas a rather abrupt change in the Ge concentration is observed. As still a significant alloying takes place these results rise the question about the interdiffusion process. Interdiffusion through the substrate-island interface would not leave an almost constant composition inside the island and a sharp interface to the pure Si substrate. Note however that no information about lateral variations of the Ge-content can be derived by this method. To gain more information about the nature of this process, a study on a sample series grown at different temperatures will be discussed in the following section.
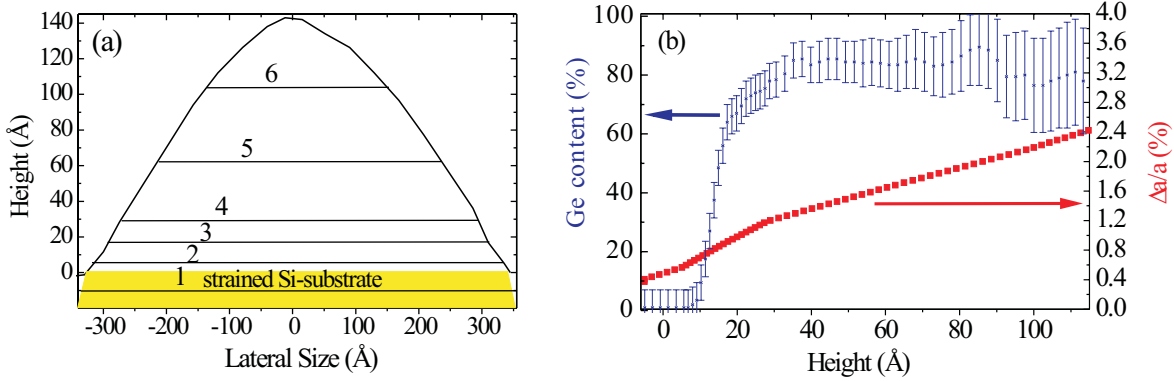
Figure 3.34: Results of the real space reconstruction for sample z1282. (a) The tip size corrected AFM profile is used to attribute a certain height to the lateral sizes determined from the fits in Fig. 3.33 (b). As these lateral sizes correspond to iso lattice parameter areas, they can be used to link directly lattice parameter and composition in (b): Red squares correspond to the lattice parameter evolution with height, whereas the blue curve with error bars describes the composition profile as determined earlier from the (620) and the (800) reflection.

3.6.2 Influence of the growth temperature on strain and interdiffusion

In this section we will extend the example presented previously to a combined study of composition- and strain analysis via anomalous diffraction and reciprocal space mapping. The effect of the growth temperature on the relaxation behaviour and the interdiffusion is studied on a series of dome shaped SiGe islands. The results will be compared to an alternative composition analysis based on a selective etching process. Four samples grown at 620 °C (sample s1901), 650 °C (s1896), 700 °C (s1892) and 840 °C (s1919) were investigated using the anomalous grazing incidence technique at high momentum transfer as described previously. For all samples, the (800) reflection was used to determine the composition in reciprocal space. A pair of radial scans for each sample is plotted in Fig. 3.35 (a)-(d) below the AFM image for the corresponding sample. The calculated concentration profile in reciprocal space is drawn as a black line for each sample. The sample s1901, grown at the lowest temperature shows the flattest evolution and the highest Ge-content. The three samples grown between 620 °C and 700 °C show a trend towards lower Ge content and a more pronounced evolution of the Ge-content with increasing lattice parameter for higher temperatures. Sample S1919 that was grown at 840 °C drops out of this trend.
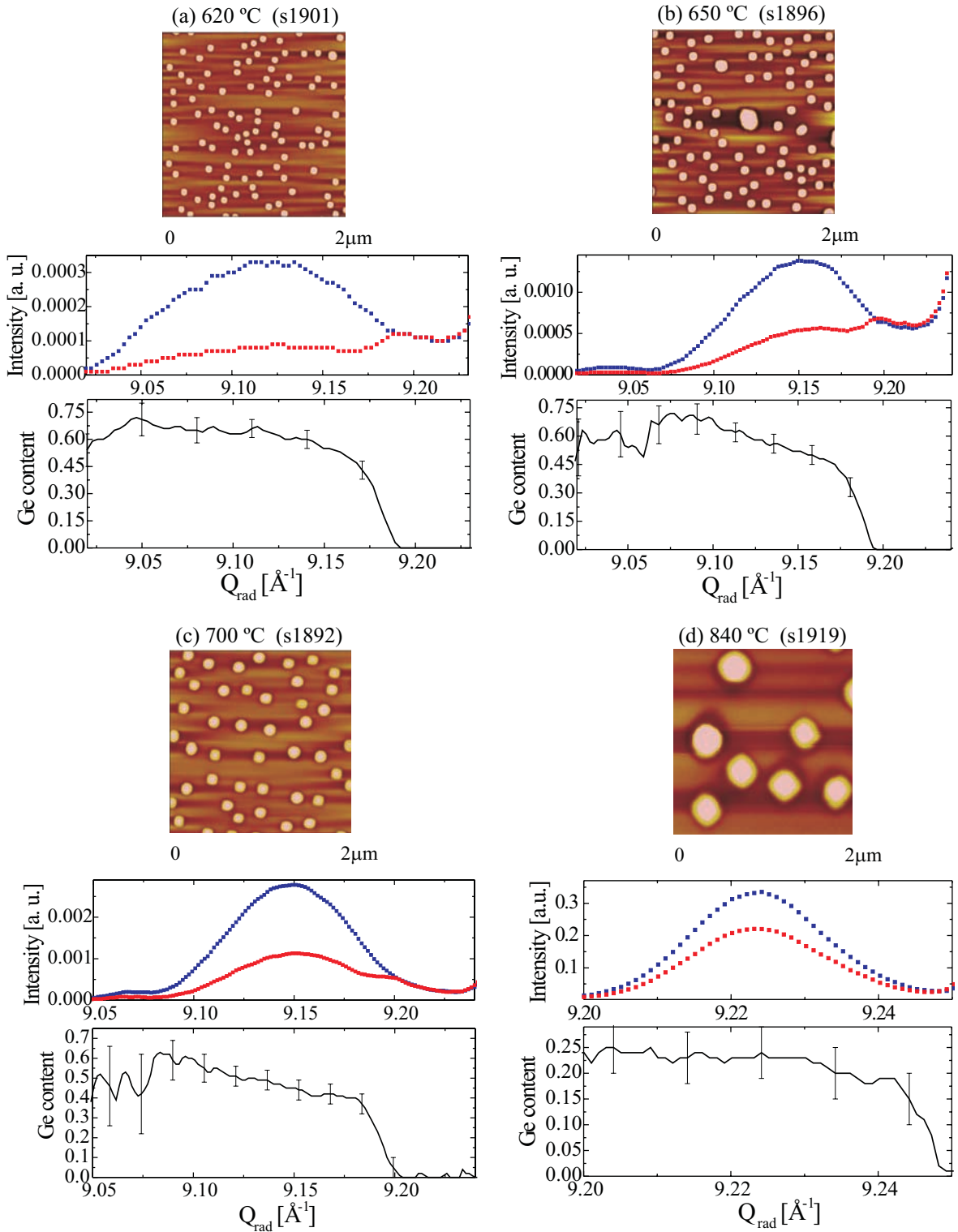
Figure 3.35: Temperature dependence of the Ge concentration profile. The AFM images show an increase of the dome size with growth temperature. Radial scans were recorded for the four samples grown at temperatures between 620 °C and 840 °C. The x-ray energies were chosen to be 60 eV below the Ge K-edge (blue squares) and 1 eV below the K-edge (red squares). The evaluation of the Ge content from these scans is plotted as a black line below the radial scans. The AFM images were recorded by M. Stoffel at the Max-Planck-Institute for solid state research in Stuttgart.

The steep gradient from pure Si to a significant (and only slowly evolving) Ge-content, appears to be present in all samples. We can indeed again state that the steepness of this gradient is at the resolution limit of our method. A perfect interface from the SiGe island to the Si substrate would show the same steepness in reciprocal space as we find in the samples in Fig. 3.35(a)-(c). This raises the question of where the relatively high Si content in the islands comes from. Interdiffusion through the interface between the substrate and the island seems at the first hand very likely, but can almost be excluded with the results presented in Figs. 3.35 and 3.34. Interdiffusion through an interface would certainly blur the sharp composition gradient. In particular the difference of the evolution of lattice parameter and composition as shown in Fig. 3.34 leaves a dramatic gradient in the elastic energy in the vicinity of the interface. As therefore neither elastic energy was minimized nor the entropy seriously affected at the substrate surface, it is considered to be frozen in a metastable state. There remains therefore two explanations for the origin of interdiffusion:

1. During the island formation, the moving Ge atoms dilute a part of the Si-substrate surface atoms, leaving the surface "perfect" apart from the first monolayers.

2. The island formation induces tensile strain inside the Si below the SiGe dome. To keep the crystal lattice of the Si coherent in the volume crystal and at the surface parts far away from the island, this tensile strain has to be compensated by a ring of laterally compressed Si. The elastic energy in this compressed region serves as the driving force to increase the mobility of these Si-atoms that finally dilute the Ge-dome during its formation.

A counter-argument against point **1.** is the fact that Ge wetting layers are reported from luminescence spectroscopy from such samples [75, 76]. The existence of such a Ge layer after the island formation makes the mobility of a vast part of the Si surface atoms during the growth unlikely. Our experimental results clearly favour therefore the interdiffusion of Si through the side of the dome. The well defined region exhibiting tensile strain in the Si exists. Its shape oscillations in Fig. 3.33 (b) indicate that it has a sharp boundary, either to silicon with a significantly different strain state, or to vacuum. As mentioned in point **2.** the compensation of the circular region of dilated Si below the SiGe island would require a ring-shaped region with high lateral compression. Atomistic elastic models have given evidence to the fact that this system would favour an increased surface energy by the removal of the highly strained Si and the formation of a ring-shaped trench surrounding the SiGe island. Furthermore, the works of Liao *et al.* and Chaparro *et al.* give also experimental evidence for strain relief via trench formation near the island perimeters [14, 77, 78]. In addition to our results obtained

via the anomalous scattering method with these from conventional x-ray diffraction studies, reciprocal space mapping on asymmetric reflections was performed using an x-ray energy of 10 keV. This method, introduced in sections 2.4.1 and 3.3.2 is used to determine the in-plane and out-of-plane lattice parameters in the non-uniform distorted SiGe islands. With the knowledge of the elastic constants of Si and Ge, this allows us to link a position in reciprocal space with a certain composition, according to its native lattice constant and the tetragonal distortion. For each sample, maps where recorded at the (224), the ($2\bar{2}4$) and the (404) reflection. Figure 3.36 shows the intensity distribution for these reflections for the samples s1901 (620 °C) in (a) and s1896 (650 °C) in (b). Two relaxation triangles are plotted, for the alloy compositions $Si_{0.5}Ge_{0.5}$ and $Si_{0.32}Ge_{0.68}$ in Fig. 3.36 (a) and for the compositions $Si_{0.55}Ge_{0.45}$ and $Si_{0.32}Ge_{0.68}$ in (b). These compositions were chosen from the results of the anomalous diffraction presented in Fig. 3.35. The intense peak to be seen at the Bragg position on the Si-substrate is mainly due to thermal diffuse scattering. The elongated tail in Q_z-direction is the truncation rod perpendicular to the substrate surface. The equivalent reciprocal space maps for the samples s1892 (700 °C) and s1919 (840 °C) are plotted in Fig. 3.37 (a) and (b). In (a) the relaxation triangles for the compositions $Si_{0.6}Ge_{0.4}$ and $Si_{0.4}Ge_{0.6}$ and in (b) those for $Si_{0.85}Ge_{0.15}$ and $Si_{0.76}Ge_{0.24}$ are added. In the first three samples, the diffracted intensity from the SiGe islands appears as an elongated diffuse streak. Note that in Fig. 3.36 (a) this streak appears to be parallel to the short cathetus of the relaxation triangles. This direction indicates an iso-composition line and hence confirms the rather constant composition throughout the island in sample s1901 that was measured in the anomalous diffraction experiment. The samples s1896 and s1892 that showed a more pronounced evolution of the Ge content exhibit a small inclination of the elongated intensity distribution. These maps confirm the results presented in Figs. 3.35 and Fig. 3.34 for the growth of SiGe islands obtained via pure Ge deposition at temperatures between 600 °C and 700 °C. The lattice parameter evolves continuously even throughout an interface almost unblurred by interdiffusion. This leaves tensile strain in the Si-substrate below the SiGe-dome and high compressive strain in the dome.

We note however, that the inclination angle between the diffuse intensity distribution and the relaxation cathetus changes between the (224) and the (404) reflections. Their azimuthal orientation in the (001) plane corresponds to the <110> and the <100> directions. These are the two main axes of elastic stiffness, *i.e.* the Si-lattice has the highest stiffness in the <110> direction and the lowest stiffness in the <100>. As the elastic anisotropy between these two directions is different between Si and Ge, the in-
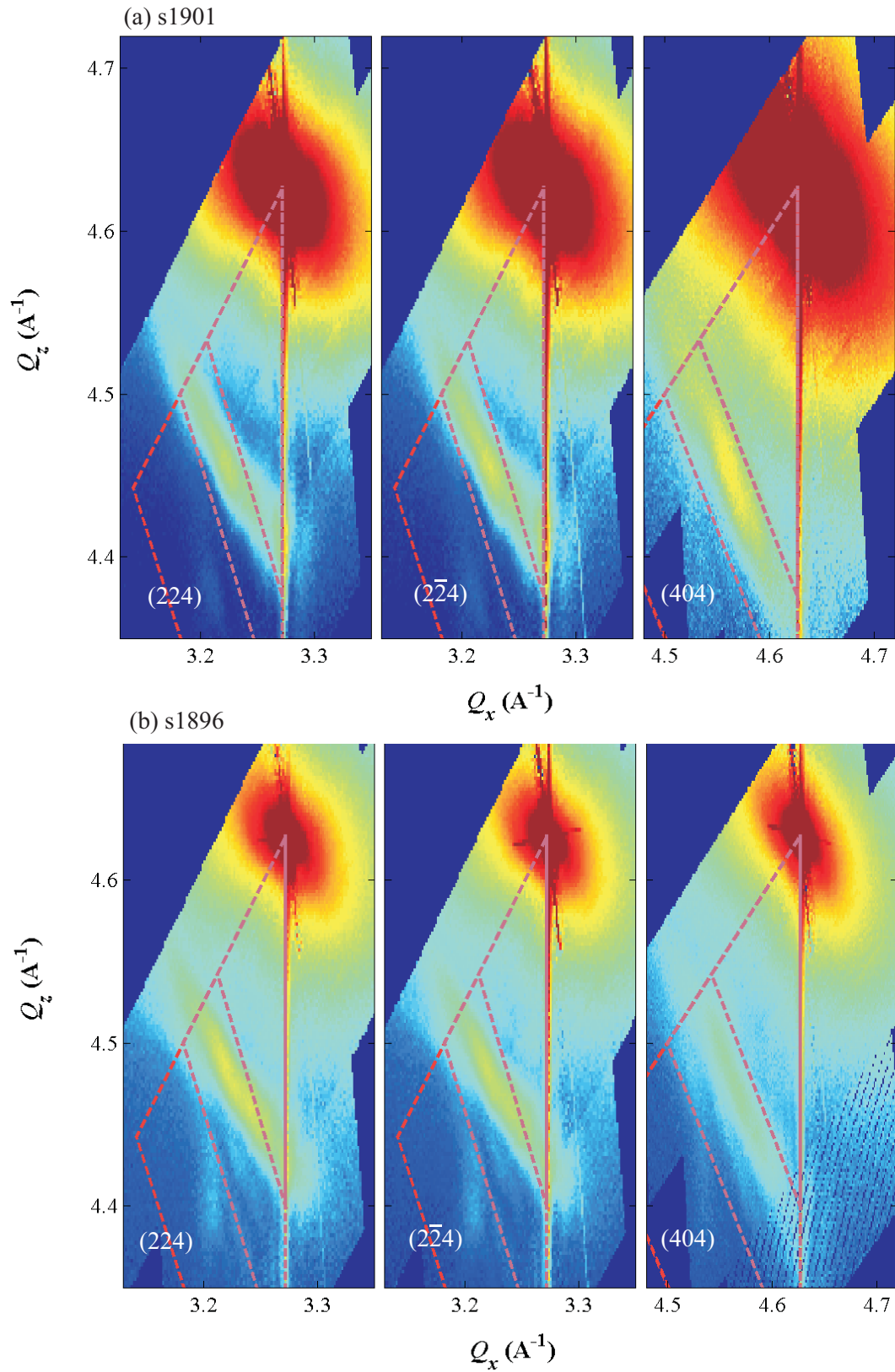
Figure 3.36: Reciprocal space maps of the samples s1901 in (a) and s1896 in (b). The relaxation triangles for Ge, $Si_{0.5}Ge_{0.5}$ and $Si_{0.32}Ge_{0.68}$ are plotted in (a), those for Ge, $Si_{0.55}Ge_{0.45}$ and $Si_{0.32}Ge_{0.68}$ are plotted in (b).
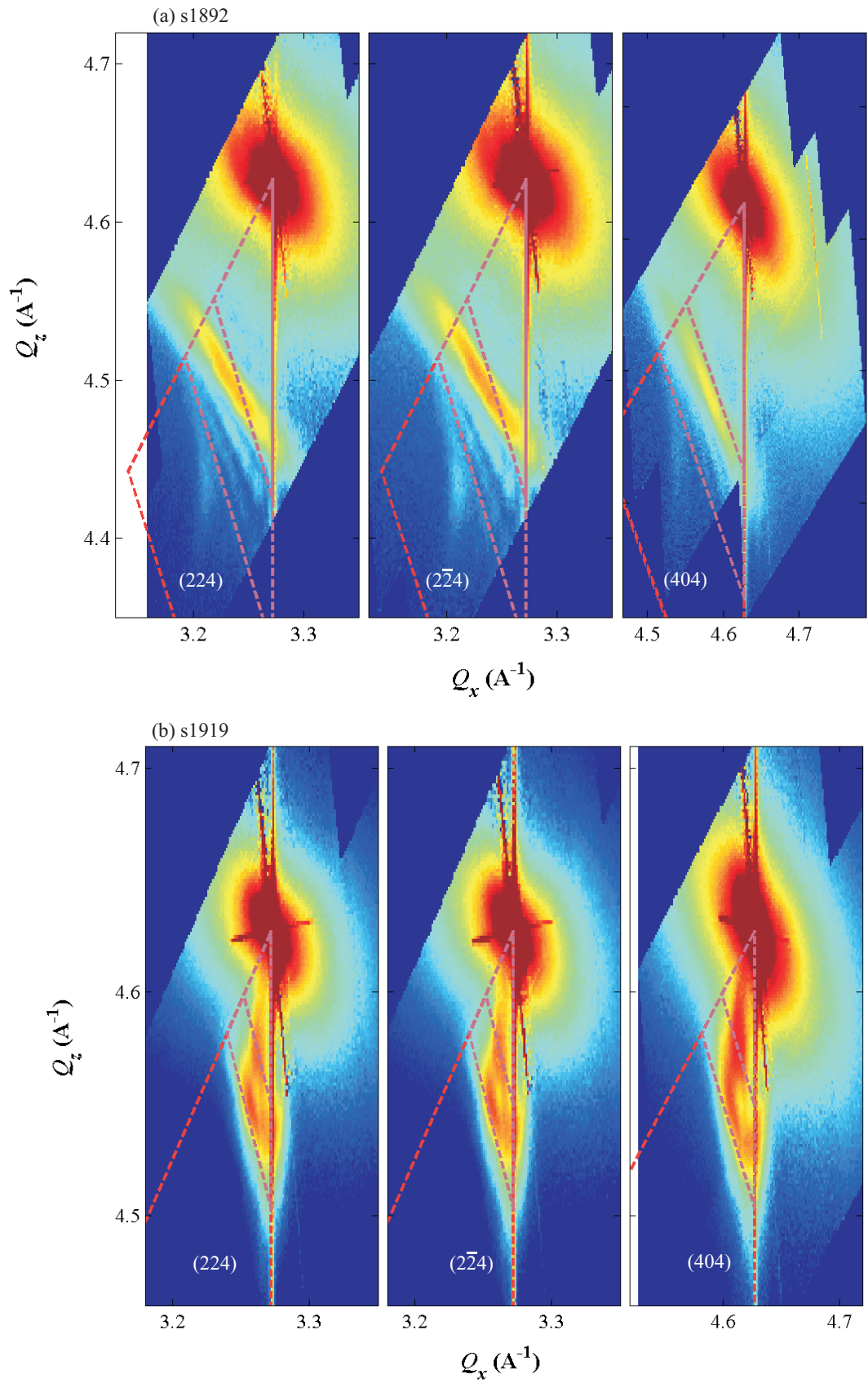
Figure 3.37: Reciprocal space maps close to asymmetric reflections of the samples s1892 in (a) and s1919 in (b). The relaxation triangles for Ge, $Si_{0.6}Ge_{0.4}$ and $Si_{0.4}Ge_{0.6}$ are plotted in (a), those for Ge, $Si_{0.85}Ge_{0.15}$ and $Si_{0.76}Ge_{0.24}$ are plotted in (b).

plane compression of the SiGe dome is expected to be anisotropic as well. We therefore have to consider our estimation of the Ge-content through the tetragonal distortion and Eq. (2.36) as being of tentative nature. As in the general case the distortion will be orthorhombic rather than tetragonal, the application of the theory of elasticity becomes less straightforward. The most suitable methods to be applied here are simulations using finite element procedures or atomistic lattice elasticity in order to simulate the diffuse intensity via Fourier transformation of the atomic lattice of the nano crystal. As the main conclusion from Figs. 3.36 and 3.37, we state that we can qualitatively deduce the trend of decreasing Ge content in the temperature regime from 600 °C to 700 °C, together with an increase in the gradient inside the island. For the sample s1919 grown at 840 °C, the diffuse intensity reaches up to the Si Bragg position. The large island size and the high amount of Si inside the island leads to a smooth transition between the scattering contrast, as well as between the lattice parameter difference of strained substrate and strained SiGe island. This smooth transition cannot be observed in the other samples sustaining our well defined dome-substrate interface.

In order to confirm the results, selective etching methods were employed at the Max-Planck-Institute for solid state research in Stuttgart in the group of O.G. Schmidt. Those methods make use of the fact that certain solutions composed of HF, H_2O_2, H_2O and CH_3COOH have an extremely selective etching behaviour between $Si_{1-x}Ge_x$ alloys and Si. The choice of the solution also determines a certain minimum Ge content x in order to dissolve the alloy [79, 80]. The samples s1901 (620 °C) and s1892 (700 °C) were etched with a solution removing all $Si_{1-x}Ge_x$ alloys with $x > 0.65$. The height of the islands in s1901 was reduced by this procedure by 30 %. In s1892 the height reduction was only about 7 %. Compared with our anomalous diffraction experiment, this confirms the fact that a concentration of 65 % Ge is indeed achieved in a significant part of the SiGe islands in sample s1901, whereas in s1892, only a very small amount of material seems to have this composition. This etching procedure therefore supports strongly the higher Ge content that was derived via the anomalous scattering method versus the lower Ge content that is estimated from the reciprocal space maps in Figs. 3.36 and 3.37 and their interpretation via Eq. (2.36). Sample s1901 was later etched with a solution that removes all $Si_{1-x}Ge_x$ alloys. Atomic force microscopy images of the sample before and after the various etching steps are shown in Fig. 3.38 (a)-(c). In (c), after the complete removal of the SiGe islands, ring-shaped trenches are visible. The interpretation of these trenches to be former hosts of a SiGe alloy that has been removed can be excluded, as this region has to suffer from compressive strain when the region below the SiGe dome is dilated. Even if the growth temperature would

allow SiGe alloy formation via solid state interdiffusion, the material exchange would certainly take place through the interface, where the reduction of the elastic energy by this process could act as a driving force.
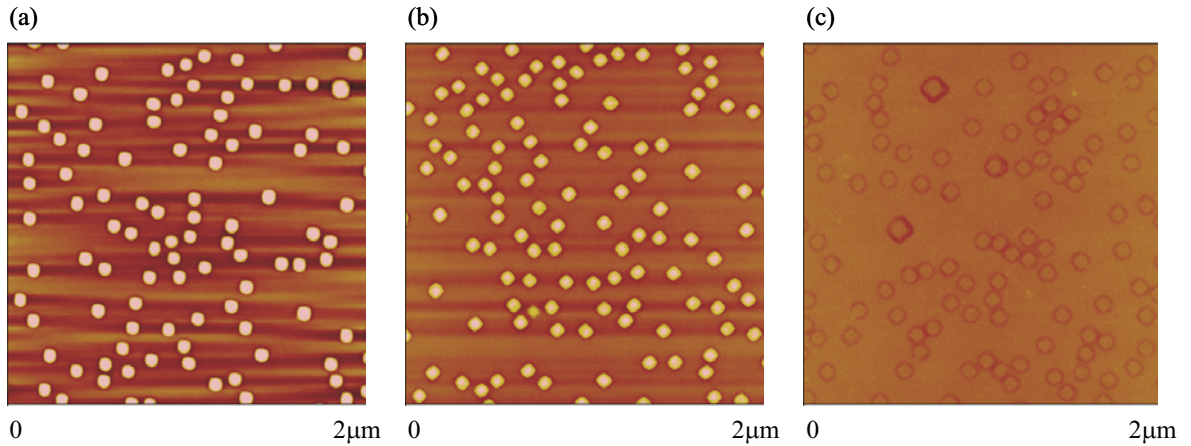

Figure 3.38: AFM images of sample s1901 for various selective etching steps. (a): before etching. (b) after removal of all $Si_{1-x}Ge_x$ alloy components with $x > 0.65$. (c): Total removal of all SiGe alloys. Ring-shaped trenches are visible.

Considering all three experiments, anomalous diffraction, reciprocal space mapping and selective etching, we can conclude that in the temperature regime between 600 °C and 700 °C the growth of SiGe domes is obtained without interdiffusion through the substrate-dome interface. The well defined strained region in the Si substrate below the SiGe dome, together with the finite size oscillations shown in Fig. 3.33 strongly support the assumption that the main source of Si-interdiffusion are the trenches around the island perimeter. A general decrease of the Ge-content with increasing temperature is confirmed. A sketch of the interpretation of the growth mode and the interdiffusion via the formation of trenches is shown in Fig. 3.39. The patterned part in the Si-substrate indicates the region in the Si substrate which suffers from tensile strain. The tendency for smaller domes with higher Ge content for lower growth temperatures is also visible in the photoluminescence (PL) spectra of SiGe islands covered with Si. Typical spectra are presented in Fig. 3.40 for three growth temperatures.
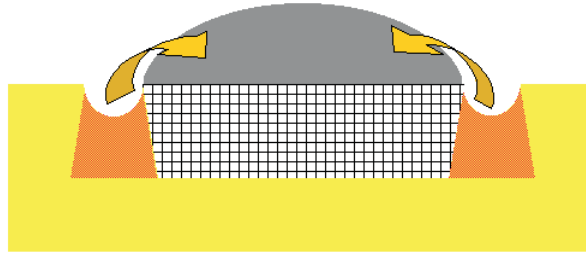
Figure 3.39: The formation of trenches in the Si-substrate is attributed to be an important Si-source in the alloying process during the SiGe island formation after deposition of pure Ge on Si(001). The patterned region below the dome represents the region in the Si substrate that suffers from tensile strain. The red parts are highly compressed.
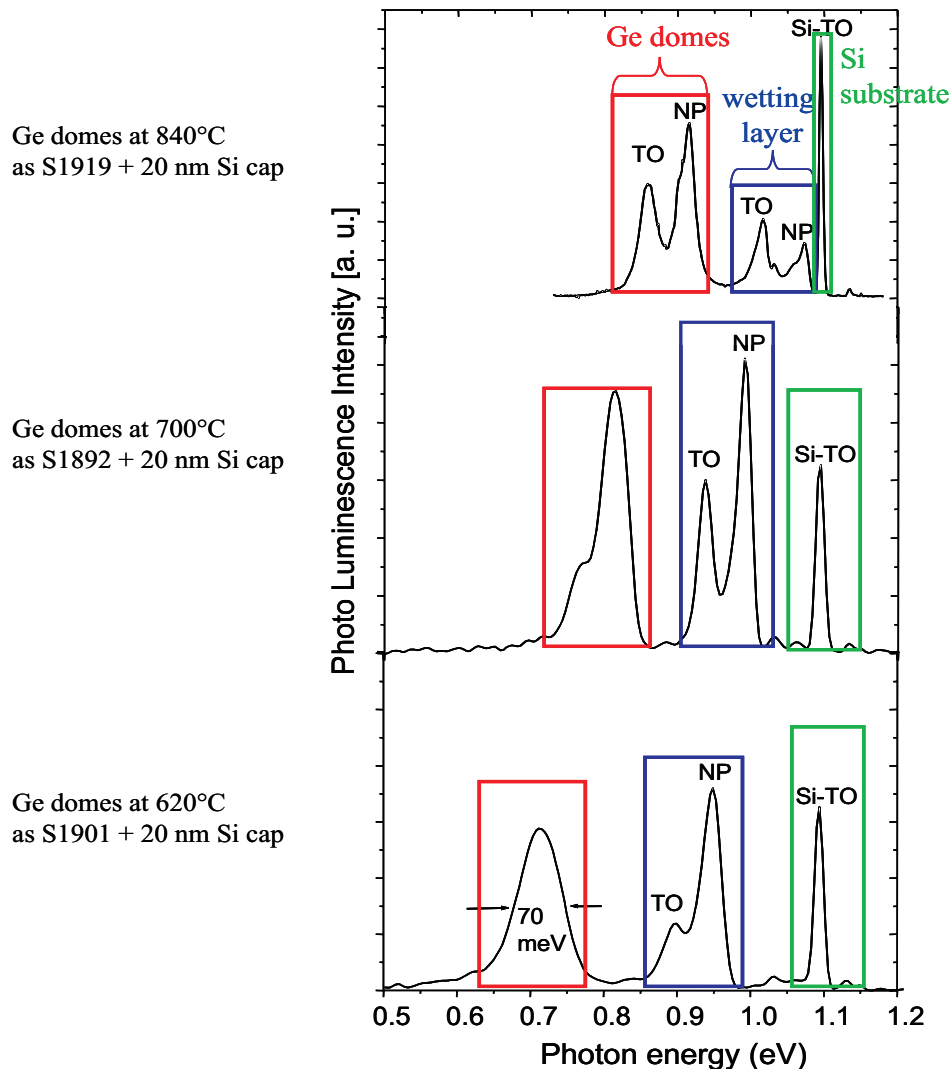
Figure 3.40: Photoluminescence (PL) spectra of capped SiGe domes. The influence of the growth temperature on the Ge content is visible in the shift of the Pl peaks of the domes to lower energies. The spectra were recorded by M. Stoffel.

For the largest domes (marked by the red frame), grown at 840 °C, the luminescence signal is closest to the transition energy of pure Si (green frame), indicating the highest interdiffusion of all samples. The signal from the alloyed wetting layer is also present and marked by the blue frame. The splitting of the peaks is due to no-phonon transition and the phonon assisted transition. In the second case, a transversal optical phonon is excited, causing an energy loss of 58 meV of the emitted photon. These peaks are labelled NP and TO in the graphs of Fig. 3.40. For the smaller islands, grown at lower temperatures, this peak splitting is no longer observable. This is due to the broadening of the signal caused by size fluctuations that influence the confinement energy. For smaller domes, these fluctuations are more important and therefore lead to a broadened PL-signal. The luminescence peak fur pure (bulk-) Ge is expected at 0.74 eV. In the nanostructures investigated here not only the composition but also the complicated strain distribution in the SiGe dome and the surrounding Si matrix influences the energy of the spatially indirect transition. It is assumed, that recombination takes place between holes in the confined SiGe island and electrons in the strained Si (see [81] and references therein). Recently, PL-peaks from capped Ge hut-clusters have been measured at 0.63 eV, well below the expected value for bulk Ge. [81]. This clearly underlines the importance of an analytical method to determine the Ge composition independently from optical or electronic properties. A more detailed discussion of the luminescence spectra will be published elsewhere [82].

3.7 Interdiffusion and facet orientation in PbSe quantum dots

3.7.1 Anomalous reciprocal space mapping on IV-VI compound quantum dot superlattices

The tools we have used for a quantitative analysis of strain and interdiffusion in free standing SiGe island on a Si(001) surface will now be combined, and applied to a more complex system. In this section we will study buried quantum dots and 3 dimensionally ordered quantum dot superlattices of lead chalcogenides via anomalous reciprocal space mapping. The questions that arise here are of a less quantitative nature than in the sections 3.6.1 and 3.6.2. It is also the higher complexity of the system that defines our limits in the quantitative data interpretation. The growth of PbSe quantum dots on cubic (111) surfaces has been studied in great detail on a variety of substrates [83, 84, 85]. They tend to form trigonal pyramids with {010} facets. The huge elastic anisotropy in the (111) plane of the lead chalcogenides as PbSe and PbTe, strongly favours this shape of the nano crystals, together with a short range order (SRO) hexagonal arrangement of the islands in the (111) plane [41, 86]. This hexagonal arrangement, however, evolves strongly if these quantum dots are grown in multilayer stacks.

The critical thickness for island formation of PbSe on top of PbTe is about 1.5 monolayers. A typical deposition of 5 monolayers (about 18 Å nominal thickness) leads to the formation of trigonal pyramids with a height of 90 Å. When these dots are then covered by a 200 Å thick $Pb_{0.92}Eu_{0.08}Te$ cap, the surface is completely flattened. As the overgrowth happens to be almost dislocation free, the strain influenced by the PbSe islands into the cap layer propagates to the surface. The elastic anisotropy of these materials leads to certain favoured directions of strain propagation, leaving three strain branches reaching from every trigonal PbSe pyramid to the surface of the cap [41]. It leaves a flat, but strain modulated template for the growth of the next PbSe quantum dot layer. Due to the lattice mismatch of -5.54 % between PbSe and PbTe, these strained spots on the surface act as nucleation sites for the formation of the PbSe pyramids. This leads to a self-organized stacking order of PbSe quantum dots in a multilayer. The nature of the order can be changed form a vertical stacking in columns to an fcc-like ABCAB...stacking via a choice of the spacer layer thickness [87, 88]. The alloying of PbTe with 8 % Eu in the spacer layers increases slightly the lattice parameter in $Pb_{0.92}Eu_{0.08}Te$, leading to an average in-plane lattice parameter of the $Pb_{0.92}Eu_{0.08}Te$/PbSe multilayer that is in elastic equilibrium with the PbTe buffer on which the whole stack is grown. After various stacking periods, the self organization of

the nucleation sites leaves an almost perfect vertical order and a long range hexagonal order in the growth plane. The growth parameters for the 3D-ordered quantum dot superlattice M925 are presented in Table III.

Sample	T (°C)	d_{PbSe} (ML)	$d_{Pb_{0.92}Eu_{0.08}Te}$ (Å)	$PbSe/Pb_{0.92}Eu_{0.08}Te$ layers
M925	360	5	460	30

Table III: Growth parameters of the investigated quantum dot superlattice M925. The sample was grown by G. Springholz at the institute for semiconductor physics in Linz.

Figure 3.41 shows AFM images of the last layer on top of a 50 x $Pb_{0.92}Eu_{0.08}Te/PbSe$ superlattice. In (a) the hexagonal ordering is visible in the Fourier transform power spectrum in the inset determined from the AFM image. Figure 3.41 (b) shows a magnified view of the orientation of the
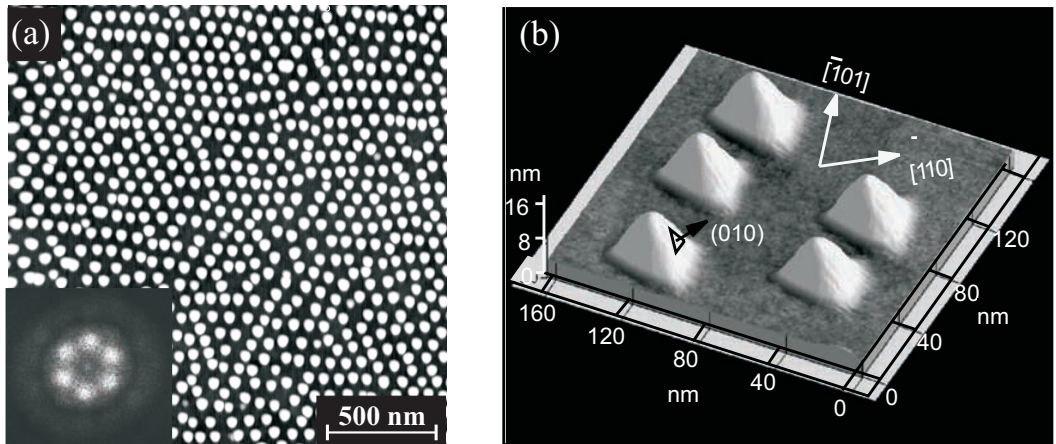
Figure 3.41: AFM images of the last layer on top of a 50 x $Pb_{0.92}Eu_{0.08}Te/PbSe$ superlattice. (a) Hexagonal order of the PbSe dots together with the Fourier transform power spectrum in the inset. (b) Magnification of the trigonal PbSe pyramids with (010) facets. The samples were grown in the group of G. Springholz at the institute for semiconductor physics in Linz.

Overgrowth of epitaxial nanostructures tends to change or wash out facets, either by transformation of the islands into a flatter structure or by interdiffusion [89, 90]. In the case of the 3 dimensional ordering of quantum dots, knowledge about the facets or their change during the growth is a crucial feature to understand and further control the growth process. In x-ray diffraction or small angle scattering, one should see a pronounced facet as a well oriented interface or surface. It should therefore show a crystal truncation rod like structure - a streak in reciprocal space in the direction of the facet normal. The contrast in x-ray scattering between PbSe and $Pb_{0.92}Eu_{0.08}Te$ is quite poor

however, so that in the case of reciprocal space mapping, we would rather record the strain modulation due to the different lattice parameter. As we have seen in the sections 3.6.1 and 3.6.2 such non-dislocated heteroepitaxial structures can show smooth lattice parameter transitions through interfaces without featuring interdiffusion. This would mean that the strain contrast mapping in reciprocal space would point out very well the 3D periodic structure and its long range order via a 3D satellite arrangement in the vicinity of the Bragg reflections. The intensity distribution enveloping these satellites however would not show any traces of facets, as the lattice parameter is expected to evolve continuously even through chemically abrupt interfaces.

We therefore have to increase the chemical contrast to be more important than the strain contrast. The only method to solve this problem is anomalous diffraction on a superstructure Bragg reflection at very low x-ray energies to excite the Pb M-shell resonance. The idea of this method has already been discussed in sections 3.4.4 and 2.5.1 and applied in section 3.5. Looking back at Fig. 3.17 we recall, that at 2400 eV at the (111) reflection, the scattered intensity from $Pb_{0.92}Eu_{0.08}Te$ is about a factor of 50 weaker then that of PbSe. This scattering difference decreases to a factor of two at 8000 eV. At this rather usual diffraction energy, the scattering is mainly determined by the surrounding $Pb_{0.92}Eu_{0.08}Te$ matrix than by the PbSe dots. The amount of $Pb_{0.92}Eu_{0.08}Te$ in the sample is also a factor of 10 higher than the amount of PbSe. The low energy diffraction therefore enables us to highlight the PbSe dots in the $Pb_{0.92}Eu_{0.08}Te$ matrix.

The experiment required the use of the specially designed gas detector described in section 3.2.3. In the coplanar geometry reciprocal space maps were recorded of a highly ordered $Pb_{0.92}Eu_{0.08}Te$/PbSe quantum dot superlattice. To demonstrate the sensitivity of our method, we recorded maps in the vicinity of the symmetric (111) Bragg reflection for 10000 eV and 2400 eV. Figure 3.42 compares the 10000 eV data in (a) with the 2400 eV data in (b). The strong scattering contrast increases the visibility of the number of satellites from the 3D stacking order of the PbSe quantum dots. Line scans for the corresponding energies as extracted from the maps along Q_z for Q_x=0 are plotted below in (c) and (d). The small ovals indicate the envelope function corresponding to the $Pb_{0.92}Eu_{0.08}Te$ matrix, the large oval the one from the PbSe dots. The comparison of the two maps illustrates clearly the necessity to measure these samples at low energies. At 10000 eV the centre of the envelope is in the vicinity of the $Pb_{0.92}Eu_{0.08}Te$ reciprocal lattice point at 1.68 Å^{-1}. At 2400 eV we can see two envelopes. One is again drawn as the small oval around the reciprocal lattice point of $Pb_{0.92}Eu_{0.08}Te$, the second, broader envelope corresponds to the small PbSe dots and is located at higher Q-values. Note

that relaxed PbSe would be expected at a Q_z position of 1.77 Å^{-1}. Any rhombohedral distortion would shift it to even higher Q-values. This indicates that the dots suffer from either hydrostatic compression and/or significant interdiffusion.
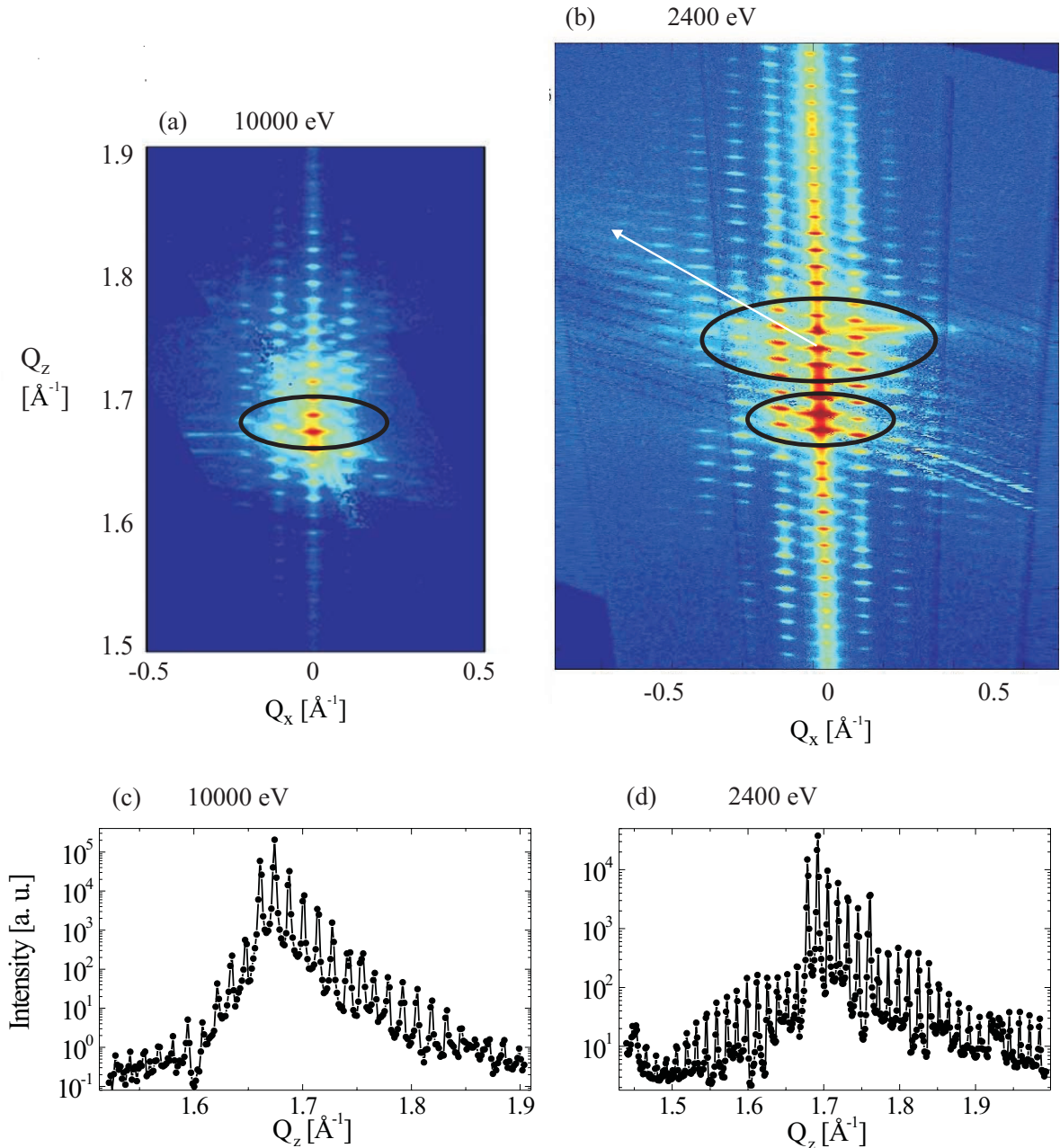

Figure 3.42: Reciprocal space maps of the $Pb_{0.92}Eu_{0.08}Te$/PbSe quantum dot superlattice M925 in the $[11\bar{2}]$ azimuth at 10000 eV in (a) and 2400 eV in (b). The small ovals act as guide to the eyes for the envelope of the satellites caused by the $Pb_{0.92}Eu_{0.08}Te$ matrix. The large oval describes the envelope corresponding to the PbSe dots. The white arrow indicates a streak in the diffuse intensity distribution. (c) and (d): Linescans along Q_z for Q_x=0 for both energies were extracted from the maps in (a) and (b).

Another important highlight in Fig. 3.42 (a) is the streak indicated by the white arrow leaving the envelope of the PbSe dots to the upper left. This indicates the existence of facets. As our intention was to look for their existence or transformation we will focus our interest in the following on this feature. To understand its appearance, we have to have a look at the sample- and the diffraction geometry. When performing coplanar diffraction on a symmetric reflection, *i.e.* a reflection that lies on the specular path, we can map any plane containing the surface normal and in-plane direction of our choice. Therefore we can rotate the sample around its surface normal and look for the facets in various in-plane orientations. As can be seen from Fig. 3.41 (b), the [010] facet normal is equivalent to the [1$\bar{1}$0] in-plane orientation. To see its truncation rod in reciprocal space, we have to record a map in the plane spanned by the surface normal [111] and the [1$\bar{1}$0] direction. To name it after its normal we call it the (11$\bar{2}$) plane. For reasons of the trigonal symmetry of the (111) surface, we should get an equivalent map for a rotation of 120 °. For a rotation of 60 ° we map the ($\bar{1}\bar{1}$2) plane and therefore should see the facet streak mirrored at the [111] (Q_z) direction. Maps recorded on the (111) Bragg reflection in these two planes are plotted in Fig. 3.43 (a) and (b). The top view of the section of the mapped plane through the PbSe pyramids is sketched for both azimuthal orientations. Both graphs show an asymmetry respective to the Q_x=0 axis. The asymmetry in (a) corresponds to the mirror image of the asymmetry in (b). The directions for eventual truncation rods from [010] or [211] facets are added as white lines. The flatter facets, the [211] facets, would correspond to the steeper line. Its inclination angle to the Q_x=0 axis is 19.5 °. That of the [010] facet normal amounts to 54.7 °. The black arrows serve as a guide to the eye to estimate the observed facet orientation.

For the {110} planes two orientations rotated by 60 ° with respect to each other were recorded. They are shown in Fig. 3.44 (a) and (b). The sections of these scans through the pyramids are again sketched. This time the situation is symmetric and no asymmetric streaks appear in the reciprocal space map. The horizontal streaks at 1.76 Å^{-1} that are visible in some of the maps are due to a twin structure in the BaF$_2$ substrate. We can conclude from the maps that the trigonal symmetry of the PbSe pyramids is conserved during the overgrowth. The facets however, seem to flatten significantly. The determination of the most likely orientation of the facets as done by a simple estimation by eye and indicated by the black arrows in Fig. 3.43 is certainly rather crude. But it definitely excludes the {010} facet orientation that was present in the uncovered pyramids. The facet orientation from these maps is estimated to be of the order of 35° ± 5°.
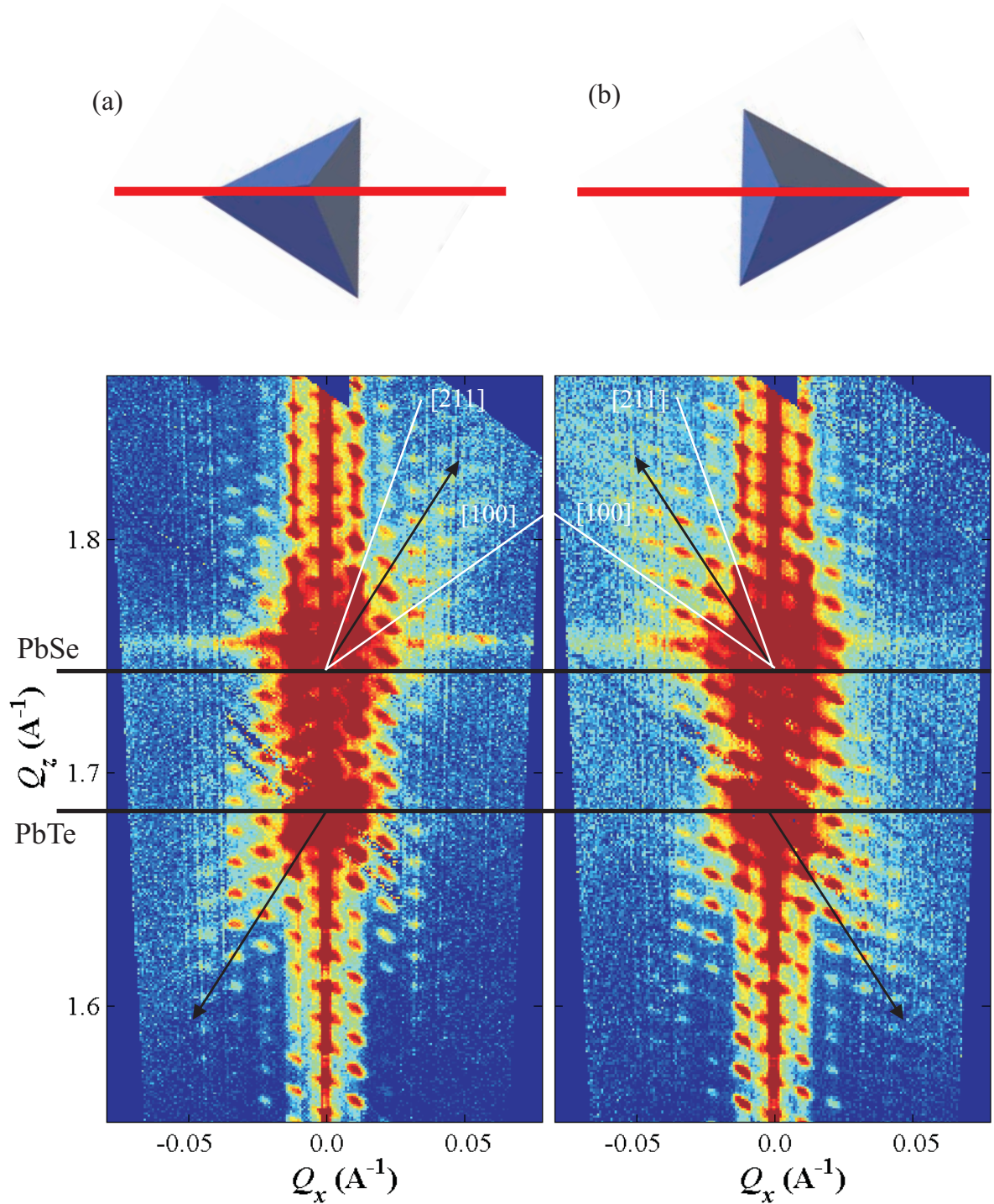
Figure 3.43: Reciprocal space maps of the symmetric (111) Bragg reflection of the $Pb_{0.92}Eu_{0.08}Te/PbSe$ quantum dot superlattice M925 in the $<11\bar{2}>$ azimuth (a): $[2\bar{1}\bar{1}]$ azimuth. (b): $[11\bar{2}]$ azimuth. The pyramids indicate the sample orientation for the corresponding map. The white lines indicate the orientations of the $\{211\}$ and $\{010\}$ facets in reciprocal space, the black arrows indicate the observed direction of the facet normal.
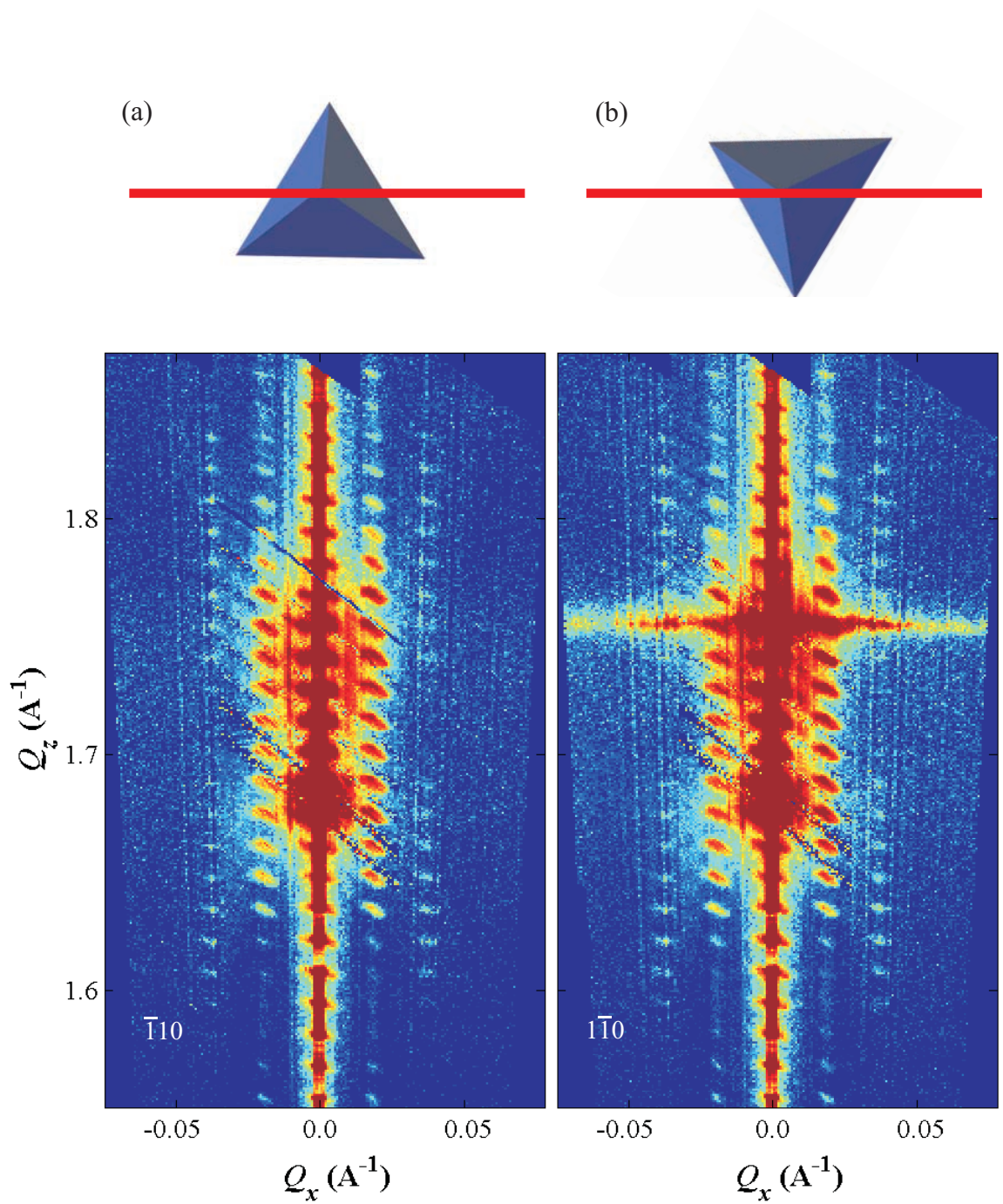
In the three dimensional stacking order of these pyramids, the strain propagating from each covered pyramid through the cap layer to the surface induces nucleation of the successive pyramids. A theoretical treatment of the elastic properties shows that in the case of $Pb_{0.92}Eu_{0.08}Te/PbSe$ quantum dot superlattices grown along [111] direction, three favoured directions for this strain propagation exist [91]. Projected in the (111) plane, they point into the three $<11\bar{2}>$ in-plane directions and form an angle of 36° with the [111] growth direction. This corresponds well to the $<411>$ direction (35°). Although the $<311>$ (29°) and $<511>$ (39°) orientations are close. Figure 3.45 shows a top view of one of the pyramids together with some of the crystal lattice directions indicated in a stereographic projection.

Figure 3.45: Orientation of the PbSe pyramids and the crystal lattice. The Blue triangle sketches the top view of one PbSe pyramid. The edges are oriented in the (111) plane along $< 1\bar{1}0 >$, the facet normals are oriented in a $< 2\bar{1}\bar{1} >$ azimuth.

Therefore every pyramid induces three nucleation sites on the surface of the spacer layer that covers the islands. The lateral distance between the subsequent islands is determined by the inclination angle of the direction of preferred strain propagation and the spacer thickness. This angle of the island replication was measured in TEM studies to be 39° [86]. So far it has not been attributed to affect the facet orientation

Figure 3.44: Reciprocal space maps of the symmetric (111) Bragg reflection of the $Pb_{0.92}Eu_{0.08}Te/PbSe$ quantum dot superlattice M925 in the $<1\bar{1}0>$ azimuth. The pyramids indicate the sample orientation for the corresponding map. As no facets are expected here, the maps appear symmetric. (a): $[1\bar{1}0]$ azimuth. (b): $[10\bar{1}]$ azimuth. The horizontal streak at 1.76 Å^{-1} is an artefact due to a twinned BaF_2 substrate.

as only the facets of the uncovered layer of pyramids were investigated and determined to be {010} planes with an inclination angle of 54.7 ° . The facet orientation that we derive here seems to be very close to the direction of preferred strain propagation. The overgrowth of these PbSe-islands with $Pb_{0.92}Eu_{0.08}Te$ therefore flattens the island by changing the facet inclination angle by about 20°.

3.7.2   Influence of interdiffusion during the overgrowth of PbSe islands

As mentioned before, the Eu in the $Pb_{0.92}Eu_{0.08}Te$ leads to a strain symmetrization of the $Pb_{0.92}Eu_{0.08}Te$/PbSe superlattice with the underlying PbTe-buffer. But there is also a significant improvement of the growth quality concerning the vertical stacking order of the dots investigated. One possibility of this improvement could be that the 8 % Eu prevent interdiffusion and therefore the dilution of the islands during the overgrowth. In order to investigate the influence of the overgrowth material, two samples with a single pyramid layer were grown on a PbTe buffer and a BaF_2 substrate. The pyramids were produced via a deposition of 5 monolayers of PbSe. Sample M1205 was then covered with a 250 Å $Pb_{0.92}Eu_{0.08}Te$ cap layer and M1206 was overgrown with 250 Å PbTe. In Table IV, the parameters for both samples are listed.

Sample	T (°C)	d_{PbTe} (buffer)	d_{PbSe} (ML)	Cap layer
M1205	360	5.1 μm	5	250 Å $Pb_{0.92}Eu_{0.08}Te$
M1206	360	2.7 μm	5	250 Å PbTe

Table IV: Growth parameters for the samples M1205 and M1206, containing a capped layer of PbSe pyramids. The samples were grown by G. Springholz at the institute for semiconductor physics in Linz.

To enhance the visibility of the PbSe islands with respect to the cap layer and the underlying PbTe buffer, anomalous reciprocal space mapping at low energies was performed. These samples now offer the opportunity to acquire complementary reciprocal images at the (111) Bragg reflection.
The diffraction minima of PbTe and $Pb_{0.92}Eu_{0.08}Te$ in the vicinity of 2400 eV can be exploited to suppress the scattering of the cap layers. A reciprocal image taken at 2490 eV demonstrates the complementary situation of a suppression of the PbSe islands. The complementary maps for the sample M1205 are plotted in Fig. 3.46, those for sample M1206 in Fig. 3.47. The symmetric (111) Bragg reflection was mapped out in an azimuthal direction that is supposed to include the facet truncation rod. In (a) the energy was tuned to 2410 eV in order to suppress $Pb_{0.92}Eu_{0.08}Te$ and highlight the

PbSe pyramids. The corresponding reciprocal image shows the PbTe buffer peak and the thickness oscillations of the $Pb_{0.92}Eu_{0.08}Te$ cap along the specular path at $Q_x=0$.
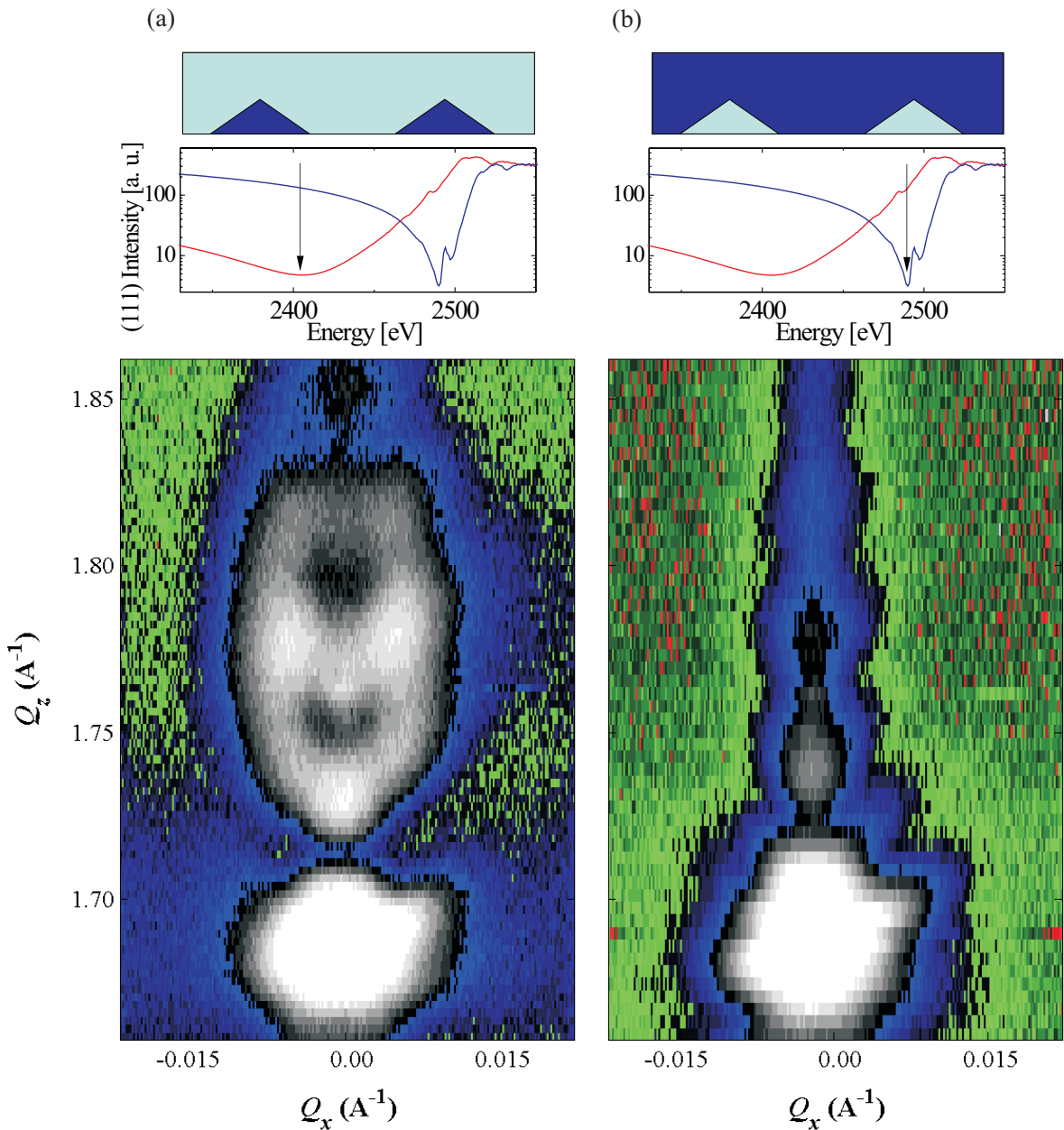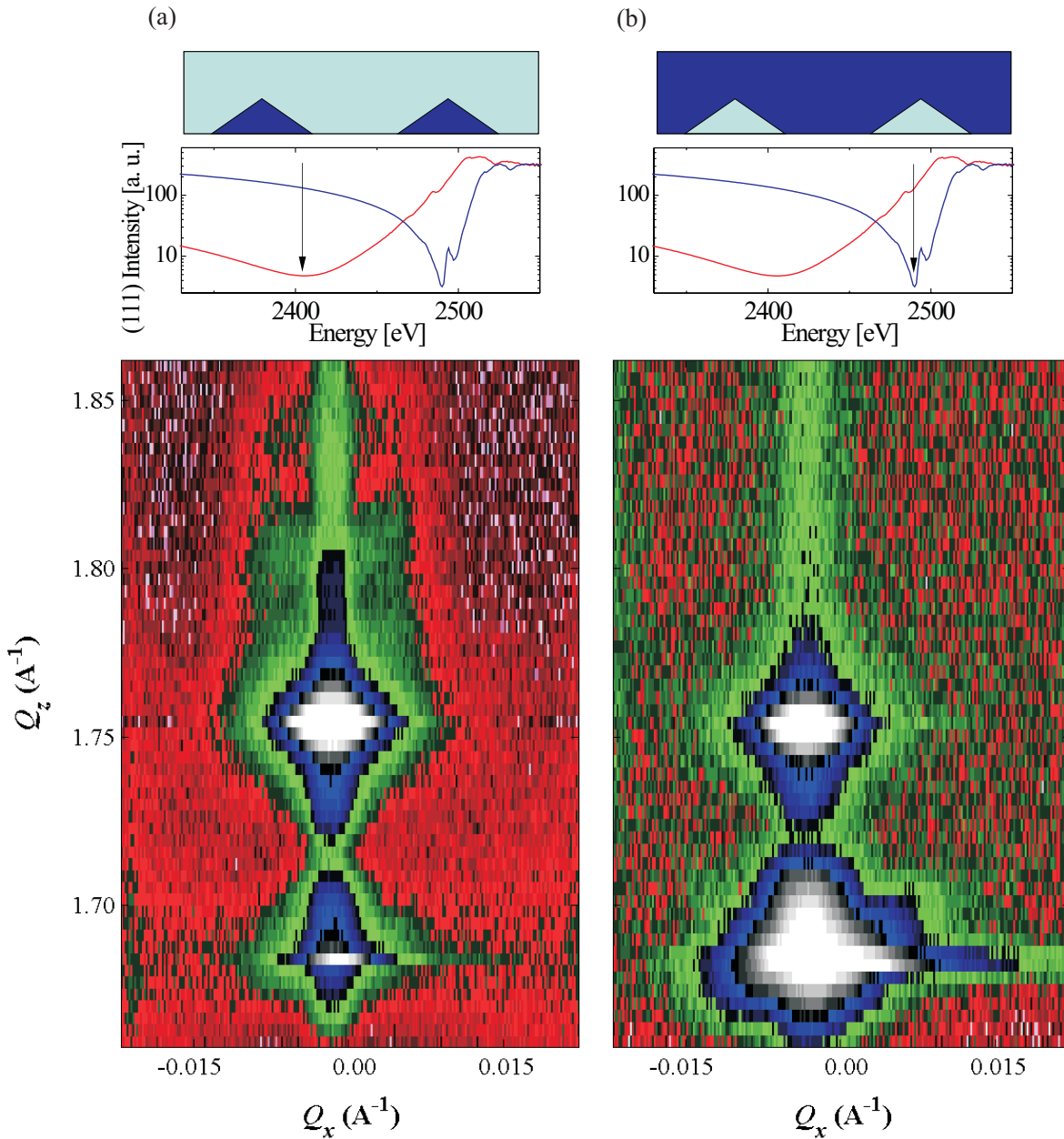

Figure 3.46: Reciprocal space maps of the (111) Bragg reflection of M1205, a single layer of PbSe pyramids capped with $Pb_{0.92}Eu_{0.08}Te$. (a): recorded at 2410 eV ($Pb_{0.92}Eu_{0.08}Te$ suppression) (b): recorded at 2490 eV (PbSe suppression).

The pronounced diffuse features in the diffuse scattering at $Q_z=1.77$ Å^{-1} for $Q_x = \pm0.005$ Å^{-1} corresponds to the in-plane structure factor of the pyramid auto-correlation function. For the growth of a single layer of PbSe pyramids, those are disordered and therefore have the structure factor of a liquid. The correlation maxima at $Q_x = \pm0.005$

Å^{-1} correspond to an average nearest neighbour distance of 1200 Å. The slight asymmetry of the diffuse intensity distribution to the upper right, represents the pyramid facets.

Figure 3.47: Reciprocal space maps of the (111) Bragg reflection of M1206, a single layer of PbSe pyramids capped with PbTe. (a): recorded at 2400 eV (PbTe suppression) (b): recorded at 2490 eV (PbSe suppression).

The situation in Fig. 3.46 (b) is inverted. The PbSe pyramids are suppressed at 2490 eV and the features in the reciprocal image are mainly attributed to the thickness oscillations and the truncation rod of the PbTe buffer. The structure factor of the dis-

ordered PbSe islands is not visible anymore.

Sample M1206, which was capped with 250 Å PbTe was investigated in the same way. Reciprocal images were recorded at complementary energies of 2400 eV and 2490 eV to suppress either the PbTe cap or the PbSe pyramids. The measurements are presented in Fig. 3.47 in a way equivalent to Fig. 3.46. This time the (111) Bragg reflection of the BaF_2 substrate is visible, as the PbTe buffer was thinner in sample M1206 than in M1205. Apart from this, it is instantly visible, that in Fig. 3.47 (a) the correlation function attributed to the PbSe islands is significantly less important than in Fig. 3.46 (a). Also the difference between the complementary images is less pronounced then in Fig. 3.47. Obviously the overgrowth of the PbSe pyramids by PbTe has a much stronger impact than the $Pb_{0.92}Eu_{0.08}Te$ capping. The interdiffusion of Te in the PbSe islands leads to a significant change in their shape. The data in Figs. 3.46 and 3.47 do not allow for a determination of the island height however. The improved growth of the 3D ordered PbSe pyramid superlattices by adding 8 % Eu to the PbTe is therefore rather unlikely to be attributed only to the strain symmetrization achieved by this alloying. It rather seems, that the Eu prevents interdiffusion, therefore leading to a stronger strain patterning of the cap layer by the PbSe pyramids

4 Outlook

In this work we have presented new methods concerning mainly the anomalous scattering technique and its application to structural studies of crystalline nano-structures. The advancement that has been achieved will have a strong impact on the increasing use of synchrotron radiation in the field of structural characterization of nano-sized materials. With the progress of experimental techniques and instrumentation, the difficulties that may affect anomalous diffraction, such as inelastic scattering or absorption in the case of low energies, will become less important. The use of specially adapted detectors and the design of dedicated beamlines that offer a wide energy flexibility will certainly increase the exploitation of the 4-dimensional diffraction parameter space given by the momentum transfer $\vec{Q}$ and the x-ray energy E. Confined systems are currently a focus of interest, on the one hand due to the promising applications of the new physical properties of conduction electrons under quantum confinement in semiconductor nano-structures. On the other hand, the thermodynamic and kinetic aspects of the growth of confined systems are of crucial interest for fundamental research and technology. Lattice distortions and compositional gradients are "frozen" in metastable states, far from thermodynamic equilibrium. Surface energies and therefore *e.g.* the crystallographic orientation of interfaces of nano-crystals will also affect the total energy stored in these systems. It is therefore still open to discussion, which growth characteristics will appear under certain growth conditions. Hence the demand for experimental methods that can elucidate these problems of strain distribution and interdiffusion will attract further interest. As the methods presented in this work still cannot resolve lateral gradients of composition and strain, a possible future development is the use of x-ray beams focussed to sub-micron spot sizes. This tool will combine a direct spatial resolution with the benefits of composition and strain resolution from diffraction. Highly intense sources of synchrotron radiation together with the recent developments in micro-focussing devices can therefore open the way to a single quantum dot spectroscopy. A microscopic resolution of the structural properties of the "nanoworld" is certainly one important key in the understanding of the very fundamental and universal physics which is present in the limits of quantum confinement or the finite size of a thermodynamic system.

Appendix

A   Analytical solutions for Fourier transforms of perfect films

A.1   The diffracted intensity from a thin film

In the case where diffraction is only to be considered in a direction perpendicular to the plane of a perfect thin film, we can simplify the description of its Fourier transform. For reasons of symmetry, we can replace such a perfect system by a linear stacked chain of atoms. Applying the convolution theorem from Eq. (2.14) and the solution for the geometrical series as shown in section 2.5.2, we can write for the diffracted intensity:

$$I\left(Q\right) = AA^* = \left(f_{a_1} e^{i\phi_{a_1}} \frac{e^{iQN_a a} - 1}{e^{iQa} - 1}\right) \left(f_{a_1} e^{i\phi_{a_1}} \frac{e^{iQN_a a} - 1}{e^{iQa} - 1}\right)^* \tag{A.1}$$

To evaluate the complex conjugate, we have to get rid of all imaginary arguments in the denominator. This is achieved via a multiplication of both complex fractions in Eq. (A.1) with $\frac{e^{-iQa} - 1}{e^{-iQa} - 1}$. With the trigonometric complex notation $e^{i\omega} = \cos\omega + i\sin\omega$ this results in:

$$A = f_{a_1} e^{i\phi_{a_1}} \left(\frac{e^{iQN_a a} - 1}{e^{iQa} - 1}\right) \left(\frac{e^{-iQa} - 1}{e^{-iQa} - 1}\right) = f_{a_1} e^{i\phi_{a_1}} \frac{e^{iQ(N_a-1)a} - e^{-iQa} - e^{iQN_a a} + 1}{2 - 2\cos Qa} \tag{A.2}$$

The product of the complex conjugates in Eq. (A.1) then reads:

$$
\begin{aligned}
AA^* &= f_{a_1}^2 \frac{\left(-e^{iQN_a a} + e^{iQ(N_a-1)a} - e^{-iQa} + 1\right)\left(-e^{-iQN_a a} + e^{-iQ(N_a-1)a} - e^{iQa} + 1\right)}{\left(2 - 2\cos Qa\right)^2} \\[2mm]
&= f_{a_1}^2 \frac{4 - 2e^{-iQa} - 2e^{iQa} - 2e^{-iQN_a a} - 2e^{iQN_a a} + e^{-iQ(N_a+1)a} + e^{iQ(N_a+1)a}}{\left(2 - 2\cos Qa\right)^2} \\[2mm]
&\quad + \frac{e^{iQ(N_a-1)a} + e^{-iQ(N_a-1)a}}{\left(2 - 2\cos Qa\right)^2} \\[2mm]
&= f_{a_1}^2 \frac{2 - 2\cos Qa - 2\cos QN_a a + \cos\left(QN_a a + Qa\right) + \cos\left(Qa - QN_a a\right)}{2\left(1 - \cos Qa\right)^2} \tag{A.3}
\end{aligned}
$$

Using the theorem

$$\cos\left(\alpha + \beta\right) = \cos\alpha\cos\beta - \sin\alpha\sin\beta \tag{A.4}$$

we can further simplify Eq. (A.3) to

$$
\begin{aligned}
AA^* &= f_{a_1}^2 \frac{2 - 2\cos Qa - 2\cos QN_a a + 2\cos(QN_a a)\cos(Qa)}{2(1 - \cos Qa)^2} \\
&= f_{a_1}^2 \frac{(\cos Qa - 1)(\cos QN_a a - 1)}{(1 - \cos Qa)^2} = \frac{\cos QN_a a - 1}{\cos Qa - 1} \\
&= f_{a_1}^2 \frac{\left(\sin \frac{1}{2}QN_a a\right)^2}{\left(\sin \frac{1}{2}Qa\right)^2}.
\end{aligned}
\tag{A.5}
$$

This expression represents the Fourier transform of the monoatomic linear chain. Its atoms have the scattering factor f_{a_1}. For the last step in Eq. (A.5) the identity

$$
\cos \alpha - 1 = -2\left(\sin \frac{1}{2}\alpha\right)^2
\tag{A.6}
$$

was used. It can be derived making use of Eq. (A.4):

$$
\begin{aligned}
\cos \alpha - 1 &= \cos\left(\frac{1}{2}\alpha + \frac{1}{2}\alpha\right) - 1 = \left(\cos \frac{1}{2}\alpha\right)^2 - \left(\sin \frac{1}{2}\alpha\right)^2 - \left(\left(\sin \frac{1}{2}\alpha\right)^2 + \left(\cos \frac{1}{2}\alpha\right)^2\right) \\
&= -2\left(\sin \frac{1}{2}\alpha\right)^2
\end{aligned}
\tag{A.7}
$$

A.2 The diffracted intensity from a thin film with superstructure

The Fourier transform for the linear chain as derived in Eq. (A.5) can be applied to the description of reciprocal space in a perpendicular direction to the plane of a thin film. This applies only to elemental crystals, or to thin films where the the elemental occupancy is the same for all netplanes in growth direction. We will now extend the calculation to crystals with two elements in the unit cell where an alternating stacking of the atoms in the growth direction is observed. Such directions are called *superstructure directions*. Examples for such a system are films of rock salt structure grown in the (111) orientation or of zinc blende structure grown in the (001) orientation. As in the treatment above, we look at a number of N_a stacked unit cells, with a lattice spacing a. To the chain formed by the atoms a_1 with the scattering factor $f_{a_1}e^{i\phi_{a_1}}$, we now add a second chain of atoms a_2 with the scattering factor $f_{a_2}e^{i\phi_{a_2}}$. This second chain is displaced by half a lattice constant with respect to the first one. According to Eq. (2.11) we can add it in Fourier space by a multiplication with the corresponding phase factor $e^{iQ\frac{a}{2}}$. The intensity distribution for this one dimensional superstructure chain

then reads:

$$I(Q) = AA^* = \left(f_{a_1}e^{i\phi_{a_1}}\frac{e^{iQN_aa}-1}{e^{iQa}-1} + e^{iQ\frac{a}{2}}f_{a_2}e^{i\phi_{a_2}}\frac{e^{iQN_aa}-1}{e^{iQa}-1}\right)$$
$$\times \left(f_{a_1}e^{i\phi_{a_1}}\frac{e^{iQN_aa}-1}{e^{iQa}-1} + e^{iQ\frac{a}{2}}f_{a_2}e^{i\phi_{a_2}}\frac{e^{iQN_aa}-1}{e^{iQa}-1}\right)^* \quad (A.8)$$

Evaluating the product in Eq. (A.8) leads to two square contributions and two cross-terms. The squares are similar to the one in Eq. (A.1). Therefore we can instantly apply the solution of Eq. (A.5) to these terms. The cross-terms describe the influence of interference between the two scattering amplitudes of the individual monoatomic linear chains. We can hence write for Eq. (A.8)

$$AA^* = f_{a_1}^2\frac{\left(\sin\frac{1}{2}QN_aa\right)^2}{\left(\sin\frac{1}{2}Qa\right)^2} + f_{a_2}^2\frac{\left(\sin\frac{1}{2}QN_aa\right)^2}{\left(\sin\frac{1}{2}Qa\right)^2}$$
$$+ \left(f_{a_1}e^{i\phi_{a_1}}\frac{e^{iQN_aa}-1}{e^{iQa}-1}\right)\left(e^{iQ\frac{a}{2}}f_{a_2}e^{i\phi_{a_2}}\frac{e^{iQN_aa}-1}{e^{iQa}-1}\right)^*$$
$$+ \left(f_{a_1}e^{i\phi_{a_1}}\frac{e^{iQN_aa}-1}{e^{iQa}-1}\right)^*\left(e^{iQ\frac{a}{2}}f_{a_2}e^{i\phi_{a_2}}\frac{e^{iQN_aa}-1}{e^{iQa}-1}\right) \quad (A.9)$$

As the last two lines in Eq. (A.9) represent the sum of a complex number and its conjugate, the imaginary parts of these cross-terms will cancel out. We therefore only have to consider twice the real part of one of the cross-terms in the further treatment of Eq. (A.9). Making use of Eq. (A.2), the first cross-term is simplified as follows:

$$\left(f_{a_1}e^{i\phi_{a_1}}\frac{e^{iQN_aa}-1}{e^{iQa}-1}\right)\left(e^{iQ\frac{a}{2}}f_{a_2}e^{i\phi_{a_2}}\frac{e^{iQN_aa}-1}{e^{iQa}-1}\right)^*$$
$$= f_{a_1}f_{a_2}\left(e^{i\phi_{a_1}}\frac{e^{iQN_aa}-1}{e^{iQa}-1}\right)\left(\frac{e^{-iQa}-1}{e^{-iQa}-1}\right)\left(e^{i\left(Q\frac{a}{2}+\phi_{a_2}\right)}\left(\frac{e^{iQN_aa}-1}{e^{iQa}-1}\right)\left(\frac{e^{-iQa}-1}{e^{-iQa}-1}\right)\right)^*$$
$$= f_{a_1}f_{a_2}e^{i\left(\phi_{a_1}-\phi_{a_2}-Q\frac{a}{2}\right)}\frac{e^{iQ(N_a-1)a}-e^{-iQa}-e^{iQN_aa}+1}{2-2\cos Qa}$$
$$\times \frac{e^{-iQ(N_a-1)a}-e^{iQa}-e^{-iQN_aa}+1}{2-2\cos Qa}$$
$$= \frac{f_{a_1}f_{a_2}}{(2-2\cos Qa)^2}\left(4e^{i(\phi_{a_1}-\phi_{a_2}-\frac{Qa}{2})} - 2e^{i(\phi_{a_1}-\phi_{a_2}+\frac{Qa}{2})} - 2e^{i(\phi_{a_1}-\phi_{a_2}-\frac{3Qa}{2})}\right.$$
$$-2e^{i(\phi_{a_1}-\phi_{a_2}-\frac{Qa}{2}-QN_aa)} + e^{i(\phi_{a_1}-\phi_{a_2}+\frac{Qa}{2}-QN_aa)} + e^{i(\phi_{a_1}-\phi_{a_2}-\frac{3Qa}{2}-QN_aa)}$$
$$\left.-2e^{i(\phi_{a_1}-\phi_{a_2}-\frac{Qa}{2}+QN_aa)} + e^{i(\phi_{a_1}-\phi_{a_2}+\frac{Qa}{2}+QN_aa)} + e^{i(\phi_{a_1}-\phi_{a_2}-\frac{3Qa}{2}+QN_aa)}\right) \quad (A.10)$$

From this sum of complex numbers we can directly extract the real part, which is the term we need in order to complete the solution of Eq. (A.9). We make use of

the trigonometric notation $e^{i\omega} = \cos\omega + i\sin\omega$, and the substitution $\phi_{a_1} - \phi_{a_2} - \frac{Qa}{2} = \phi_a$. The latter substitution can be interpreted as the phase-shift between the two amplitudes of the two atomic chains occupied by the atoms a_1 and a_2 that are spatially displaced by $\frac{a}{2}$. The real part of Eq. (A.10) then reads:

$$
re\left[\left(f_{a_1}e^{i\phi_{a_1}}\frac{e^{iQN_a a}-1}{e^{iQa}-1}\right)\left(e^{iQ\frac{a}{2}}f_{a_2}e^{i\phi_{a_2}}\frac{e^{iQN_a a}-1}{e^{iQa}-1}\right)^*\right]
$$

$$
= \frac{f_{a_1}f_{a_2}}{(2-2\cos Qa)^2}[4\cos(\phi_a) - 2\cos(\phi_a + Qa) - 2\cos(\phi_a - Qa)
$$
$$
-2\cos(\phi_a - QN_a a) + \cos(\phi_a + Qa - QN_a a)
$$
$$
+\cos(\phi_a - Qa - QN_a a) - 2\cos(\phi_a + QN_a a)
$$
$$
+\cos(\phi_a + Qa + QN_a a) + \cos(\phi_a - Qa + QN_a a)]
$$

$$
= \frac{f_{a_1}f_{a_2}}{(2-2\cos Qa)^2}[4\cos(\phi_a) - 2(\cos(\phi_a + Qa) + \cos(\phi_a - Qa))
$$
$$
-2(\cos(\phi_a + QN_a a) + \cos(\phi_a - QN_a a))
$$
$$
+\cos(\phi_a + (Qa - QN_a a)) + \cos(\phi_a - (Qa - QN_a a))
$$
$$
+\cos(\phi_a + (Qa + QN_a a)) + \cos(\phi_a - (Qa + QN_a a))] \tag{A.11}
$$

With the exception of the first cosine in Eq. (A.13) all trigonometric terms are of the form $(\cos(\alpha + \beta) + \cos(\alpha - \beta))$ using the theorem Eq. (A.4) we can simplify:

$$
\cos(\alpha + \beta) + \cos(\alpha - \beta) = \cos\alpha\cos\beta - \sin\alpha\sin\beta + \cos\alpha\cos\beta + \sin\alpha\sin\beta
$$
$$
= 2\cos\alpha\cos\beta \tag{A.12}
$$

Applying Eq. (A.12) to Eq. (A.11) we can write:

$$
re\left[\left(f_{a_1}e^{i\phi_{a_1}}\frac{e^{iQN_a a}-1}{e^{iQa}-1}\right)\left(e^{iQ\frac{a}{2}}f_{a_2}e^{i\phi_{a_2}}\frac{e^{iQN_a a}-1}{e^{iQa}-1}\right)^*\right]
$$

$$
= \frac{f_{a_1}f_{a_2}}{(2-2\cos Qa)^2}[4\cos(\phi_a) - 4\cos\phi_a\cos(Qa) - 4\cos\phi_a\cos(QN_a a)
$$
$$
+2\cos\phi_a\cos(Qa - QN_a a) + 2\cos\phi_a\cos(Qa + QN_a a)]
$$

$$
= \frac{f_{a_1}f_{a_2}2\cos(\phi_a)}{(2-2\cos Qa)^2}[2 - 2\cos(Qa) - 2\cos(QN_a a)
$$
$$
+\cos(Qa - QN_a a) + \cos(Qa + QN_a a)]
$$

$$
= \frac{f_{a_1}f_{a_2}\cos(\phi_a)}{(1-\cos Qa)^2}[1 - \cos(Qa) - \cos(QN_a a) + \cos(Qa)\cos(QN_a a)]
$$

$$\begin{aligned}
&= \frac{f_{a_1} f_{a_2} \cos(\phi_a)}{(1 - \cos Qa)^2} \left[(1 - \cos(Qa))(1 - \cos(QN_a a)) \right] \\
&= \frac{f_{a_1} f_{a_2} \cos(\phi_a)}{1 - \cos Qa} \left[1 - \cos(QN_a a) \right] \\
&= f_{a_1} f_{a_2} \cos(\phi_a) \frac{\left(\sin(\frac{QN_a a}{2}) \right)^2}{\left(\sin(\frac{Qa}{2}) \right)^2}
\end{aligned} \tag{A.13}$$

In the last step the identity Eq. (A.6) was used. The result of Eq. (A.13) represents the real part of one cross-term in Eq. (A.9). As discussed before, twice this real part represents the interference contribution between the two displaced monoatomic linear chains in Eq. (A.9). The complete analytical solution for a biatomic chain can now be written as the sum of the fundamental intensities for both linear chains and the intensity from the interference of their amplitudes (re-substituting $\phi_a = \phi_{a_1} - \phi_{a_2} - \frac{Qa}{2}$):

$$\begin{aligned}
I(Q) = AA^* &= f_{a_1}^2 \frac{\left(\sin \frac{1}{2} QN_a a \right)^2}{\left(\sin \frac{1}{2} Qa \right)^2} + f_{a_2}^2 \frac{\left(\sin \frac{1}{2} QN_a a \right)^2}{\left(\sin \frac{1}{2} Qa \right)^2} \\
&+ 2 f_{a_1} f_{a_2} \cos \left(\phi_{a_1} - \phi_{a_2} - \frac{Qa}{2} \right) \frac{\left(\sin(\frac{QN_a a}{2}) \right)^2}{\left(\sin(\frac{Qa}{2}) \right)^2}
\end{aligned} \tag{A.14}$$

A.3 The diffracted intensity from an epitaxial double film with superstructure

We now consider a system of two perfect films that are epitaxially grown on top of each other. Both films may feature a superstructure in the growth direction *i.e.* they consist of two different atoms that are alternately stacked. In consistency with the previous section, we described the first film A with its lattice parameter a (in growth direction). The atoms of this film are represented by their complex scattering factors $f_{a_1} e^{i\phi_{a_1}}$ and $f_{a_1} e^{i\phi_{a_2}}$ whereas N_a again describes the number of atomic layers in film A. The second film (B), on top of the first one, is then equivalently represented by the parameters b, $f_{b_1} e^{i\phi_{b_1}}$, $f_{b_2} e^{i\phi_{b_2}}$ and N_b. As for Eq. (A.8) we can describe every atomic chain as a geometrical series, taking into account their relative positions by the corresponding phase factors. In this case, the phase factors for the two linear chains that form film B, both take into account the thickness of film A. The intensity as the absolute square

of the scattering amplitude of this structure is:

$$
\begin{aligned}
I\left(Q\right) = AA^* \quad = \quad & \left(f_{a_1} e^{i\phi_{a_1}} \frac{e^{iQN_a a} - 1}{e^{iQa} - 1} + e^{iQ\frac{a}{2}} f_{a_2} e^{i\phi_{a_2}} \frac{e^{iQN_a a} - 1}{e^{iQa} - 1} \right. \\
& \left. + e^{iQ\left(\left(N_a + \frac{1}{2}\right)a + \frac{b}{2}\right)} f_{b_1} e^{i\phi_{b_1}} \frac{e^{iQN_b b} - 1}{e^{iQb} - 1} + e^{iQ\left(\left(N_a + \frac{1}{2}\right)a + b\right)} f_{b_2} e^{i\phi_{b_2}} \frac{e^{iQN_b b} - 1}{e^{iQb} - 1} \right) \\
\times \quad & \left(f_{a_1} e^{i\phi_{a_1}} \frac{e^{iQN_a a} - 1}{e^{iQa} - 1} + e^{iQ\frac{a}{2}} f_{a_2} e^{i\phi_{a_2}} \frac{e^{iQN_a a} - 1}{e^{iQa} - 1} \right. \\
& \left. + e^{iQ\left(\left(N_a + \frac{1}{2}\right)a + \frac{b}{2}\right)} f_{b_1} e^{i\phi_{b_1}} \frac{e^{iQN_b b} - 1}{e^{iQb} - 1} + e^{iQ\left(\left(N_a + \frac{1}{2}\right)a + b\right)} f_{b_2} e^{i\phi_{b_2}} \frac{e^{iQN_b b} - 1}{e^{iQb} - 1} \right)^*
\end{aligned}
\tag{A.15}
$$

The evaluation of the square in Eq. (A.15) will lead to 16 addends each a product of two of the complex fraction. To further discuss the solution, we will introduce here some abbreviations for the lengthy terms in Eq. (A.15). As the linear chains of the atoms a_1 and a_2 from film A form the first two fractions in Eq. (A.15) we substitute these fractions with A_1 and A_2. These may also include the phase factors. The same shall hold for film B and the fractions B_1 and B_2. We can then write the 16 addends as

$$
\begin{aligned}
I\left(Q\right) = \quad & A_1 A_1^* + A_1 A_2^* + A_1 B_1^* + A_1 B_2^* \\
& A_2 A_1^* + A_2 A_2^* + A_2 B_1^* + A_2 B_2^* \\
& B_1 A_1^* + B_1 A_2^* + B_1 B_1^* + B_1 B_2^* \\
& B_2 A_1^* + B_2 A_2^* + B_2 B_1^* + B_2 B_2^*
\end{aligned}
\tag{A.16}
$$

The diagonal terms in the matrix of Eq. (A.16) are the intensities from the four individual monoatomic linear chains. They have been solved in Eq. (A.5). To the six arguments above the diagonal, we can find the six complex conjugates below the diagonal. They therefore form six cross-term pairs of complex conjugates. As before we therefore only have to evaluate their real parts. Two of these six pairs we know already as the interference terms of the two elements a_1 and a_2 in film A, and b_1 and b_2 in film B. These are the addends $A_1 A_2^*$ and $B_1 B_2^*$ above the diagonal. There remains four more cross-terms which describe interferences between the linear chains in film A, and those in film B. For their solution, the real parts of the addends $A_1 B_1^*$, $A_1 B_2^*$, $A_2 B_1^*$ and $A_2 B_2^*$ of Eq. (A.16) have to be considered. If we look back to Eq. (A.15), we can state that the complex fractions in these four products are the same, and they only differ from each other by a complex phase factor. The treatment of these terms is demonstrated for $A_1 B_1^*$ and can be easily assigned to the others. From eqs. (A.15) and (A.16) we can

deduce:

$$A_1 B_1^* = \left(f_{a_1} e^{i\phi_{a_1}} \frac{e^{iQN_a a} - 1}{e^{iQa} - 1} \right) \left(e^{iQ((N_a + \frac{1}{2})a + \frac{b}{2})} f_{b_1} e^{i\phi_{b_1}} \frac{e^{iQN_b b} - 1}{e^{iQb} - 1} \right)^*$$

$$= f_{a_1} f_{b_1} e^{i[Q(-(N_a + \frac{1}{2})a - \frac{b}{2}) + \phi_{a_1} - \phi_{b_1}]} \left(\frac{e^{iQN_a a} - 1}{e^{iQa} - 1} \right) \left(\frac{e^{-iQN_b b} - 1}{e^{-iQb} - 1} \right) \quad \text{(A.17)}$$

As done in Eq. (A.2) we eliminate the imaginary parts in the denominator and expand Eq. (A.17) to

$$A_1 B_1^* = f_{a_1} f_{b_1} e^{i\left[Q\left(-\left(N_a + \frac{1}{2}\right)a - \frac{b}{2}\right) + \phi_{a_1} - \phi_{b_1}\right]}$$

$$\times \quad \frac{\left(e^{iQ(N_a - 1)a} - e^{-iQa} - e^{iQN_a a} + 1 \right) \left(e^{-iQ(N_b - 1)b} - e^{iQb} - e^{-iQN_b b} + 1 \right)}{(2 - 2\cos(Qa))(2 - 2\cos(Qb))} \text{(A.18)}$$

Expanding Eq. (A.18) and taking twice its real part, we evaluate for the sum of the two crossterms $A_1 B_1^*$ and $B_1 A_1^*$ from Eq. (A.16):

$$A_1 B_1^* + B_1 A_1^* = \frac{2 * f_{a_1} f_{b_1}}{(2 - 2\cos(Qa))(2 - 2\cos(Qb))}$$

$$\times \left[\cos(\phi_{a_1} - \phi_{b_1} - \frac{3aQ}{2} - \frac{bQ}{2}) - \cos(\phi_{a_1} - \phi_{b_1} - \frac{aQ}{2} - \frac{bQ}{2}) \right.$$

$$- \cos(\phi_{a_1} - \phi_{b_1} - \frac{3aQ}{2} + \frac{bQ}{2}) + \cos(\phi_{a_1} - \phi_{b_1} - \frac{aQ}{2} + \frac{bQ}{2})$$

$$- \cos(\phi_{a_1} - \phi_{b_1} - \frac{3aQ}{2} - \frac{bQ}{2} - N_a aQ) + \cos(\phi_{a_1} - \phi_{b_1} - \frac{aQ}{2} - \frac{bQ}{2} - N_a aQ)$$

$$+ \cos(\phi_{a_1} - \phi_{b_1} - \frac{3aQ}{2} + \frac{bQ}{2} - N_a aQ) - \cos(\phi_{a_1} - \phi_{b_1} - \frac{aQ}{2} + \frac{bQ}{2} - N_a aQ)$$

$$- \cos(\phi_{a_1} - \phi_{b_1} - \frac{3aQ}{2} - \frac{bQ}{2} - N_b bQ) + \cos(\phi_{a_1} - \phi_{b_1} - \frac{aQ}{2} - \frac{bQ}{2} - N_b bQ)$$

$$+ \cos(\phi_{a_1} - \phi_{b_1} - \frac{3aQ}{2} + \frac{bQ}{2} - N_b bQ) - \cos(\phi_{a_1} - \phi_{b_1} - \frac{aQ}{2} + \frac{bQ}{2} - N_b bQ)$$

$$+ \cos(\phi_{a_1} - \phi_{b_1} - \frac{3aQ}{2} - \frac{bQ}{2} - N_a aQ - N_b bQ)$$

$$- \cos(\phi_{a_1} - \phi_{b_1} - \frac{aQ}{2} - \frac{bQ}{2} - N_a aQ - N_b bQ)$$

$$- \cos(\phi_{a_1} - \phi_{b_1} - \frac{3aQ}{2} + \frac{bQ}{2} - N_a aQ - N_b bQ)$$

$$\left. + \cos(\phi_{a_1} - \phi_{b_1} - \frac{aQ}{2} + \frac{bQ}{2} - N_a aQ - N_b bQ) \right] \quad \text{(A.19)}$$

Here we find numerous pairs equivalent to the form $(\cos(\alpha + \beta) + \cos(\alpha - \beta))$. Therefore we make use of eqs. (A.12) and (A.6) and derive:

$$A_1 B_1^* + B_1 A_1^* = 2 * f_{a_1} f_{b_1} \cos(\phi_{a_1} - \phi_{b_1} - aQ - \frac{N_a aQ}{2} - \frac{N_b bQ}{2})$$

$$\times \quad \frac{\sin(\frac{N_a a Q}{2}) \sin(\frac{N_b b Q}{2})}{\sin(\frac{a Q}{2}) \sin(\frac{b Q}{2})} \tag{A.20}$$

Evaluating the other crossterms in Eq. (A.16) this finally simplifies Eq. (A.15) to

$$I(Q) = AA^* =$$

$$2 \left[f_{a_1}^2 + f_{a_2}^2 + 2 f_{a_1} f_{a_2} \cos\left(\phi_{a_1} - \phi_{a_2} - \frac{1}{2} a Q\right) \right] \left(\frac{\sin\left(\frac{1}{2} a N_a Q\right)}{\sin\left(\frac{1}{2} a Q\right)}\right)^2$$

$$+ \quad 2 \left[f_{b_1}^2 + f_{b_2}^2 + 2 f_{b_1} f_{b_2} \cos\left(\phi_{b_1} - \phi_{b_2} - \frac{1}{2} b Q\right) \right] \left(\frac{\sin\left(\frac{1}{2} b N_b Q\right)}{\sin\left(\frac{1}{2} b Q\right)}\right)^2$$

$$+ \quad 2 \left[f_{a_1} f_{b_1} \cos\left(\phi_{a_1} - \phi_{b_1} - a Q - \frac{1}{2} a N_a Q - \frac{1}{2} b N_b Q\right) \right.$$

$$+ \quad f_{a_1} f_{b_2} \cos\left(\phi_{a_1} - \phi_{b_2} - a Q - \frac{1}{2} a N_a Q - \frac{1}{2} b N_b Q - \frac{1}{2} b Q\right)$$

$$+ \quad f_{a_2} f_{b_1} \cos\left(\phi_{a_2} - \phi_{b_1} - \frac{1}{2} a Q - \frac{1}{2} a N_a Q - \frac{1}{2} b N_b Q\right)$$

$$+ \quad f_{a_2} f_{b_2} \cos\left(\phi_{a_2} - \phi_{b_2} - \frac{1}{2} a Q - \frac{1}{2} a N_a Q - \frac{1}{2} b N_b Q - \frac{1}{2} b Q\right) \right]$$

$$* \quad \frac{\sin\left(\frac{1}{2} a n_a Q\right) \sin\left(\frac{1}{2} b N_b Q\right)}{\sin\left(\frac{1}{2} a Q\right) \sin\left(\frac{1}{2} b Q\right)}$$

$$\tag{A.21}$$

List of Figures

References

[1] J. S. Kilby, Nobel Lecture, (2000).

[2] C. S. Lent, P. D. Tougaw, W. Porod, G. H. Bernstein, Nanotechnology **4**, 49 (1993).

[3] P. D. Tougaw, C. S. Lent, J. Appl. Phys. **75**, 1818 (1994).

[4] D. Bimberg, M. Grundmann, N. N. Ledentsov, *Quantum dot heterostructures*, John Wiley & Sons, Chichester, Great Britain (1999).

[5] A. Rogalski, K. Chrzanowski, Opto-Electron. Rev. **10**, 111 (2002).

[6] H. Zogg, C. Maissen, J. Masek, T. Hoshino, S. Blunier, A. N. Tiwari, Semicond. Sci. Tech. **6**, C36 (1991).

[7] D. L. Partin, R. F. Majkowski, D. E. Swets, J. Vac. Sci. Technol. B **3**, 576 (1985).

[8] H. Beyer, J. Nurnus, H. Bttner, A. Lambrecht, T. Roch, G. Bauer, Appl. Phys. Lett. **80**, 1216 (2002).

[9] G. Springholz, T. Schwarzl, W. Heiss, G. Bauer, M. Aigle, H. Pascher, I. Vavra, Appl. Phys. Lett. **79**, 1225 (2001).

[10] B. G. Levi, Phys.Today **49**, 22 (1996).

[11] P. M. Petroff, A. Lorke, A. Imamoglu, Phys. Today **54**, 46 (2001).

[12] J. Tersoff, Phys. Rev. Lett. **81**, 3183 (1998).

[13] D. J. Bottomley, Appl. Phys. Lett. **72**, 783 (1998).

[14] X. Z. Liao, J. Zou, D. J. H. Cockayne, J. Qin, Z. M. Jiang, X. Wang, R. Leon, Phys. Rev. B **60**, 15605 (1999).

[15] M. Born, E. Wolf, *Principles of optics. Electromagnetic theory of propagation, interference and diffraction of light*, Cambridge University Press, Cambridge, Great Britain (1997).

[16] G. Materlick, C. J. Sparks, K. Fisher, *Resonant Anomalous X-Ray Scattering: Theory and applications*, North-Holland, Amsterdam (1994).

[17] A. González, J.-D. Pédelacq, M. Sola, F. X. Gomis-Rüth, M. Coll, J.-P. Samama, S. Benini, Acta Cryst D **55**, 1449 (1999).

[18] T. Fukamachi, S. Hosoya, M. Okunuki, Acta Cryst. A **32**, 245 (1976).

[19] J. A. Elliot, S. Hanna, J. Appl. Cryst. **32**, 1069 (1999).

[20] J. Pearce, D. Mittleman, Phys. Rev. E **66**, 056602 (2002).

[21] J. D. Jackson, *Classical electrodynamics*, John Wiley & Sons Inc., New York (1967).

[22] A. Compton, S. Allison, *X-rays in theory and experiment*, Van Nostrand, (1935).

[23] J. H. Hubbell, W. J. Veigele, E.A. Briggs, R. T. Brown, D. T. Cromer, R. J. Howerton, J. Phys. Chem. Ref. Data **4**, 471 (1975).

[24] D. Cromer, D. Liberman, J. Chem. Phys. **53**(5), 1891 (1970).

[25] B. L. Henke, E. M. Gullikson, J. C. Davis, Atomic Data and Nuclear Data Tables **54**, 181 (1993).

[26] D. C. Creagh, W. J. McAuley, in International Tables for Crystallography Vol. C, edited by A. J. C. Wilson, Kluwer Academic Publishers, Dordrecht (1992).

[27] J. Baró, M. Roteta, J. M. Fernández-Varea, F. Salvat, Radiat. Phys. Chem. **44**, 531 (1994).

[28] P. M. Bergstrom Jr, L. Kissel, R. H. Pratt, A. Costescu, Acta Cryst. A **53**, 7 (1997).

[29] T. Fukamachi, R. Negishi, M. Yoshizawa, K. Ehara, T. Kawamura, T. Nakajima, Z. Zhao, Acta Cryst. A **49**, 573 (1993).

[30] A. E. H. Love, *A treatise on the mathematical theory of elasticity*, Dover Publications, New York (1944).

[31] J. F. Nye, *Physical properties of crystals*, Oxford University Press, London (1957).

[32] C. Zener, *Élasticité et anélasticité des métaux*, Dunod, Paris (1955).

[33] J. H. van der Merwe, D. L. Tonsing, P. M. Stoop, Surf. Sci. **312**, 387 (1994).

[34] A. Pimpinelli, J. Villain, *Physics of crystal growth*, Cambridge University Press, Cambridge, Great Britain (1998).

[35] U. Pietsch, W. Seifert, J. Fornell, H. Rhan, T. H. Metzger, S. Rugel, J. Peisl, Appl. Surf. Sci. **54**, 502 (1992).

[36] T. H. Metzger, I. Kegel, R. Paniago, J. Peisl, J. Phys. D: Appl. Phys. **32**, A202 (1999).

[37] T. Wiebach, M. Schmidbauer, M. Hanke, H. Raidt, R. Köhler, H. Wawra, Phys. Rev. B **61**, 5571 (2000).

[38] A. Hesse, J. Stangl, V. Holý, T. Roch, G. Bauer, O.G. Schmidt, U. Denker, B. Struth Phys. Rev. B **66**, 085321 (2002).

[39] K. Albe, K. Nordlund, J. Nord, A. Kuronen, Phys. Rev. B **66**, 035205 (2002).

[40] V. Holý, U. Pietsch, T. Baumbach, *High resolution x-ray scattering from thin films and multilayers*, Springer Verlag, Berlin (1999), p. 164.

[41] G. Springholz, V. Holý, M. Pinczolits, G. Bauer, Science **282**, 734 (1998).

[42] T. U. Schülli, M. Sztucki, V. Chamard, T. H. Metzger, D. Schuh, Appl. Phys. Lett. **81**, 448 (2002).

[43] B. E. Warren, *X-ray diffraction*, Dover Publications Inc., New York (1969).

[44] B. Nickel, W. Donner, H. Dosch, C. Detlefs, G. Grübel, Phys. Rev. Lett. **85**, 134 (2000).

[45] P. F. Fewster, C. J. Curling, J. Appl. Phys. **62**, 4154 (1987).

[46] S. Nakamura, Semicond. Sci. Technol. **14**, R27 (1999).

[47] H. Soda, K. Iga, C. Kitahara, Y. Suematsu, Jpn. J. Appl. Phys. **18**, 2329 (1979).

[48] V. Holý, P. F. Fewster, X-Top Conference Aussois 2002, to be published in J. Appl. Phys. D (2003).

[49] T. Hatano, R. Akimoto, M Kobayashi, T. Suzuki, S. Endo, J. Phys. Chem. Solids **56**, 531 (1995).

[50] I.N. Goncharenko, I. Mirebeau, Europhys. Lett. **37**, 633 (1997).

[51] I.N. Goncharenko, I. Mirebeau, Phys. Rev. Lett. **80**, 1082 (1998).

[52] K. Yamada, A. Kowata, K. Satoh, H. Koike, K. Yamaguchi, J. Magn. Magn. Mater. **157/158**, 563 (1996).

[53] D. Singh, M. Rajagopalan, A. K. Bandyopadhyay, Solid State Commun. **112**, 39 (1999).

[54] R. T. Lechner *et al., to be published.*

[55] C. Teichert, Phys. Rep. **365**, 335 (2002).

[56] G.Medeiros-Ribero, A.M. Bratkovski, T.I. Kamins, D.A.A. Ohlberg, and R.S.Williams, Science **279**, 353 (1998).

[57] L. Vescan, T. Stoica, O. Chretien, M. Goryll, E. Mateeva, A. Muck, J. Appl.Phys. **87**, 7275 (2000).

[58] Chuan-Pu Liu, J. M. Gibson, D.G. Cahill, T.I. Kamins, D.P. Basile, and R.S. Williams, Phys. Rev. Lett. **84**, 1958 (2000).

[59] T. Walther, A.G. Cullis, D.J. Norris, M. Hopkinson, Phys. Rev. Lett. **86**, 2381 (2001).

[60] H. You, J. Appl. Cryst. **32**, 614 (1999).

[61] H. Kiessig, Ann. d. Phys., **10**, 715 (1931).

[62] L. G. Parratt, Phys. Rev., **95**, 359 (1954).

[63] L. Névot, P. Croce, Revue Phys. Appl., **15**, 761 (1980).

[64] H.Dosch, *Critical Phenomena at Surfaces and Interfaces*, Springer Verlag, Heidelberg (1992).

[65] J. A. Bearden, A. F. Burr, Rev. Mod. Phys. **39**, 125 (1967).

[66] I. Kegel, T. H. Metzger, A. Lorke, J. Peisl, J. Stangl, G. Bauer, K. Nordlund, W. V Schoenfeld, P. M. Petroff, Phys. Rev. B **63**, 035318 (2001).

[67] I. K. Robinson, D. J. Tweet, Rep. Prog. Phys. **55**, 599 (1992).

[68] G. Springholz, A. Y. Ueta, N. Frank, G. Bauer, Appl. Phys. Lett **69**, 2822 (1996).

[69] X. Deng, J. D. Weil, M. Krishnamurthy, Phys. Rev. Lett. **80**, 4721 (1998).

[70] J. Stangl, A. Daniel, V. Holý, T. Roch, G. Bauer, I. Kegel, T. H. Metzger, T. Wiebach, O. G. Schmidt, K. Eberl, Appl. Phys. Lett. **79**, 1474 (2001).

[71] A. Hesse, J. Stangl, V. Holý, T. Roch, G. Bauer, O. G. Schmidt, U. Denker, B. Struth, Phys. Rev. B **66**, 085321 (2002).

[72] R. Magalhaes-Paniago, G. Medeiros-Ribeiro, A. Malachias, S. Kycia, T. I. Kamins, R. Stan Williams, Phys. Rev. B **66**, 245312 (2002).

[73] T. U. Schülli, J. Stangl, Z. Zhong, R. T. Lechner, M. Sztucki, T. H. Metzger, G. Bauer, Phys. Rev. Lett. **90**, 066105 (2003).

[74] R. S. Williams, G. Medeiros-Ribeiro, T. I. Kamins, D. A. A. Ohlberg, Ann. Rev. Phys. Chem. **51**, 527 (2000).

[75] O. G. Schmidt, C. Lange, K. Eberl, Appl. Phys. Lett **75**, 1905 (1999).

[76] O. G. Schmidt, K. Eberl, Phys. Rev. B **61**, 13721 (2000).

[77] S. A. Chaparro, J. Drucker, Y. Zhang, D. Chandrasekhar, M.R. McCartney, D. J. Smith, Phys. Rev. Lett. **83**, 1199 (1999).

[78] S. A. Chaparro, Y. Zhang, J. Drucker, Appl. Phys. Lett. **76**, 3534 (2000).

[79] T. K. Carns, M. O. Tanner, K. L. Wang, J. Electrochem. Soc. **142**, 1260 (1995).

[80] U. Denker, M. W. Dashiell, N. Y. Jin-Phillipp, O. G. Schmidt, Mater. Sci. Eng. B **89**, 166 (2002).

[81] U. Denker, M. Stoffel, O. G. Schmidt, H. Sigg, Appl. Phys. Lett. **82**, 454 (2003).

[82] M. Stoffel *et al.*, to be published.

[83] A. Raab, G. Springholz, Phys. Stat. Sol. **224**, 509 (2001).

[84] K. Alchalabi, D. Zimin, G. Kostorz, H. Zogg, Phys. Rev. Lett. **90**, 026104 (2003).

[85] X. L. Huang, Z. Labadi, A. Hammiche, A. Krier, J. Appl. Phys. **35**, 3091 (2002).

[86] G. Springholz, M. Pinczolits, P. Mayer, V. Holý, G. Bauer, H. H. Kang, L. Salamanca-Riba, Phys. Rev. Lett. **84**, 4669 (2000).

[87] M. Pinczolits, G. Springholz, G. Bauer, Phys. Rev. B **60**, 11524 (1999).

[88] A. Raab, R. T. Lechner, G. Springholz, Appl. Phys. Lett. **80**, 1273 (2002).

[89] P. Boucaud, V. Le Thanh, V. Yam, S. Sauvage, N. Meneceur, M. Elkurdi, D. Debarre, D. Bouchier, Mater. Sci. Eng. B **89**, 36 (2002).

[90] A. Rastelli, M. Kummer, H. von Känel, Phys. rev. Lett. **87**, 256101 (2001).

[91] V. Holý, G. Springholz, M. Pinczolits, G. Bauer, Phys. Rev. Lett. **83**, 356 (1999).

[92] R. T. Lechner, T. U. Schülli, G. Springholz, G. Bauer, D.Lott, A. Schreyer, H. Clemens, *Conference presentation at the MRS 2002 Fall Meeting, Boston.*

[93] F. Boscherini, Nucl. Instr. and Meth. in Phys. Res. B **199**, 169 (2003).

[94] A. V. Kolobov, H. Oyanagi, S. Wei, K. Brunner, G. Abstreiter, K. Tanaka, Phys. Rev. B **66**, 075319 (2002).

List of Publications

X-ray diffraction from semiconductor nanostructures

[1] T. U. Schülli, M. Sztucki, T. H. Metzger, J. Stangl, Z. Zhong, R. T. Lechner, G. Bauer, *Direct Determination of Strain and Composition Profiles in SiGe Islands by Anomalous X-ray Diffraction at High Momentum Transfer*, Phys. Rev. Lett. **90**, 066105 (2003).

[2] J. Stangl, A. Hesse, T. Roch, V. Holý, G. Bauer, T. Schuelli, T. H. Metzger, *Structural Investigation of Semiconductor Nanostructures by X-ray Techniques*, Nucl. Instr. and Meth. in Phys. Res. B **200**, 11 (2003).

[3] T. U. Schülli, M. Sztucki, V. Chamard, T. H. Metzger, D. Schuh, *Anomalous X-ray Diffraction on InAs/GaAs Quantum Dot Systems*, Appl. Phys. Lett. **81**, 448 (2002).

[4] M. Derivaz, P. Noé, R. Dianoux, A. Barski, T. Schülli, T. H. Metzger, *Growth of Highly Strained Ge Dots on Si(001) Covered by a Silicon Nitride Layer*, Appl. Phys. Lett. **81**, 3843 (2002).

Other publications about x-ray diffraction

[5] T. Schülli, J. Trenkler, I. Mönch, D. Le Bolloc'h, H. Dosch, *X-ray study of the structure and order in Cu_3Au nano-cuboids*, Europhys. Lett. 58, 737 (2002).

[6] D. Le Bolloc'h, F. Livet, F. Bley, T. U. Schulli, M. Veron, T. H. Metzger, *X-ray diffraction from rectangular slits*, J. Synchrotron Rad. **8**, 258 (2002).

Acknowledgements

The completion of this work needed the help of many people who I would like to acknowledge for their support during my time in Grenoble and during the years before. Among these, there are even many who will not appear on these pages. My special thanks go to

- **Prof. Dr. Günther Bauer** whose support, motivation and ideas were indispensable. His continuous interest in the progress of this work have been a source of motivation in particular during the long weekends and night-shifts at the beamline.

- **Dr. Till Hartmut Metzger** as my supervisor and the responsible of the beamline ID01 at the ESRF in Grenoble. The scientific and experimental knowledge he shared allowed me a very efficient start in my x-ray scattering experiments. During my two years at ID01 he was always open towards any scientific and non-scientific discussion.

- **Prof. Dr. Václav Holý** for his willingness to co-assess this thesis. In particular I want to thank him for his open and motivating way of discussing and solving problems in diffraction and computation.

- **Dr. Julian Stangl, Rainer T. Lechner, Dr. Zhenyang Zong and Eugen Wintersberger** for their support during the beamtimes.

- **Michael Sztucki** for his incredibly successful pragmatism in the solution of all computer problems.

- **Dr. Mathieu Stoffel** from the Max-Planck-Institute for solid state research in Stuttgart, for the growth of the SiGe samples and the fruitful collaboration.

- **Dr. Samantha Warren** for her absolutely necessary language corrections.

- **Dr. David Le Bolloc'h** for hosting me during my first months in Grenoble. His social and scientific activity together with his inexhaustible energy allowed me a very pleasant start in the new environment.

- **Dr. Virginie Chamard, Luciana Capello, Dr. Olivier Plantevin, and Dr. Bruno Jean** as my collegues who created the nice atmosphere in our group. They receive my special thanks for helping me in numerous language and administrative problems.

Curriculum Vitae

14.04.1974	Born in Heidelberg
1980-1984	Primary school in Waiblingen
1984-1993	High school, Salier Gymnasium in Waiblingen
1993-1994	Military Service
1994-2000	Studies in physics and mathematics at the University of Stuttgart
1999-2000	Diploma thesis at the Max-Planck-Institute for metal research in Stuttgart. Title: *Laterale Strukturierung und röntgenographische Untersuchung epitaktischer Metallfilme.*
2000-2003	PhD thesis at the European Synchrotron Radiation Facility (ESRF) in collaboration with the institute for semiconductor physics at the Johannes Kepler University in Linz.